



POLITECNICO DI MILANO  
DEPARTMENT OF ENERGY  
DOCTORAL PROGRAMME IN ENERGY AND NUCLEAR SCIENCE AND  
TECHNOLOGY

---

TWO-PHASE HEAT AND MASS TRANSFER MODELING:  
FLEXIBLE NUMERICAL METHODS FOR ENERGY  
ENGINEERING ANALYSES

Doctoral Dissertation of:  
**Gaël Guédon**

Advisor:

**Prof. Emanuela Colombo**

Tutor:

**Prof. Fabio Inzoli**

The Chair of the Doctoral Program:

**Prof. Carlo Enrico Bottani**

August 2013 – XXV Cycle



*A mes parents et à mes frères*



---

## Acknowledgements

---

I would like to express my sincere gratitude to my supervisors Professor Fabio Inzoli and Professor Emanuela Colombo for their constant guidance and encouragement since the last year of my master degree, and for the opportunity they gave me to begin this doctoral course. It has been a privilege for me to share their vast knowledge and enthusiasm.

I am truly grateful to Professor Jacopo Buongiorno from the Department of Nuclear Science and Engineering of the Massachusetts Institute of Technology (MIT). The opportunity he gave me to spend five months as a visiting PhD student at the Computational Multiphase Fluid Dynamics laboratory has been very rewarding and fruitful for the completion of this thesis. I am also grateful to the Progetto Roberto Rocca joint MIT–Politecnico di Milano research program for its financial support.

All my colleagues and friends at Politecnico di Milano and MIT are gratefully thanked for the enjoyable and propitious working atmosphere they offered. I am indebted to Paolo Lampitella for all the advices he gave me and for sharing his expertise on numerical methods with me. I am also indebted to Riccardo Mereu for the precious help he gave me during all these years.

On a more personal note, the Strada family and relatives receive my acknowledgments for the kindness, generosity and precious support they offered me during my stay in Italy. Great thanks also to Claudio Basilico and his friends for their support, entertaining conversations and good company.

Last but not least, I thank my family especially my parents and brothers. Without their love and support, the endeavor could not have been made truly worthwhile.



*“Blow a soap bubble and observe it.  
You may study it all your life and draw one  
lesson after another in physics from it.”*

*Lord Kelvin*



---

## Abstract

---

**D**EVELOPING a high resolution numerical method for the simulation of two-phase heat and mass transfer is a viable way of getting deeper insights into such phenomena, and as consequence to better understand them. A reliable and flexible numerical method is developed in the present thesis in order to achieve this goal. The method is applied to the simulation of boiling phenomena, which is a relevant mode of heat transfer in the energy sector, however it may be easily extended to other types of heat and mass transfer phenomena such as condensation.

Boiling is a very efficient mode of heat transfer and plays a major role in several engineering systems for the production and conversion of energy. Despite its wide use, the design of heat exchangers still relies on empirical correlations that have been developed during the second half of the twentieth century, because the numerical methods for the simulation of boiling phenomena are still not well established. In addition, several aspects of boiling heat transfer are still not well understood.

The several spatial scales involved in boiling phenomena constitute one of the main difficulties in the development of a reliable numerical method. Various numerical issues also arise due to the presence of moving two-phase interfaces. The correct prediction of capillary forces, mass transfer rate and heat transfer, with an optimized computational cost, is the principal challenge of nowadays numerical models.

Within this framework, a numerical model is developed using the open-source OpenFOAM Computational Fluid Dynamics toolkit, which permits a high flexibility and sustainability of the model. The Finite Volume discretization method is used to solve the governing equations of the problem. The method is compatible with general unstructured meshes in two- and three-dimension. A mass-conservative Volume-Of-Fluid interface tracking method is adopted to capture the position of the two-phase interface and its influence on the fluids flow. Four interfacial curvature calculation methods for the prediction of surface tension are implemented and compared. The mass transfer rate is computed directly from the heat flux at the interface using a reconstructed Level-Set function. The sources due to mass transfer are then concentrated near the interface. Adaptive mesh refinement is possible in three-dimension and the mesh is usually refined near the interface, where a higher mesh resolution is beneficial for the correct

---

prediction of the mass transfer rate.

The detailed description of the governing equations and of the implemented numerical model is followed by a verification and validation process. Dedicated test cases are employed for the isothermal and phase change part of the model. Isothermal static bubbles and capillary waves are studied to evaluate the accuracy of the implemented interfacial curvature calculation methods. The proper implementation and validation of the phase change model is then performed by investigating the Stefan, sucking interface, and spherical bubble growth problems. The several numerical issues related to two-phase heat and mass transfer are identified and the accuracy of the model is assessed.

The present thesis also contains a detailed study of isothermal spherical rising air bubbles in water with dimensions typical of heat and mass transfer applications. A thorough review of the experimental and theoretical works is performed in order to identify the most appropriate reference data for the comparison with the numerical model. A high dependence of the bubbles' terminal rising velocity on the interfacial curvature calculation method is observed, suggesting the use of the height function method implemented in the open-source Gerris Flow Solver code.

Finally, a benchmark for the simulation of nucleate boiling is developed using experimental data from the pool boiling facility of the Department of Nuclear Science and Engineering of the Massachusetts Institute of Technology.

---

# Contents

---

<b>1</b>	<b>Introduction</b>	<b>1</b>
1.1	Relevance of two-phase heat and mass transfer in energy applications . . . . .	2
1.2	Boiling phenomena . . . . .	2
1.3	State of the art . . . . .	6
1.3.1	Related experimental work . . . . .	6
1.3.2	Modeling approaches at the interface scale . . . . .	7
1.4	Objectives . . . . .	12
1.5	Novel contributions in this thesis . . . . .	13
<b>2</b>	<b>Governing equations</b>	<b>15</b>
2.1	Local instant conservation equations . . . . .	15
2.1.1	General balance equation . . . . .	15
2.1.2	Laws of conservation . . . . .	17
2.1.3	Constitutive equations . . . . .	19
2.1.4	Interfacial jump and boundary conditions . . . . .	21
2.2	One-fluid formulation . . . . .	25
2.2.1	Conservation of mass . . . . .	26
2.2.2	Conservation of linear momentum . . . . .	27
2.2.3	Enthalpy equation . . . . .	28
<b>3</b>	<b>Implemented numerical method</b>	<b>31</b>
3.1	Finite volume discretization . . . . .	31
3.1.1	Discretization of the computational domain . . . . .	32
3.1.2	Formulation of the discretized governing equations . . . . .	33
3.1.3	Solution of the system of linear algebraic equation . . . . .	38
3.2	Interface tracking . . . . .	39
3.3	Interfacial curvature calculation . . . . .	40
3.3.1	Original method: Gauss integration . . . . .	41
3.3.2	First proposed method: node-based gradient . . . . .	41
3.3.3	Second proposed method: recursive weighted interpolations . . . . .	42
3.3.4	Height function method . . . . .	44

## Contents

---

3.4	Interfacial jumps due to heat and mass transfer . . . . .	44
3.4.1	Transport of the volume fraction . . . . .	45
3.4.2	Mass, momentum and energy equations . . . . .	46
3.4.3	Calculation of the mass transfer flux . . . . .	47
3.5	Pressure-velocity coupling . . . . .	48
3.6	Treatment of body forces . . . . .	50
3.6.1	Gravity acceleration . . . . .	50
3.6.2	Surface tension . . . . .	51
3.7	Solution procedure . . . . .	52
<b>4</b>	<b>Verification and validation of the method</b>	<b>53</b>
4.1	Isothermal two-phase model . . . . .	53
4.1.1	Interfacial curvature estimates of a perfectly spherical interface . . . . .	53
4.1.2	Description of the spurious currents . . . . .	55
4.1.3	Stationary axisymmetric circular interface . . . . .	57
4.1.4	Planar capillary wave . . . . .	61
4.2	Phase change model . . . . .	63
4.2.1	One-dimensional Stefan problem . . . . .	63
4.2.2	One-dimensional sucking interface problem . . . . .	64
4.2.3	Spherical vapor bubble growth . . . . .	68
<b>5</b>	<b>Results on isothermal spherical rising bubbles</b>	<b>73</b>
5.1	Reference data . . . . .	74
5.2	Boundary conditions and initialization . . . . .	78
5.3	Results . . . . .	80
5.3.1	Calculation of the terminal rise velocity . . . . .	80
5.3.2	Grid convergence analysis . . . . .	80
5.3.3	Characterization of the bubble rise . . . . .	81
5.3.4	Flow field description . . . . .	86
<b>6</b>	<b>Single bubble nucleate pool boiling benchmark</b>	<b>89</b>
6.1	The MIT pool boiling facility . . . . .	89
6.2	Simplifying assumptions . . . . .	92
6.3	Computational domain, boundary conditions and initialization . . . . .	93
6.3.1	Computational domain . . . . .	93
6.3.2	Boundary conditions . . . . .	93
6.3.3	Initial conditions . . . . .	94
6.4	Data post-processing . . . . .	95
6.5	Experimental results . . . . .	96
6.5.1	High-speed video imaging . . . . .	97
6.5.2	High-speed IR measurements . . . . .	97
<b>7</b>	<b>Conclusions and outlook</b>	<b>101</b>
7.1	Summary . . . . .	101
7.2	Future work . . . . .	103
<b>Bibliography</b>		<b>105</b>

---

## List of Figures

---

1.1 Pool boiling curve for water at atmospheric pressure (Collier and Thome, 1994). . . . .	3
1.2 Pool boiling curve for water at atmospheric pressure (Collier and Thome, 1994). . . . .	4
2.1 Material volume $V(t)$ cut by an interface $A_{\text{int}}(t)$ . . . . .	16
2.2 Contact angle $\theta$ in function of the surface tension between gas-liquid $\sigma$ , gas-solid $\sigma_{gs}$ , and liquid-solid $\sigma_{ls}$ . . . . .	25
3.1 Typical control volume. The cube symbol ■ denotes the cell center, the cross × the face center and the spheres • the points defining the cell and its faces. . . . .	32
4.1 Cell contour of the estimated interfacial curvature of a perfectly spherical interface using a) the <i>Gauss</i> method and b) the <i>node-based gradient</i> method ( $r_e/\Delta = 24$ ). . . . .	54
4.2 Cell contour of the estimated interfacial curvature of a perfectly spherical interface using a) the <i>recursive weighted interpolations</i> method and b) the <i>height function</i> method ( $r_e/\Delta = 24$ ). . . . .	55
4.3 Convergence rate of the relative error norm $L_\infty(\kappa)$ computed from interfacial cells and its one-cell neighborhood. . . . .	56
4.4 Boundary conditions and computational mesh corresponding to the <i>coarse</i> resolution. . . . .	58
4.5 Computational mesh corresponding to the a) <i>intermediate</i> and b) <i>fine</i> resolutions. . . . .	58
4.6 Time history of the relative amplitude of an air-water capillary wave ( $\text{La} = 3000$ ). The mesh resolution is $128 \times 384$ . . . . .	62
4.7 Domain definition for the Stefan problem. . . . .	63
4.8 Time evolution of the interface position for the Stefan problem. . . . .	65
4.9 Domain definition for the sucking interface problem. . . . .	66
4.10 Time evolution of the interface position for the sucking interface problem.	67

---

## List of Figures

---

4.11 Temperature profiles at $t = 1.1\text{s}$ for the sucking interface problem. . . . .	67
4.12 Domain definition for the spherical vapor bubble growth problem. . . . .	69
4.13 Time evolution of the interface position for the spherical vapor bubble growth problem. . . . .	70
4.14 Temperature profiles at $t = 0.3\text{ms}$ for the spherical vapor bubble growth problem. . . . .	71
5.1 Shape regimes for bubbles rising in stagnant liquids (Clift et al., 1978). . . . .	75
5.2 Terminal rise velocity of air bubbles in water at $20^\circ\text{C}$ by Clift et al. (1978), left, and Tomiyama (2004), right. . . . .	76
5.3 Analytical terminal rise velocity values for air bubble in water at $20^\circ\text{C}$ . . . . .	77
5.4 Overview of the domain extension, boundary conditions and meshing strategies. . . . .	79
5.5 Bubble rise velocity history for the case Large ( $d_e = 0.9 \text{ mm}$ ). Results from the <i>Gauss</i> , <i>nbg</i> and <i>rwi</i> methods (OpenFOAM code). . . . .	83
5.6 Bubble rise velocity history for the case Medium ( $d_e = 0.5 \text{ mm}$ ). Results from the <i>Gauss</i> , <i>nbg</i> and <i>rwi</i> methods (OpenFOAM code). . . . .	83
5.7 Bubble rise velocity history for the case Small ( $d_e = 0.3 \text{ mm}$ ). Results from the <i>Gauss</i> , <i>nbg</i> and <i>rwi</i> methods (OpenFOAM code). . . . .	84
5.8 Bubble rise velocity history for the case Large ( $d_e = 0.9 \text{ mm}$ ). Results from the <i>hf</i> method (Gerris Flow Solver code). . . . .	84
5.9 Bubble rise velocity history for the case Medium ( $d_e = 0.5 \text{ mm}$ ). Results from the <i>hf</i> method (Gerris Flow Solver code). . . . .	85
5.10 Bubble rise velocity history for the case Small ( $d_e = 0.3 \text{ mm}$ ). Results from the <i>hf</i> method (Gerris Flow Solver code). . . . .	85
5.11 Velocity vector field around the bubble for the case Large ( $d_e = 0.9 \text{ mm}$ ). Results from the Coarse mesh resolution at $t = 0.05 \text{ s}$ . . . . .	87
5.12 Velocity vector field around the bubble for the case Small ( $d_e = 0.3 \text{ mm}$ ). Results from the Coarse mesh resolution at $t = 0.02 \text{ s}$ . . . . .	87
6.1 Schematic of the MIT pool boiling facility. Lateral windows are provided for the HSV (the spherical shape around the ITO heater represents the front and back access windows). The bottom access port is for the IR thermometry. . . . .	90
6.2 Schematic of the ITO heater. . . . .	91
6.3 Schematic of the two possible computational domains (drawing not in scale). . . . .	93
6.4 Schematic of the characteristic dimensions of the bubble during bubble growth. . . . .	96
6.5 Sequence of HSV images for the first bubble. . . . .	97
6.6 Schematic of the characteristic dimensions of the bubble during bubble growth. . . . .	98
6.7 Time evolution of the characteristic dimensions of the three bubbles. The measurements have an accuracy of $\pm 0.04 \text{ mm}$ . . . . .	98

---

**List of Figures**

6.8 Radial distribution of the azimuthally average temperature (averaged between the three bubbles). Curves with empty symbols are after bubble departure. Accuracy of the measured temperature is $\pm 2$ °C, and precision is $< 0.5$ °C. . . . .	99
6.9 Time history of the temperature at the nucleation site. Accuracy of the measured temperature is $\pm 2$ °C. . . . .	100
6.10 Average heat transfer coefficient as a function of the radial size of the integration domain. Average between the three ebullition cycles. Accuracy of the calculated heat transfer coefficient is $\pm 0.8$ kW m $^{-2}$ K $^{-1}$ , and precision $< 0.2$ kW m $^{-2}$ K $^{-1}$ . . . . .	100



---

## List of Tables

---

1.1 Features of the major phase change models found in literature. . . . .	12
3.1 Value of $\rho_\psi$ , $\psi$ , $\gamma_\psi$ and $\phi_\psi$ for the various governing equations. . . . .	33
4.1 Summary of the mesh element sizes. . . . .	57
4.2 Maximum dimensionless velocity and pressure jump obtained in the static bubble simulations at time $t = T_\mu$ . . . . .	60
4.3 Summary of the fluid properties for the capillary wave test case. . . . .	61
4.4 Convergence of the $L_2$ error norm for the air-water capillary wave test case. . . . .	62
4.5 Water properties at saturation pressure of 1 atm ( $T_{\text{sat}} = 373.15$ K). . . . .	63
4.6 Mesh resolutions and results for the Stefan problem. . . . .	64
4.7 Mesh resolutions and results for the sucking interface problem. . . . .	66
4.8 Mesh resolutions and results for the spherical vapor bubble growth problem. . . . .	70
5.1 Characteristics of the three scenarios chosen for the comparative study.	78
5.2 Summary of the mesh element sizes. . . . .	79
5.3 Simulated terminal rise velocities compared with reference data (see Section 5.1). Large and Medium cases. . . . .	81
5.4 Simulated terminal rise velocities compared with reference data (see Section 5.1). Small case. . . . .	82
6.1 Thermo-physical properties of water, ITO and sapphire at 100 °C. . . . .	92



---

# CHAPTER **1**

---

## **Introduction**

---

Two-phase heat and mass transfer phenomena play an important role in several natural processes and engineering systems. Knowledge about the mechanisms governing such phenomena is therefore of interest for the understanding of our environment and for the design of safe and efficient technical components. As a consequence, researchers and engineers have continuously performed experiments and developed mathematical models for the description of such phenomena. In spite of all their efforts, many of the physical phenomena that occur during two-phase heat and mass transfer and their interaction are still not well understood. Accordingly, current efforts are directed towards higher resolution experiments and numerical models in order to provide better understanding of two-phase heat and mass transfer processes. In the recent years, the spatial and temporal resolutions of the experiments have continuously increased while few high resolution mechanistic predictive tools, to be used in parallel to the experiments, have been developed. The development of reliable and flexible high resolution numerical models is thus an active field of research nowadays.

The present thesis is a contribution to this common goal by suggesting a numerical framework for the simulation of phase change phenomena. Due to the wide field of applications making use of two-phase heat and mass transfer, the proposed phase change model is focused on boiling phenomena. However, the developed model may be easily extended to other types of heat and mass transfer phenomena thanks to the flexibility of the code used.

## **1.1 Relevance of two-phase heat and mass transfer in energy applications**

---

It is worthless to mention that heat transfer phenomena play a major role in energy applications. On the other hand, two-phase heat and mass transfer such as boiling and condensation are relevant for systems requiring highly efficient heat transfer. As an example, the generation of electrical power from large scale power plants highly relies on boiling to transform into mechanical energy the large amount of heat released from nuclear reactions or from the combustion of fossil fuels. On smaller scales, boiling and condensation are used in refrigeration and heat pump devices as well as in the cooling of high-performance electronics. In effect, the high heat transfer coefficients obtainable using such phase change phenomena allow the design of heat exchangers with reduced dimensions with respect to single-phase heat exchangers. The lower temperatures achievable also allow to maintain the integrity of materials in high-temperature environments.

Boiling and condensation phenomena have been studied extensively during the second half of the twentieth century. These studies have mainly lead to empirical correlations that have driven the design strategy in the sector for a long time. However, in the particular case of boiling, it is almost known that these correlations fail to predict performances in situations that go beyond the range over which the correlations have been developed. This is mainly due to the lack of understanding of the phenomena occurring at the liquid-vapor interfaces at and near the heated surfaces. In a very interesting paper (Nelson, 2001), the author pointed out that progress in mechanistic predictive tools will not be possible without a better understanding of the physical phenomena occurring in the whole process and without resolving its temporal and spatial variations. During the last decade, with the ever increasing computational resources and quality of measurement techniques, researchers have thus started investigating the use of numerical simulations to describe such phenomena, while providing consistent information about the mechanisms involved using higher resolution experiments.

A brief description of boiling phenomena, useful for identifying the various issues related with their understanding, will be given in the followings. For a comprehensive overview of boiling and condensation phenomena, the reader is directed towards some reference textbooks on the topic (Rohsenow et al., 1998; Collier and Thome, 1994; Stephan, 1992).

## **1.2 Boiling phenomena**

---

The typical equation that relates the heat transferred,  $Q$ , from a solid surface to a bulk liquid is given as

$$Q = hS(T_{\text{wall}} - T_{\text{bulk}}), \quad (1.1)$$

where  $h$  is the heat transfer coefficient,  $S$  is the surface area involved in the heat transfer and  $(T_{\text{wall}} - T_{\text{bulk}})$  is the wall superheat. From this relation, we can easily observe that heat transfer can be increased in three different ways: by increasing the heat transfer coefficient, the surface area, or the wall superheat. Increasing the wall superheat is usually limited by the integrity of the materials while increasing the surface area is

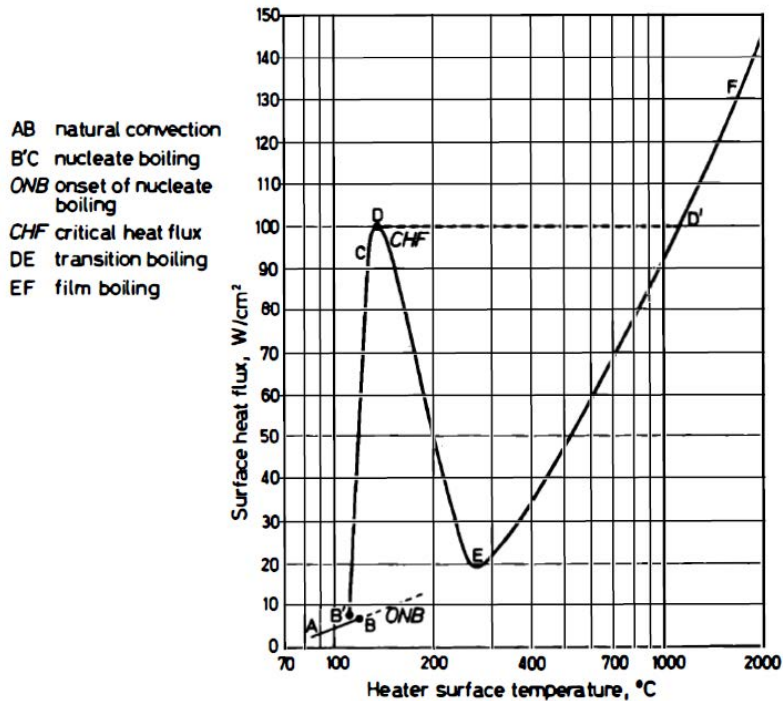


**Figure 1.1:** Pool boiling curve for water at atmospheric pressure (Collier and Thome, 1994).

limited by the dimensions, weight and cost of the heat exchanger. The most efficient way of improving heat transfer is therefore to increase the heat transfer coefficient. This is exactly what occurs during boiling heat transfer and a simple way of describing it is to analyze the pool boiling heat transfer.

Pool boiling is defined as boiling from a heated surface submerged in a large volume of stagnant liquid. The term saturated pool boiling is employed when the temperature of the liquid is at its boiling point, while the term subcooled pool boining is used when the temperature of the liquid is below its boiling point. The results of investigations into heat transfer rates in pool boiling are usually plotted on a graph of surface heat flux ( $q'' = Q/S$ ) against heater wall surface temperature ( $T_{wall}$ ) or wall superheat – the “boiling curve”. Such a diagram has been firstly proposed by Nukiyama (1934) and is often referred to as the “Nukiyama’s curve”. The boiling curve for water at atmospheric pressure is shown qualitatively in Figure 1.1.

The various regions of the curve are well known and helps to identifies the different regimes observed during pool boiling. Some of these regimes are also observed in other configurations. Figure 1.2 gives an overview of each region.

- 1. Natural convection (AB):** In this region, heat is removed by natural convection in the pool and then by evaporation at the free surface.
- 2. Onset of nucleate boiling (ONB):** The wall superheat becomes sufficient to cause the nucleation of vapor bubbles at the microscopic cavities of the heating surface. The drop in surface temperature from B to B' depends on several parameters such as the type of fluids, the properties and characteristics of the heating surface or the operating pressure.

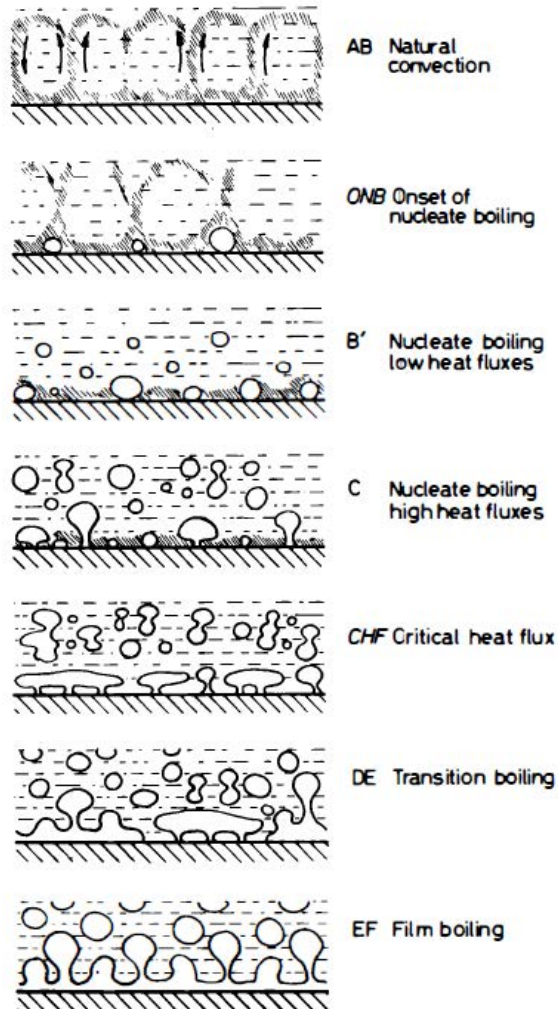


**Figure 1.2:** Pool boiling curve for water at atmospheric pressure (Collier and Thome, 1994).

3. **Nucleate boiling (B'C):** In this region, nucleation of vapor bubbles continuously occur at the heating surface. At low heat flux, few individual nucleation sites are activated. As the heat flux increases, the wall superheat increases and more nucleation sites are activated. As a results bubbles coalesce and at high heat fluxes vapor patches and columns are formed close to the heating surface. Due to the different vapor structure, this region is often subdivided into nucleate boiling at low to moderate heat fluxes and nucleate boiling at high heat fluxes.
4. **Critical heat flux (CHF or point D):** As the heat flux increases, more and more liquid is substituted by vapor on the heating surface, until a stable vapor layer forms and completely separate the heating surface from the liquid. Vapor nucleation is therefore prevented and in the case of heat flux controlled heating, the temperature of the heating surface increases drastically until point D' is reached. Knowledge of the critical heat flux for a given combination of heating surface characteristic and fluids is therefore important to maintain the integrity of the materials and thus of the heat exchanger.

5. **Transition boiling (DE):** In this region, the vapor layer over the heating surface is unstable and releases large patches of vapor at more or less regular intervals. The existence of this region is possible only in conditions approximating constant surface temperature.
6. **Leidenfrost point (E):** The onset of stable film boiling is determined by the Leidenfrost point, which is also the point at the lowest heat flux when vapor completely cover the heating surface. At this wall superheat, droplets bounce off or hover above the heating surface without wetting it.
7. **Film boiling (EF):** In this regime the vapor layer over the heating surface is stable. As liquid approaches the heating surface, the vapor generation increases and the liquid is pushed away from the wall until a vapor bubble is released. The liquid never wet the heating surface and regularly spaced bubbles form periodically. Heat transfer is accomplished principally by conduction and convection through the vapor film with radiation becoming significant as the surface temperature is increased.

The most interesting regime for industrial applications is nucleate boiling due to the high heat transfer coefficients achievable with low superheat. Maintaining small temperature differences in heat exchangers is an approach to optimize the efficiency of a thermodynamic cycle for power generation or heating and cooling. Though the nucleate boiling regime is widely used, it is also the most complex regime and several of its related phenomena are still not well understood.

After the pioneering work of Han and Griffith (1965a,b), several attempts have been made to describe the governing mechanisms during nucleate boiling heat transfer. In the last years, with the significantly increased knowledge about boiling processes, Stephan and Kern (2004) and Kim (2009) proposed the following mechanisms for the transport of heat from the wall into the fluid:

- **Enhanced convection:** The periodic growth and release of bubbles from nucleation sites induces a motion of the liquid layer in proximity to the heating surface. Heat transfer due to convection is therefore increased with respect to natural convection.
- **Transient conduction:** During the bubble growth, the largest amount of heat is supplied by the superheated liquid layer near the heating surface. This heat is progressively absorbed through evaporation at the liquid-vapor interface and the temperature of the liquid drops. During and after the bubble detachment, the depleted liquid layer is restored and its temperature increases through conduction from the heating surface into the liquid.
- **Microlayer evaporation:** One of the pioneering work suggesting the presence of a microlayer underneath the bubble is due to Cooper and Lloyd (1969). With the increasing spatial and temporal resolutions of the experiments, evidences of the presence of this microlayer have been provided. Close to the three-phase contact line, i.e., where the liquid-vapor interface meets the solid surface, a thin liquid layer of some micrometers subsists during the growth of the bubble. This thin layer progressively evaporates and contributes to the total heat absorbed through

evaporation by the bubble. Stephan and Kern (2004) and Kim (2009) state that this contribution from the microlayer can account for up to 20 to 30% of the total heat transferred.

## **1.3 State of the art**

---

### **1.3.1 Related experimental work**

Boiling is one of the most studied physical phenomena in science and engineering. From the early works of Jakob and Fritz (1931), Fritz (1935) and Nukiyama (1934) up to the present day, there is a bewildering number of papers in the literature. In the followings, a brief review of the most relevant experimental studies will be given and does not claim to be exhaustive.

During the second half of the twentieth century, some of the most important and widely used correlations for the prediction of pool boiling heat transfer coefficients have been developed. Empirical models based on dimensionless groups have been proposed by Rohsenow (1952) and Forster and Zuber (1955). Rohsenow's correlation introduces an empirical coefficients to account for the differing nucleation properties of specific liquid-surface combinations. A detailed study of these coefficient for various liquid-surface combinations and various surface preparation techniques has been reported by Vachon et al. (1967b,a). On the other hand, Forster and Zuber's correlations does not account for the heater surface-fluid combination. Some years later, Stephan and Abdelsalam (1980) developed a series of correlations obtained from regression analysis of about 5000 known experimental data. Four groups of substances were identified: hydrocarbons, cryogenic fluids, refrigerants and water. For each group, a different set of dimensionless quantities were chosen, motivated by the fact that a unique correlation is less accurate. In parallel, empirical models based on the law of corresponding states have also been proposed (Mostinski, 1963; Cooper, 1984; Gorenflo et al., 1990). The advantage of such correlations is their simplicity and robustness while varying fluid properties and surface characteristics. Several other correlations have also been proposed for the prediction of the number of active nucleation sites (Mikic and Rohsenow, 1969; Benjamin and Balakrishnan, 1997), the bubble departure diameters (Zuber, 1963; Cole, 1967; Mikic and Rohsenow, 1969) and the bubble departure frequencies (Cole, 1967; Mikic and Rohsenow, 1969; Malenkov, 1972).

Most of the above mentioned correlations rely on empirical coefficients which are valid only for a specific fluid-heating surface combination and a certain range of operating conditions, which limits their applications to other fluids and parameter ranges. However, in absence of more sophisticated predictive models, these correlations are still used for design purposes. A way of improving the reliability of these correlations is to improve the understanding of the governing mechanisms. Experiments focusing on some aspects of nucleate boiling, with progressively higher resolution techniques, have therefore been performed.

With the introduction of high-speed infrared thermometry by Theofanous et al. (2002a,b), investigation of local quantities such as local wall temperature and heat transfer underneath a nucleating bubble has been made possible. Another high-resolution approach using arrays of micro-heater has also been proposed recently by Demiray and Kim (2004) to allow information on the local heat transfer at the bubble foot. The use

of thermochromic liquid crystals have also permitted high resolutions measurements of local quantities (Kenning and Yan, 1996; Kenning et al., 2001). More recently, Buongiorno's group provided high-resolution data of bubble dynamics and heat transfer in pool boiling of water using synchronized high-speed video and infrared thermometry (Gerardi et al., 2010; Duan et al., 2013).

Deeper insights to the dynamics of the microlayer underneath the nucleating bubble and its contribution to the total heat transfer have also been possible with the introduction of high-resolution experiments. In Schweizer and Stephan (2009), the maximum local heat flux is observed at the three-phase contact line and can reaches one or even more orders of magnitude higher values than the average heat flux. Several experiments also indicate that the heat transfer at the three-phase contact line strongly depends on its motion direction and speed (Myers et al., 2005; Moghaddam and Kiger, 2009a,b; Delgoshaei and Kim, 2010). Very recently, Kunkelmann et al. (2012) proposed a combined experimental and numerical study of the influence of the three-phase contact line dynamics on the total heat transfer. All these studies have revealed an increasing local heat transfer while the three-phase contact line advance during bubble detachment. Using high-speed infrared thermometry, Kim and Buongiorno (2011) have also been able to measure the temporal and spatial variation of the microlayer thickness.

All the high resolution experiments performed recently have permitted to increase our knowledge about the mechanisms involved in nucleate boiling and to quantify their influence on the total heat transfer in some configurations. Nevertheless, some limitations in the spatial and temporal resolutions of the different measurement techniques still not allow the complete description of the local heat transfer near the heating surface and the detailed measurement of the liquid temperature surrounding the vapor bubble. On the other hand, boiling research is also focusing on the investigation of micro-structured surfaces as well as nano-fluids for enhanced nucleate boiling heat transfer. However the results obtained with a particular surface geometry and fluid usually cannot be used directly to predict the heat transfer with different fluids and operating conditions. As a consequence there is still a need to further understand the physical mechanisms involved in boiling in order to reduce the degree of empiricism and the number of experimental tests to find optimal parameters.

### **1.3.2 Modeling approaches at the interface scale**

The simulation of a two-phase flow at the interface scale, also referred to as the direct numerical simulation of a two-phase flow, generally relies on a specific interface tracking technique in order to follow the evolution of the interface and to account for the interfacial jumps and forces such as surface tension. In the framework of fixed Eulerian grids, the so-called one-fluid method is generally adopted (Hirt and Nichols, 1981; Unverdi and Tryggvason, 1992; Sussman et al., 1994). In such framework, a single set of governing equations is solved for both fluids through the use of a Heaviside function which identifies the spatial distribution of the phases. In most cases, a smooth version of the Heaviside function is reconstructed, i.e., the boundary conditions at the interface are distributed over the control volumes surrounding the interface. It is however possible to represent a sharp Heaviside function if specific numerical treatments are adopted. For instance, in the Ghost Fluid Method (Fedkiw et al., 1999; Kang et al., 2000; Liu et al., 2000) the boundary conditions at the interface are reconstructed at the cell center,

## Chapter 1. Introduction

---

providing a sharp treatment of the interfacial boundary conditions.

To include the effects of surface tension, various models have been developed. In particular, a proper calculation of the interfacial curvature is relevant for surface tension driven flows. Several calculation methods exist and are often related to the interface tracking method adopted in the two-phase model.

Finally, to evaluate the heat and mass transfer, various phase change modeling approaches have been developed. Due to the various types of phase change phenomena and their relative complexity, the present thesis is focused mainly on boiling phenomena. Some of the method developed for simulating boiling phenomena may however be extended to other kinds of phase change phenomena.

A two-phase flow model able to deal with heat and mass transfer at the interface scale should therefore include three main features:

1. an interface tracking technique;
2. a surface tension model;
3. a phase change model.

Some of the most used methods will be described in the following.

### Interface tracking techniques

The main techniques reported in the literature can be classified by the representation of the interface adopted. Methods such as Level-Set (LS) (Sussman et al., 1994) and Volume-Of-Fluid (VOF) (Hirt and Nichols, 1981; Scardovelli and Zaleski, 1999) track the interface implicitly from data computed on a fixed Eulerian mesh. On the other hand, methods such as Front Tracking (FT) (Unverdi and Tryggvason, 1992) explicitly track the interface using a moving Lagrangian surface mesh. Implicit methods such as LS or VOF are generally characterized by automatic merging or breakup of the two-phase interface. This feature can be undesired in some circumstances, however it can be compensated using, for instance, Adaptive Mesh Refinement (AMR) techniques. On the other hand, explicit methods require the implementation of a sub-grid model in order to handle the merging and breakup of the two-phase interface. In the absence of a sub-grid model, these methods are well suited for the study of swarm effects (Tryggvason et al., 2001; Roghair et al., 2011). Each interface tracking technique presents advantages and drawbacks that will be briefly described here.

The LS method represents the interface as the zero level set of a distance function from the interface. Its evolution is obtained from the advection of the distance function. The relative simplicity of the method is offset by mass conservation issues, especially in flows with high vorticity (van Sint Annaland et al., 2006). The VOF method is based on the transport of a color function, often referred to as the volume fraction, that represents the relative amount of one of the phases at a given location. The transport equation of the volume fraction is derived from the continuity equation, resulting in strong mass conservation. However, due to the sharp nature of the volume fraction, numerical diffusion readily occurs. One family of VOF methods employs specific high-resolution schemes and an anti-diffusive term that tends to reduce the numerical diffusion over two to three mesh elements (see e.g., Ubbink and Issa (1999)). The mass conservative method recently proposed by Sato and Ničeno (2012) is also similar to these VOF

methods. Another family of VOF methods, also known as geometrical VOF, performs a geometrical reconstruction and advection of the interface, leading to a sharp representation. Early work on these methods is attributed to Noh and Woodward (1976) and Hirt and Nichols (1981), where the interface is represented using the Simple Line Interface Calculation (SLIC) algorithm. Later, Youngs (1982) introduced the concept of Piecewise Linear Interface Calculation (PLIC) algorithms where the interface is represented through line elements in 2D or planes in 3D. Modern PLIC VOF methods (see e.g., Popinet (2009)) have proven to be accurate enough and efficient enough to simulate a wide range of surface tension driven applications. In order to combine the strong points of the VOF and LS methods, Sussman and Puckett (2000) also proposed a Coupled Level-Set Volume-Of-Fluid (CLSVOF) algorithm. Finally, the FT technique represents the interface explicitly using a series of connected points constituting surface meshes. The inherent accuracy and robustness of the method is offset by its complicated implementation due to the requirement for dynamic remeshing and mapping of the interface mesh onto the fixed mesh that is used to solve the Navier–Stokes equations (van Sint Annaland et al., 2006).

### Surface tension models

The proper estimation of the interface curvature and the proper implementation of the surface tension forces are relevant for surface tension dominant flows. The Continuum Surface Force (CSF) method proposed by Brackbill et al. (1992) is one of the most widely adopted implementations of surface tension forces in the VOF (Renardy and Renardy, 2002) and LS (Sussman et al., 1994; Sussman and Puckett, 2000) techniques. In this method, the surface tension forces are added to the momentum equation as a body force localized near the interface, via a smoothed delta function. Improvements in the implementation of the CSF method have been achieved by Francois et al. (2006) through the introduction of discrete exact balances between the pressure gradients and the surface tension forces. An estimate of the local interfacial mean curvature is required within the CSF method and is often obtained from the gradient of the interface normal vector using finite difference approximations (Brackbill et al., 1992; Sussman et al., 1994; Sussman and Puckett, 2000; Renardy and Renardy, 2002). On unstructured meshes, finite volume approximations using the Gauss theorem, which reduce to finite difference approximations on orthogonal meshes, are generally applied to estimate the derivatives. However, such estimates of the interfacial mean curvature are relatively inaccurate, in particular when a sharp function, such as the volume fraction, is used. This principally leads to the generation of unphysical velocities near the interface, i.e., the so-called spurious currents (Scardovelli and Zaleski, 1999; Popinet and Zaleski, 1999).

More accurate estimates are obtained using higher order methods. For instance, in the PROST method proposed by Renardy and Renardy (2002), local parabolic reconstructions of the interface are performed by least-squares fitting of a quadratic surface to the volume fraction, providing second order accurate estimates of the interfacial mean curvature. Within the VOF interface tracking framework, the height function method, initially proposed by Torrey et al. (1985), shows in addition second order accuracy. In this method, approximations of the local interface position are obtained from local volume integrals of the volume fractions. The interfacial mean curvature is then computed from the local interface positions, i.e., local height functions, using centered

## Chapter 1. Introduction

---

finite differences. Due to the nature of the height function calculations, i.e., discrete sums along the direction of the largest component of the interface normal vector, the method is restricted to orthogonal meshes. Because no fitting is required, the height function method is faster than parabolic reconstruction algorithms, especially in three dimensions. However, when the interface is under-resolved, i.e., when the radius of curvature of the interface is comparable to the mesh size, consistent height functions cannot be found. To overcome this problem, Popinet (2009) recently proposed a generalized height function technique where under-resolved interfaces are treated appropriately through parabolic reconstruction. The method is embedded in the Gerris Flow Solver open source code (Popinet, 2003).

To avoid the generation of spurious currents at the interface, Raeini et al. (2012) proposed a Filtered Surface Force (FSF) method. It is derived from the CSF method, however a filtering procedure is applied to remove the capillary forces that are parallel to the interface. Though some amount of capillary forces are removed artificially, the method is particularly effective for the simulation of two-phase flows with very low capillary numbers such as in porous media. Another advantage of the method is its compatibility with any interfacial curvature calculation methods.

### Phase change models

The first CFD model simulating boiling is attributed to Welch (1995), where the liquid-vapor interface is represented in two dimensions by the boundary between two moving computational domains discretized using triangular meshes. Since the interface is explicitly tracked as a boundary, the interfacial jumps and the mass transfer rate are directly computed at the interface and included as boundary conditions within each phase. In Welch (1998), the method is further applied to the simulation of nucleate boiling and the homogeneous vapor bubble growth benchmark is introduced. However the method is limited to small interface deformation without topology change. In order to simulate large interface deformation, interface tracking methods, such as the ones introduced previously, are adopted. In Son and Dhir (1998), a LS method is used, while a VOF and a FT method is employed in Welch and Wilson (2000) and Juric and Tryggvason (1998), respectively. These models are applied to the simulation of two-dimensional film boiling. Various one-dimensional benchmarks with analytical solutions are introduced also in Welch and Wilson (2000), such as the Stefan problem and the sucking interface problem.

Various phase change models coupled with the LS method have been continuously developed and improved after the initial work of Dhir's group Son and Dhir (1998). In Son et al. (1999), a sub-grid model for micro layer evaporation is included into the original model and is applied to nucleate boiling on a horizontal surface. Merging processes during nucleate boiling are also analyzed in Son et al. (2002), Mukherjee and Dhir (2004) and Dhir (2006) using this model. In Mukherjee and Kandlikar (2007) the dynamic contact angles effects during pool boiling are analyzed. An improved model based on the Ghost Fluid Method and an Immersed Boundary Method (Son, 2005) is introduced in Son and Dhir (2007) and Son and Dhir (2008b) for the simulation of film boiling over a horizontal cylinder. Simulation of nucleate boiling with high heat fluxes and sub-cooled pool boiling are also undertaken with the improved model in Son and Dhir (2008a) and Wu and Dhir (2011), respectively. In addition to the model of Dhir's

group, Gibou et al. (2007) developed a phase change model based on the LS method and the Ghost Fluid Method, with application to the simulation of two-dimensional film boiling. Tanguy et al. (2007) also developed a similar model with application to the evaporation of a water droplet in air. The main drawback of phase change models coupled with the LS method is that conservation of mass is not strictly guaranteed due to the interface tracking approach.

The phase change model coupled with the FT technique introduced in Juric and Tryggvason (1998) is modified and applied to the study of film boiling in Esmaeeli and Tryggvason (2004a) and Esmaeeli and Tryggvason (2004b). An Immersed Boundary Method is also implemented to deal with complex solid geometries and simulation of film boiling over horizontal cylinders is performed in Esmaeeli and Tryggvason (2004c). Despite the model is demonstrated to be reliable, the implementation of the FT method with treatment of topology changes at the liquid-vapor interface is complicated.

The VOF-based phase change model of Welch and Wilson (2000) is used in Welch and Rachidi (2002) to simulate film boiling with conjugate heat transfer and in Agarwal et al. (2004) to study the periodic bubble release during film boiling in two dimensions. In Yuan et al. (2008), a VOF-based phase change model is extended to non-orthogonal body-fitted coordinates in order to simulate film boiling on a sphere. These phase change models compute the mass transfer rate directly from the heat flux at the interface. In contrast, a phase change model based on the evaporation heat transfer coefficient proposed by (Schrage, 1953) is developed in Hardt and Wondra (2008). In this phase change model, a smearing-out of the mass transfer rate is also performed over few cells around the interface in order to stabilize the solution. The mass transfer rate is also shifted to the liquid side and to the vapor side to account for disappearance and creation of mass. This shifting generates error in the velocity, pressure and temperature fields because the mass transfer does not occur at the interface itself but in the liquid side and in the vapor side respectively. The model therefore requires a finer mesh with respect to the other existing phase change models. However it is more flexible with respect to the type of mesh and to the interface tracking technique adopted, which is an advantage for an implementation within a general purpose CFD software. In effect, the method has been implemented successfully in the OpenFOAM® open-source CFD toolbox by Kunkelmann and Stephan (2009). Three-dimensional film boiling and nucleate boiling simulation are performed. The model is also modified in Kunkelmann and Stephan (2010b) and Kunkelmann and Stephan (2010a) to compute the mass transfer rate directly from the heat flux at the interface by introducing a level set reconstruction method. As described in Kunkelmann (2011), computing the mass transfer directly from the heat flux at the interface is more accurate when the interface is well-resolved, such as in nucleate boiling simulations. On the other hand, the calculation of the mass transfer rate through the evaporation heat transfer coefficient is proven effective when the interface is under-resolved or when high heat fluxes are present such as in film boiling simulations. The Hardt and Wondra approach is also implemented in the commercial ANSYS® FLUENT® code in Magnini and Pulvirenti (2011), Magnini et al. (2013a) and Magnini et al. (2013b). In these studies, evaporation of elongated bubbles in microchannels are investigated. The particularity of the method is a self-implementation of the height function method for interfacial curvature calculation in order to increase the stability and accuracy of surface tension modeling.

## Chapter 1. Introduction

---

**Table 1.1:** Features of the major phase change models found in literature.

	Interface tracking method	Mass conservative	Automatic topology changes	3D simulation	Unstructured mesh	Adaptive mesh refinement	Sharp mass transfer	Mass transfer rate calculation
Dhir's group	LS	no	yes	yes	no	no <sup>a</sup>	yes	DHT <sup>b</sup>
Tryggvason's group	FT	no	no	yes	no	no <sup>a</sup>	yes	DHT <sup>b</sup> and EC <sup>c</sup>
Welch's group	VOF-PLIC	yes	yes	no	no	no <sup>a</sup>	yes	DHT <sup>b</sup>
Stephan's group	VOF	yes	yes	yes	yes	yes	no	DHT <sup>b</sup> and EC <sup>c</sup>
Magnini et al.	VOF-PLIC	yes	yes	yes	yes	yes	no	EC <sup>c</sup>
Sato and Ničeno	VOF-CIP <sup>d</sup>	yes	yes	yes	no	no	yes	DHT <sup>b</sup>

<sup>a</sup> Staggered grid formulation renders adaptive mesh refinement a complicated task.

<sup>b</sup> Direct calculation from interfacial heat flux.

<sup>c</sup> Calculation using the evaporation heat transfer coefficient approach.

<sup>d</sup> Advection of the VOF using the CIP-CSL2 scheme (Nakamura et al., 2001).

Phase change models coupled with other types of interface tracking techniques have also been proposed. In Tomar and Biswas (2005), a Coupled Level-Set Volume-Of-Fluid interface tracking method is employed and simulations of film boiling in two dimensions are analyzed. The method is mass conservative however no validation test cases are presented. Very recently, Sato and Ničeno (2013) proposed a phase change model coupled with the mass conservative interface tracking technique developed in Sato and Ničeno (2012). The phase change model is based on direct estimation of the heat flux at the interface and a sharp temperature field is solved using a discretization similar to the Ghost Fluid Method. Several test cases are presented and three-dimensional simulations of nucleate boiling are performed. The method is however limited to uniform Cartesian grids.

A summary of the major phase change models found in literature and their features is given in Table 1.1.

## 1.4 Objectives

---

The general objective of the present thesis is to develop and validate a numerical model for the simulation of two-phase heat and mass transfer for applications within the energy sector. As such, the thesis will focus on simulation of boiling phenomena due to its wide use and importance in the production and conversion of energy. The developed model is intended to be used in parallel with high resolution experiments in order to provide deeper insights into the mechanisms governing boiling heat transfer and thus to reduce the number of trials while optimizing the design of heat exchangers.

Different approaches are available for the implementation of such a numerical model into a CFD code. While it is possible to develop a specific stand-alone application, it is preferred to implement the model within the open-source CFD toolkit OpenFOAM® for a higher sustainability and usage of the model. The structure of the code is highly flexible, parallelizable and compatible with general polyhedral meshes. It has also a large community of users and developers which participates actively to the continuous improvement of the CFD libraries available.

The VOF interface tracking method is adopted due to its wide usage, conservative property and robustness. A VOF method employing a high-resolution scheme and an anti-diffusive term is already implemented within OpenFOAM libraries. Extension of the method to deal with boiling phase change is therefore required. The verification and validation of the model will be performed following typical benchmarks using analytical solutions. Both the isothermal and phase change parts of the model will be analyzed. The method of verification and validation follows the Q<sup>3</sup> approach proposed by Colombo et al. (2012).

In order to assess the accuracy of the two-phase model in practical cases, spherical rising bubbles will be investigated. The results will be compared with theoretical correlations and experimental data available in literature. Finally, a benchmark for the simulation of nucleate pool boiling will be developed using experimental data obtained at the MIT pool boiling facility, where part of the present thesis has been achieved with the support of the “Progetto Roberto Rocca” joint MIT–Politecnico di Milano research program.

---

## 1.5 Novel contributions in this thesis

The present thesis proposes a novel numerical framework for the simulation of two-phase heat and mass transfer which consists of the following features:

- the VOF interface tracking technique is used with a compressive high resolution scheme;
- the method is mass conservative;
- interface topology changes are treated automatically;
- the method is both two- and three-dimensional;
- unstructured mesh are employed;
- adaptive mesh refinement is possible in three-dimension;
- the sources due to mass transfer are treated in a sharp way;
- the calculation of the mass transfer rate is performed directly from the heat fluxes at the interface (DHT).

The method implemented is similar to the method developed by the Stephan’s group, however a sharp treatment of the sources due to mass transfer is adopted here. This permits to reduce the error in the velocity and temperature fields near the interface and to reduce the global number of mesh elements because the regions of interest, requiring high spatial resolution, are more concentrated around the interface.

## **Chapter 1. Introduction**

---

In addition to these features, two interfacial curvature calculation methods are proposed in order to reduce the spurious velocities near the two-phase interface and to increase the accuracy of the capillary forces estimates. These methods are compared to reference data and to the height function method implemented in the Gerris Flow Solver code (Popinet, 2009).

A detailed analysis of isothermal spherical rising air bubbles in water is also performed with proper identification of the reference data to be used.

Finally, a benchmark for the simulation of nucleate boiling is developed using the experimental data obtained at the pool boiling facility of the Department of Nuclear Science and Engineering of the Massachusetts Institute of Technology.

---

# CHAPTER 2

---

## Governing equations

---

In this chapter, the governing equations of a two-phase flow with heat and mass transfer are derived. First the local instant conservation equations are obtained. Then the one-fluid formulation is introduced through the use of a Heaviside function and the transport equations that will be solved in the numerical model are retrieved.

### 2.1 Local instant conservation equations

---

In the present study, the standard method of continuum mechanics is followed. As a result, the flow of two immiscible phases is described by two single-phase regions delimited by moving interfaces and solid boundaries. The standard differential balance equations hold for each subregion up to an interface, but not across it. The singular characteristics (discontinuities) in the various variables at an interface are taken into account using appropriate form of the balance equations: the so-called jump conditions. Finally, the problem is define uniquely using additional interfacial boundary conditions and constitutive equations.

#### 2.1.1 General balance equation

The general balance equation of a quantity describing fluid flow can be stated in the differential form, applicable at a point, or in the integral form, applicable to a region. Consider a material volume  $V(t)$  cut by an interface  $A_{\text{int}}(t)$  which divides the material volume  $V(t)$  into sub-volumes  $V_1(t)$  and  $V_2(t)$ , respectively bounded by surfaces  $A_1(t)$  and  $A_{\text{int}}(t)$ , and,  $A_2(t)$  and  $A_{\text{int}}(t)$  (see Figure 2.1). As the volume  $V(t)$  is material,  $A_1(t)$  and  $A_2(t)$  are also material and we have at each point belonging to these surfaces

$$\mathbf{u}_A \cdot \mathbf{n}_k = \mathbf{u}_k \cdot \mathbf{n}_k, \quad (2.1)$$

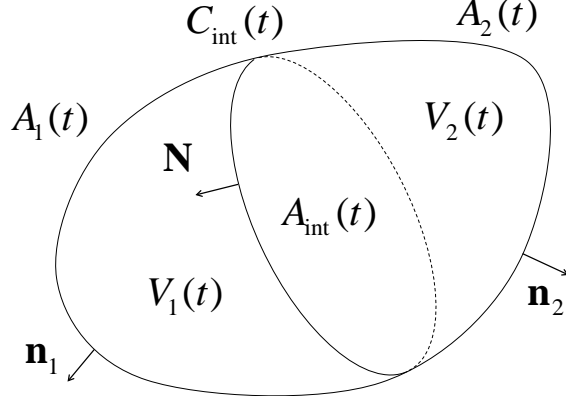


**Figure 2.1:** Material volume  $V(t)$  cut by an interface  $A_{\text{int}}(t)$ .

where  $\mathbf{n}_k$  is the outward-pointing unit normal vector of the surface,  $\mathbf{u}_A \cdot \mathbf{n}_k$  the speed of displacement of the surface and  $\mathbf{u}_k$  the velocity of a particle, with  $k = 1, 2$  designing the  $k$ -th phase. The interface  $A_{\text{int}}(t)$ , delimited by the curve  $C_{\text{int}}(t)$ , is not a material surface and mass transfer may occur between the sub-volumes  $V_1(t)$  and  $V_2(t)$ . Defining  $\mathbf{u}_{\text{int}}(\mathbf{x}, t)$  the velocity of the interface, the mass transfer per unit surface from the  $k$ -th phase to the other phase is defined as

$$\dot{m}_k'' = \rho_k (\mathbf{u}_k - \mathbf{u}_{\text{int}}) \cdot \mathbf{n}_k. \quad (2.2)$$

with  $\rho_k(\mathbf{x}, t)$  the density of the  $k$ -th phase. Note that by definition  $\dot{m}_1'' = -\dot{m}_2''$ .

The general integral balance of any specific quantity  $f_k = f_k(\mathbf{x}, t)$  of the  $k$ -th phase can be written introducing the surface flux  $\mathbf{J}_k$  and the volume source  $\phi_k$ . This gives

$$\frac{d}{dt} \int_{V_k(t)} \rho_k f_k dV = - \oint_{\partial V_k(t)} \mathbf{J}_k \cdot \mathbf{n}_k dA + \int_{V_k(t)} \rho_k \phi_k dV - \int_{A_{\text{int}}(t)} \dot{m}_k'' f_k dA. \quad (2.3)$$

The left-hand side represents the time rate of change of  $\rho_k f_k$  within  $V_k(t)$ . The first term of the right-hand side is the influx through  $\partial V_k(t)$  (which does not include mass transfer), the second term is the volume source and the last term is the influx due to mass transfer at the interface. Using the Reynolds' transport theorem, which is a three-dimensional generalization of the Leibniz's integral rule, and the Gauss's theorem, the differential form of the balance equation can be obtained. The Leibniz's integral rule shows how to differentiate under the integral sign, provided that both the integrand  $F$  and its partial derivative are sufficiently smooth. It is given as

$$\frac{d}{dx} \int_{\alpha(x)}^{\beta(x)} F(x, y) dy = \int_{\alpha(x)}^{\beta(x)} \frac{\partial F}{\partial x} dy + F(x, \beta(x)) \frac{d\beta}{dx} - F(x, \alpha(x)) \frac{d\alpha}{dx}, \quad (2.4)$$

Generalizing the above equation to three dimensions, the Reynolds' transport theorem is obtained and reads

$$\frac{d}{dt} \int_{V(t)} F dV = \int_{V(t)} \frac{\partial F}{\partial t} dV + \oint_{\partial V(t)} F \mathbf{u}_A \cdot \mathbf{n} dA. \quad (2.5)$$

where  $\mathbf{u}_A \cdot \mathbf{n}$  is the surface displacement velocity of  $\partial V(t)$ .

## 2.1. Local instant conservation equations

---

The Gauss's theorem gives the relation between the flux of a quantity through a closed surface and its behavior within the surface. For a vector or tensor field of any order  $\mathbf{F}$ , the Gauss's theorem states that

$$\int_{V(t)} \nabla \cdot \mathbf{F} dV = \oint_{\partial V(t)} \mathbf{F} \cdot \mathbf{n} dA, \quad (2.6)$$

while for a scalar field  $F$ , the theorem is

$$\int_{V(t)} \nabla F dV = \oint_{\partial V(t)} F \mathbf{n} dA. \quad (2.7)$$

In view of Eqs. (2.3) and (2.5) the general balance equation becomes

$$\begin{aligned} & \int_{V_k(t)} \frac{\partial \rho_k f_k}{\partial t} dV + \oint_{\partial V_k(t)} \rho_k f_k \mathbf{u}_A \cdot \mathbf{n}_k dA \\ &= - \oint_{\partial V_k(t)} \mathbf{J}_k \cdot \mathbf{n}_k dA + \int_{V_k(t)} \rho_k \phi_k dV - \int_{A_{\text{int}}(t)} \dot{m}_k'' f_k dA. \end{aligned} \quad (2.8)$$

As discussed previously, the boundary  $A_k(t)$  of the sub-volume  $V_k(t)$  moves with the fluid, while the interface  $A_{\text{int}}(t)$  can move relative to the fluids due to mass transfer. Hence, the above equation reads

$$\begin{aligned} & \int_{V_k(t)} \frac{\partial \rho_k f_k}{\partial t} dV + \int_{A_k(t)} \rho_k f_k \mathbf{u}_k \cdot \mathbf{n}_k dA + \int_{A_{\text{int}}(t)} \rho_k f_k \mathbf{u}_{\text{int}} \cdot \mathbf{n}_k dA \\ &= - \oint_{\partial V_k(t)} \mathbf{J}_k \cdot \mathbf{n}_k dA + \int_{V_k(t)} \rho_k \phi_k dV - \int_{A_{\text{int}}(t)} \rho_k f_k (\mathbf{u}_k - \mathbf{u}_{\text{int}}) \cdot \mathbf{n}_k dA, \end{aligned} \quad (2.9)$$

which simplifies to

$$\begin{aligned} & \int_{V_k(t)} \frac{\partial \rho_k f_k}{\partial t} dV + \oint_{\partial V_k(t)} \rho_k f_k \mathbf{u}_k \cdot \mathbf{n}_k dA \\ &= - \oint_{\partial V_k(t)} \mathbf{J}_k \cdot \mathbf{n}_k dA + \int_{V_k(t)} \rho_k \phi_k dV. \end{aligned} \quad (2.10)$$

The above general balance equation in integral form is identical to the case without mass transfer. Using the Gauss's theorem Eq. (2.6), the differential form of the general balance equation is obtained

$$\frac{\partial \rho_k f_k}{\partial t} + \nabla \cdot (\rho_k f_k \mathbf{u}_k) = -\nabla \cdot \mathbf{J}_k + \rho_k \phi_k.$$

(2.11)

### 2.1.2 Laws of conservation

The mathematical formulation of the laws of conservation of mass, linear momentum, angular momentum and total energy can be expressed in differential form using the general balance equation (Eq. (2.11)).

### Conservation of mass

In the present study, we do not consider volume sources of mass. Hence, by setting

$$f_k = 1, \quad \mathbf{J}_k = 0, \quad \phi_k = 0, \quad (2.12)$$

the conservation of mass is expressed in differential form as

$$\boxed{\frac{\partial \rho_k}{\partial t} + \nabla \cdot (\rho_k \mathbf{u}_k) = 0.} \quad (2.13)$$

### Conservation of linear momentum

Considering the forces acting on a fluid mass, the conservation of linear momentum can be obtained from Eq. (2.11) by setting

$$f_k = \mathbf{u}_k, \quad \mathbf{J}_k = -\mathbf{T}_k = p_k \mathbf{I} - \mathbf{S}_k, \quad \phi_k = \mathbf{b}_k, \quad (2.14)$$

where the surface stress tensor  $\mathbf{T}_k$ , the pressure term  $p_k \mathbf{I}$ , the viscous stress  $\mathbf{S}_k$  and the body forces  $\mathbf{b}_k$  have been introduced, with  $\mathbf{I}$  the unit tensor. After substitution in Eq. (2.11) we have

$$\boxed{\frac{\partial \rho_k \mathbf{u}_k}{\partial t} + \nabla \cdot (\rho_k \mathbf{u}_k \mathbf{u}_k) = -\nabla p_k + \nabla \cdot \mathbf{S}_k + \rho_k \mathbf{b}_k.} \quad (2.15)$$

Note that the effects of the other phase and surface tension at the interface are taken into account by using proper boundary conditions for  $p_k$  and  $\mathbf{S}_k$  at the interface.

### Conservation of angular momentum

In the absence of body torque or couple stress, which is the case in the present work, all torques arise from the surface stress and the body force (Aris, 1962; Ishii and Hibiki, 2006). Hence, the conservation of angular momentum reduces to

$$\boxed{\mathbf{T}_k = \mathbf{T}_k^\top,} \quad (2.16)$$

which states that the surface stress tensor is symmetric.

### Conservation of total energy

The conservation of total energy can be obtained by setting

$$f_k = \frac{u_k^2}{2} + e_k, \quad \mathbf{J}_k = \mathbf{q}_k - \mathbf{T}_k \cdot \mathbf{u}_k, \quad \phi_k = \mathbf{b}_k \cdot \mathbf{u}_k + \frac{\dot{q}_k'''}{\rho_k}, \quad (2.17)$$

where the velocity magnitude  $u_k$ , the internal energy  $e_k$ , the heat flux  $\mathbf{q}_k$  and the volumetric heat generation rate  $\dot{q}_k'''$  related to the  $k$ -th phase have been introduced. After substitution in Eq. (2.11) we have

$$\boxed{\begin{aligned} & \frac{\partial}{\partial t} \left[ \rho_k \left( \frac{u_k^2}{2} + e_k \right) \right] + \nabla \cdot \left[ \rho_k \left( \frac{u_k^2}{2} + e_k \right) \mathbf{u}_k \right] \\ &= -\nabla \cdot \mathbf{q}_k + \nabla \cdot (\mathbf{T}_k \cdot \mathbf{u}_k) + \rho_k (\mathbf{b}_k \cdot \mathbf{u}_k) + \dot{q}_k'''. \end{aligned}} \quad (2.18)$$

## 2.1. Local instant conservation equations

---

Since the number of dependent variables exceeds that of the field equations, these four local laws of conservation with proper boundary conditions are insufficient to close the problem. Consequently, it is necessary to supplement them with various constitutive equations, that define a certain type of ideal materials, and interfacial jump conditions, that account for the discontinuities at an interface. However, before discussing them, there are some important relations which can be derived from the above equations.

### Mechanical energy equation

By dotting the conservation of linear momentum (Eq. (2.15)) by the velocity and using the conservation of mass (Eq. (2.13)), we can obtain the mechanical energy equation

$$\begin{aligned} \frac{\partial}{\partial t} \left( \rho_k \frac{u_k^2}{2} \right) + \nabla \cdot \left( \rho_k \frac{u_k^2}{2} \mathbf{u}_k \right) \\ = -\nabla p_k \cdot \mathbf{u}_k + (\nabla \cdot \mathbf{S}_k) \cdot \mathbf{u}_k + \rho_k (\mathbf{b}_k \cdot \mathbf{u}_k). \end{aligned} \quad (2.19)$$

### Internal energy equation

By substituting the mechanical energy equation (Eq. (2.19)) from the conservation of total energy (Eq. (2.18)), the internal energy equation is obtained. Furthermore,  $\mathbf{T}_k$  is symmetric thus  $\mathbf{S}_k$  is symmetric and  $\nabla \cdot (\mathbf{S}_k \cdot \mathbf{u}_k) = (\nabla \cdot \mathbf{S}_k) \cdot \mathbf{u}_k + (\mathbf{S}_k \cdot \nabla) \cdot \mathbf{u}_k$ . After simplification, the internal energy equation reduces to

$$\frac{\partial \rho_k e_k}{\partial t} + \nabla \cdot (\rho_k e_k \mathbf{u}_k) = -\nabla \cdot \mathbf{q}_k - p_k \nabla \cdot \mathbf{u}_k + (\mathbf{S}_k \cdot \nabla) \cdot \mathbf{u}_k + \dot{q}_k'''. \quad (2.20)$$

### Enthalpy equation

Introducing the enthalpy of the  $k$ -th phase  $h_k = e_k + p_k/\rho_k$ , the enthalpy equation is obtained from the internal energy equation

$$\begin{aligned} \frac{\partial \rho_k h_k}{\partial t} + \nabla \cdot (\rho_k h_k \mathbf{u}_k) \\ = -\nabla \cdot \mathbf{q}_k + \frac{\partial p_k}{\partial t} + \mathbf{u}_k \cdot \nabla p_k + (\mathbf{S}_k \cdot \nabla) \cdot \mathbf{u}_k + \dot{q}_k'''. \end{aligned} \quad (2.21)$$

### 2.1.3 Constitutive equations

Constitutive equations provide mathematical relations able to describe approximately the behaviors of specific group of materials or substances. They are formulated from experimental observations together with postulated principles such as the entropy inequality, determinism, frame indifference and local action (Ishii and Hibiki, 2006). The principle of determinism expresses the predictability of a present state from a past history. The principle of material frame indifference means that the response of a material is independent of the conditions of observation. The entropy inequality states that the rate of entropy production should be positive, which can be considered as a restriction on the constitutive laws. Finally, the principle of local action states that an object is influenced directly only by its immediate surroundings. As noticed by Ishii and Hibiki (2006), various constitutive equations can be classified into three groups based on their physical significances:

## Chapter 2. Governing equations

---

1. mechanical constitutive equations;
2. energetic constitutive equations;
3. constitutive equation of state.

The viscous stress tensor and the body forces are specified in the first group, whereas the heat flux and heat generation rate are supplied by the second group. The last equation provides a relation between two or more state functions such as the temperature, pressure, volume, or internal energy of the fluid.

In the present study, the following constitutive equations are adopted:

### Mechanical constitutive equation

The fluids are considered as Newtonian, i.e., the viscous stresses depend linearly on the dynamic viscosity  $\mu_k$  of the fluid, which is assumed constant, the rate of strain and the rate of expansion of the flow

$$\mathbf{S}_k = \mu_k (\nabla \mathbf{u}_k + \nabla \mathbf{u}_k^\top) - \frac{2}{3} \mu_k (\nabla \cdot \mathbf{u}_k) \mathbf{I}. \quad (2.22)$$

For an incompressible fluid, the velocity field is solenoidal and the relation reduces to

$$\boxed{\mathbf{S}_k = \mu_k (\nabla \mathbf{u}_k + \nabla \mathbf{u}_k^\top)}. \quad (2.23)$$

The gravitational force is considered as the only body force acting the fluids, thus we have

$$\boxed{\mathbf{b}_k = \mathbf{g}}. \quad (2.24)$$

### Energetic constitutive equation

The Fourier's law is adopted to describe the mechanism of contact heat transfer. Furthermore, isotropic materials are considered. Thus, the heat flux depend linearly on the temperature gradient and the thermal conductivity  $\lambda_k$  of the fluid, which is assumed constant. The heat flux becomes

$$\boxed{\mathbf{q}_k = -\lambda_k \nabla T_k}. \quad (2.25)$$

Heat generation due to nuclear, electric or magnetic effects are absent. In addition, the temperature of the fluids in the problems treated within the present work are relatively low thus radiative heat transfer is negligible. Hence, the constitutive law for the volumetric heat generation rate is

$$\boxed{\dot{q}_k''' = 0}. \quad (2.26)$$

### Equation of state

The assumption of incompressible fluids is made throughout the present work. It is justified by the small enough Mach number  $\text{Ma} = u/u_{\text{sound}}$  within the liquid and gaseous phases. The density  $\rho_k$  of each phase is therefore assumed constant and the continuity equation (Eq. (2.13)) reduces to

$$\boxed{\nabla \cdot \mathbf{u}_k = 0}. \quad (2.27)$$

### 2.1.4 Interfacial jump and boundary conditions

The standard differential balance equations derived previously hold for each fluid sub-region up to an interface, but not across it. The so-called jump conditions are necessary to account for the discontinuities in the various variables at the interface, and thus to impose the proper boundary conditions. Different approaches can be found in literature for their derivation. In Ishii and Hibiki (2006), the balance equations are integrated on a control volume containing a finite thickness interface. While in Delhaye (1974), the interfacial jump conditions are derived from the global balances on a material volume cut by an interface with given properties and mass. Here, an approach similar to Delhaye (1974) is used. However, for the sake of simplicity, an ideal interface is assumed.

#### Ideal interface condition

By setting the entropy production of the interface to zero, there are no resistances to interfacial transfer of quantities (Ishii and Hibiki, 2006). This means that the exchanges between the two phases are governed by the conditions of the bulk fluid at each side, but not by the interface itself. Hence the interface can be considered as ideal and the transfer at the interface can be said reversible.

#### Mass jump condition

The conservation of mass integrated over the material volume  $V(t)$  (see Figure 2.1) gives

$$\frac{d}{dt} \int_{V_1(t)} \rho_1 dV + \frac{d}{dt} \int_{V_2(t)} \rho_2 dV = 0. \quad (2.28)$$

Thus, following Eqs. (2.3) and (2.12), we have

$$\int_{A_{\text{int}}(t)} \rho_1 (\mathbf{u}_1 - \mathbf{u}_{\text{int}}) \cdot \mathbf{n}_1 dA + \int_{A_{\text{int}}(t)} \rho_2 (\mathbf{u}_2 - \mathbf{u}_{\text{int}}) \cdot \mathbf{n}_2 dA = 0, \quad (2.29)$$

which simply states that

$$\boxed{\dot{m}_1'' = -\dot{m}_2'' = \dot{m}''.} \quad (2.30)$$

#### Linear momentum jump condition

In order to integrate the linear momentum over the material volume  $V(t)$ , the forces acting on the interface need to be taken into account in addition to the forces acting on the fluid particles. Introducing the surface tension coefficient  $\sigma(\mathbf{x}_{\text{int}}, t)$ , the conservation of linear momentum reads

$$\begin{aligned} \frac{d}{dt} \int_{V_1(t)} \rho_1 \mathbf{u}_1 dV + \frac{d}{dt} \int_{V_2(t)} \rho_2 \mathbf{u}_2 dV &= \oint_{C_{\text{int}}(t)} \sigma \mathbf{N} dl \\ &+ \int_{A_1(t)} \mathbf{T}_1 \cdot \mathbf{n}_1 dA + \int_{A_2(t)} \mathbf{T}_2 \cdot \mathbf{n}_2 dA + \int_{V_1(t)} \rho_1 \mathbf{b}_1 dV + \int_{V_2(t)} \rho_2 \mathbf{b}_2 dV. \end{aligned} \quad (2.31)$$

The Gauss's theorem for a surface (Aris, 1962; Delhaye, 1974) is given as

$$\oint_{\partial A(t)} F \mathbf{N} dl = \int_{A(t)} [\nabla_s F - (\nabla_s \cdot \mathbf{n}) F \mathbf{n}] dA, \quad (2.32)$$

## Chapter 2. Governing equations

---

where  $F$  is a scalar field defined on the surface  $A(t)$ ,  $\nabla_s$  the surface del operator and  $\mathbf{N}$  the outward-pointing unit normal vector at a given point belonging to the curve  $\partial A(t)$  and located in the tangent plane of  $A(t)$ . By definition we also have the identity

$$\nabla = \nabla_s + \mathbf{n}(\mathbf{n} \cdot \nabla) = \nabla_s + \nabla_n. \quad (2.33)$$

In view of Eqs. (2.3), (2.14), (2.31) and (2.32), the linear momentum jump condition reduces to

$$\mathbf{T}_1 \cdot \mathbf{n}_1 + \mathbf{T}_2 \cdot \mathbf{n}_2 = \dot{m}_1'' \mathbf{u}_1 + \dot{m}_2'' \mathbf{u}_2 + \nabla_s \sigma + \sigma \kappa \mathbf{n}, \quad (2.34)$$

where  $\kappa = -\nabla_s \cdot \mathbf{n}$  is twice the mean curvature and  $\mathbf{n}$  can be chosen arbitrarily equal to  $\mathbf{n}_1$  or  $\mathbf{n}_2$ . Considering  $\mathbf{n} = \mathbf{n}_1 = -\mathbf{n}_2$  and  $\mathbf{T}_k = -p_k \mathbf{I} + \mu_k (\nabla \mathbf{u}_k + \nabla \mathbf{u}_k^\top)$ , the above equations becomes

$$\begin{aligned} & (p_2 - p_1) \mathbf{n} + [\mu_1 (\nabla \mathbf{u}_1 + \nabla \mathbf{u}_1^\top) - \mu_2 (\nabla \mathbf{u}_2 + \nabla \mathbf{u}_2^\top)] \cdot \mathbf{n} = \\ & \dot{m}'' (\mathbf{u}_1 - \mathbf{u}_2) + \nabla_s \sigma + \sigma \kappa \mathbf{n}. \end{aligned} \quad (2.35)$$

Projecting the above jump condition along the normal to the interface and using the identities  $\nabla \mathbf{u} \cdot \mathbf{n} = \nabla u_n$  and  $(\nabla \mathbf{u})^\top \cdot \mathbf{n} = \nabla_n \mathbf{u}$ , the pressure jump is obtained

$$p_2 - p_1 = 2 (\mu_2 \nabla_n u_{2,n} - \mu_1 \nabla_n u_{1,n}) + \dot{m}'' (u_{1,n} - u_{2,n}) + \sigma \kappa, \quad (2.36)$$

where  $u_{k,n}(\mathbf{x}_{\text{int}}, t)$  is the normal component of the velocity of the  $k$ -th phase at the interface. For the tangential directions we have

$$\begin{aligned} & \mu_1 (\nabla_s u_{1,n} + \nabla_n u_{1,s}) - \mu_2 (\nabla_s u_{2,n} + \nabla_n u_{2,s}) = \\ & \dot{m}'' (u_{1,s} - u_{2,s}) + \nabla_s \sigma, \end{aligned} \quad (2.37)$$

which, considering the no-slip interfacial boundary condition  $\mathbf{u}_{1,s} = \mathbf{u}_{2,s}$ , given later in the text, reduces to

$$\mu_1 (\nabla_s u_{1,n} + \nabla_n u_{1,s}) - \mu_2 (\nabla_s u_{2,n} + \nabla_n u_{2,s}) = \nabla_s \sigma. \quad (2.38)$$

### Angular momentum jump condition

The derivation of the angular momentum jump condition leads to the same condition as Eq. (2.35) (Delhaye, 1974).

**Total energy jump condition**

The global balance of the total energy reads

$$\begin{aligned}
 & \frac{d}{dt} \int_{V_1(t)} \rho_1 \left( \frac{u_1^2}{2} + e_1 \right) dV + \frac{d}{dt} \int_{V_2(t)} \rho_2 \left( \frac{u_2^2}{2} + e_2 \right) dV = \\
 & - \int_{A_1(t)} \mathbf{q}_1 \cdot \mathbf{n}_1 dA - \int_{A_2(t)} \mathbf{q}_2 \cdot \mathbf{n}_2 dA \\
 & + \int_{A_1(t)} (\mathbf{T}_1 \cdot \mathbf{u}_1) \cdot \mathbf{n}_1 dA + \int_{A_2(t)} (\mathbf{T}_2 \cdot \mathbf{u}_2) \cdot \mathbf{n}_2 dA \\
 & + \int_{V_1(t)} \rho_1 (\mathbf{b}_1 \cdot \mathbf{u}_1) dV + \int_{V_2(t)} \rho_2 (\mathbf{b}_2 \cdot \mathbf{u}_2) dV \\
 & + \int_{V_1(t)} \dot{q}_1''' dV + \int_{V_2(t)} \dot{q}_2''' dV + \int_{A_1(t)} (\nabla_s \sigma + \sigma \kappa \mathbf{n}) \cdot \mathbf{u}_{\text{int}} dA.
 \end{aligned} \tag{2.39}$$

In view of Eqs. (2.3) and (2.17) the above equation reduces to

$$\begin{aligned}
 & -\mathbf{q}_1 \cdot \mathbf{n}_1 - \mathbf{q}_2 \cdot \mathbf{n}_2 + (\mathbf{T}_1 \cdot \mathbf{u}_1) \cdot \mathbf{n}_1 + (\mathbf{T}_2 \cdot \mathbf{u}_2) \cdot \mathbf{n}_2 \\
 & = \dot{m}_1'' \left( \frac{u_1^2}{2} + e_1 \right) + \dot{m}_2'' \left( \frac{u_2^2}{2} + e_2 \right) + (\nabla_s \sigma + \sigma \kappa \mathbf{n}) \cdot \mathbf{u}_{\text{int}}.
 \end{aligned} \tag{2.40}$$

Considering the energy constitutive equation  $\mathbf{q}_k = -\lambda_k \nabla T_k$ , we have the following jump condition for the heat flux at the interface

$$\begin{aligned}
 & \lambda_1 \nabla_n T_1 - \lambda_2 \nabla_n T_2 = (\mathbf{T}_2 \cdot \mathbf{u}_2) \cdot \mathbf{n} - (\mathbf{T}_1 \cdot \mathbf{u}_1) \cdot \mathbf{n} \\
 & + \dot{m}'' \left( \frac{u_1^2}{2} + e_1 - \frac{u_2^2}{2} - e_2 \right) + (\nabla_s \sigma + \sigma \kappa \mathbf{n}) \cdot \mathbf{u}_{\text{int}}.
 \end{aligned} \tag{2.41}$$

**Mechanical energy jump condition**

Dotting the linear momentum jump condition, Eq. (2.35), by the interface velocity, the mechanical energy jump condition is obtained (Delhaye, 1974)

$$\begin{aligned}
 & (\mathbf{T}_1 \cdot \mathbf{n}_1) \cdot \mathbf{u}_{\text{int}} + (\mathbf{T}_2 \cdot \mathbf{n}_2) \cdot \mathbf{u}_{\text{int}} \\
 & = \dot{m}_1'' \mathbf{u}_1 \cdot \mathbf{u}_{\text{int}} + \dot{m}_2'' \mathbf{u}_2 \cdot \mathbf{u}_{\text{int}} + (\nabla_s \sigma + \sigma \kappa \mathbf{n}) \cdot \mathbf{u}_{\text{int}}.
 \end{aligned} \tag{2.42}$$

**Internal energy jump condition**

Subtracting the mechanical energy jump condition from the total energy jump condition, the internal energy jump condition is obtained

$$\begin{aligned}
 & \lambda_1 \nabla_n T_1 - \lambda_2 \nabla_n T_2 = (\mathbf{T}_2 \cdot \mathbf{n}) \cdot (\mathbf{u}_2 - \mathbf{u}_{\text{int}}) - (\mathbf{T}_1 \cdot \mathbf{n}) \cdot (\mathbf{u}_1 - \mathbf{u}_{\text{int}}) \\
 & + \dot{m}'' \left( \frac{u_1^2}{2} + e_1 - \mathbf{u}_1 \cdot \mathbf{u}_{\text{int}} - \frac{u_2^2}{2} - e_2 + \mathbf{u}_2 \cdot \mathbf{u}_{\text{int}} \right).
 \end{aligned} \tag{2.43}$$

### Enthalpy jump condition

Substituting the internal energy with the enthalpy defined as  $h_k = e_k + p_k/\rho_k$ , the enthalpy jump condition is obtained from the internal energy jump condition

$$\begin{aligned} \lambda_1 \nabla_n T_1 - \lambda_2 \nabla_n T_2 &= (\mathbf{T}_2 \cdot \mathbf{n}) \cdot (\mathbf{u}_2 - \mathbf{u}_{\text{int}}) - (\mathbf{T}_1 \cdot \mathbf{n}) \cdot (\mathbf{u}_1 - \mathbf{u}_{\text{int}}) \\ &+ \dot{m}'' \left( \frac{u_1^2}{2} + h_1 - \frac{p_1}{\rho_1} - \mathbf{u}_1 \cdot \mathbf{u}_{\text{int}} - \frac{u_2^2}{2} - h_2 + \frac{p_2}{\rho_2} + \mathbf{u}_2 \cdot \mathbf{u}_{\text{int}} \right). \end{aligned} \quad (2.44)$$

Replacing the expression of the surface stress tensor by  $\mathbf{T}_k = -p_k \mathbf{I} + \mathbf{S}_k$ , the above equation becomes

$$\begin{aligned} \lambda_1 \nabla_n T_1 - \lambda_2 \nabla_n T_2 &= p_1 (\mathbf{u}_1 - \mathbf{u}_{\text{int}}) \cdot \mathbf{n} - p_2 (\mathbf{u}_2 - \mathbf{u}_{\text{int}}) \cdot \mathbf{n} \\ &+ (\mathbf{S}_2 \cdot \mathbf{n}) \cdot (\mathbf{u}_2 - \mathbf{u}_{\text{int}}) - (\mathbf{S}_1 \cdot \mathbf{n}) \cdot (\mathbf{u}_1 - \mathbf{u}_{\text{int}}) \\ &+ \dot{m}'' \left( \frac{u_1^2}{2} + h_1 - \frac{p_1}{\rho_1} - \mathbf{u}_1 \cdot \mathbf{u}_{\text{int}} - \frac{u_2^2}{2} - h_2 + \frac{p_2}{\rho_2} + \mathbf{u}_2 \cdot \mathbf{u}_{\text{int}} \right), \end{aligned} \quad (2.45)$$

which, using the expression of the mass transfer flux, simplifies to

$$\begin{aligned} \lambda_1 \nabla_n T_1 - \lambda_2 \nabla_n T_2 &= (\mathbf{S}_2 \cdot \mathbf{n}) \cdot (\mathbf{u}_2 - \mathbf{u}_{\text{int}}) - (\mathbf{S}_1 \cdot \mathbf{n}) \cdot (\mathbf{u}_1 - \mathbf{u}_{\text{int}}) \\ &+ \dot{m}'' \left( \frac{u_1^2}{2} + h_1 - \mathbf{u}_1 \cdot \mathbf{u}_{\text{int}} - \frac{u_2^2}{2} - h_2 + \mathbf{u}_2 \cdot \mathbf{u}_{\text{int}} \right). \end{aligned} \quad (2.46)$$

In most cases, the viscous dissipation and kinetic energy are negligible with respect to the heat flux and enthalpy. Hence, the enthalpy jump can be expressed as

$$\boxed{\dot{m}'' (h_2 - h_1) = \lambda_2 \nabla_n T_2 - \lambda_1 \nabla_n T_1.} \quad (2.47)$$

### Thermal boundary condition

Since the interface is ideal, the thermal boundary condition can be derived from the interfacial entropy inequality (Ishii and Hibiki, 2006). This gives

$$\boxed{T_1 = T_2 = T_{\text{int}},} \quad (2.48)$$

which states that the interface is in thermal equilibrium. The reader is referred to Ishii and Hibiki (2006) for an introduction to the cases in which the above condition is not valid.

### No-slip condition

From the above equations, the tangential velocity  $\mathbf{u}_{s,\text{int}}$  is an unknown parameter. In the present thesis, the interface is considered ideal, thus from the interfacial entropy inequality (Ishii and Hibiki, 2006), a no-slip condition is obtained

$$\boxed{\mathbf{u}_{1,s} = \mathbf{u}_{2,s} = \mathbf{u}_{\text{int},s},} \quad (2.49)$$

which is valid for viscous fluids.

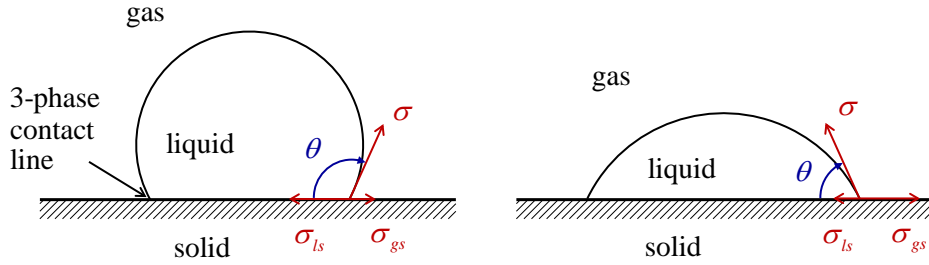


**Figure 2.2:** Contact angle  $\theta$  in function of the surface tension between gas-liquid  $\sigma$ , gas-solid  $\sigma_{gs}$ , and liquid-solid  $\sigma_{ls}$ .

### Contact angle

The singularity created by the intersection of two different interfaces, also referred as the 3-phase contact line, adds an additional boundary condition to the problem. In the case of a two-phase flow, the third phase is the solid bounding the flow domain. As a bubble or a droplet approaches the solid boundary, the gas-liquid interface attaches the wall forming a singular curve at the intersection. Depending on the forces acting on the singular curve, a given contact angle  $\theta$ , measured through the liquid, is observed (see Figure 2.2). Considering only the surface fluxes, the force balance in the normal plane to the singular curve gives (Ishii and Hibiki, 2006)

$$\cos\theta = \frac{\sigma_{gs} - \sigma_{ls}}{\sigma}, \quad (2.50)$$

where  $\sigma$  is the gas-liquid surface tension,  $\sigma_{gs}$  the gas-solid surface tension, and  $\sigma_{ls}$  the liquid-solid surface tension. In practice, only the surface tension between gas and liquid is known and the contact angle is measured experimentally for a given set of gas-liquid-solid phases. In addition, the surface roughness and chemical heterogeneity of the surface can influence the apparent contact angle at the 3-phase contact line. In modeling and measuring the contact angle, static conditions are often considered. However, the contact angle is dynamic while the interface is moving and the dynamic values of contact angle can differ significantly from the static ones. In the present thesis, static apparent contact angles are considered.

## 2.2 One-fluid formulation

In order to reduce the computational time associated with the solution of the conservation laws, the one-fluid formulation can be used. In this case a Heaviside function  $\chi(\mathbf{x}, t)$  is introduced and allows to solve only one set of conservation laws for both the phases. Early works employing such formulation can be attributed to Hirt and Nichols (1981), Unverdi and Tryggvason (1992) and Sussman et al. (1994). It is particularly suited for modeling two-phase flow at the spatial scale of the interface shape.

The Heaviside function is defined arbitrarily as

$$\chi(\mathbf{x}, t) \equiv \begin{cases} 1 & \text{if the point } \mathbf{x} \text{ pertains to phase 1,} \\ 0 & \text{if the point } \mathbf{x} \text{ pertains to phase 2.} \end{cases} \quad (2.51)$$

## Chapter 2. Governing equations

---

The density, dynamic viscosity and thermal conductivity are then defined as

$$\rho = \chi\rho_1 + (1 - \chi)\rho_2, \quad (2.52)$$

$$\mu = \chi\mu_1 + (1 - \chi)\mu_2, \quad (2.53)$$

$$\lambda = \chi\lambda_1 + (1 - \chi)\lambda_2. \quad (2.54)$$

All other quantities are now defined using only one variable for each phase, e.g.  $\mathbf{u} = \mathbf{u}_1$  within  $V_1(t)$  and  $\mathbf{u} = \mathbf{u}_2$  within  $V_2(t)$ . In the derivation of the conservation laws, the constitutive equations as well as the jump and boundary conditions introduced previously will be taken into account.

### 2.2.1 Conservation of mass

The time derivative of the newly defined density field reads

$$\frac{d}{dt} \int_{V(t)} \rho dV = \frac{d}{dt} \int_{V(t)} \chi\rho_1 dV + \frac{d}{dt} \int_{V(t)} (1 - \chi) \rho_2 dV, \quad (2.55)$$

which is equivalent to

$$\frac{d}{dt} \int_{V(t)} \rho dV = \frac{d}{dt} \int_{V_1(t)} \rho_1 dV + \frac{d}{dt} \int_{V_2(t)} \rho_2 dV. \quad (2.56)$$

This results simply in the conservation of mass for the material volume

$$\frac{d}{dt} \int_{V(t)} \rho dV = 0, \quad (2.57)$$

which, using the Reynolds' transport theorem Eq. (2.5), gives the following the differential form

$$\frac{\partial \rho}{\partial t} + \nabla \cdot (\rho \mathbf{u}) = 0.$$

(2.58)

Considering the incompressibility condition, it is possible to obtain the condition for the divergence of the one-fluid velocity field. Using the Gauss's theorem Eq. (2.6), we have

$$\int_{V(t)} \nabla \cdot \mathbf{u} dV = \int_{A_1(t)} \mathbf{u} \cdot \mathbf{n} dA + \int_{A_2(t)} \mathbf{u} \cdot \mathbf{n} dA. \quad (2.59)$$

Summing the incompressibility condition applied to each phase (Eq. (2.27)) gives

$$\int_{V_1(t)} \nabla \cdot \mathbf{u}_1 dV + \int_{V_2(t)} \nabla \cdot \mathbf{u}_2 dV = 0, \quad (2.60)$$

which, using the Gauss's theorem Eq. (2.6) gives

$$\int_{A_1(t)} \mathbf{u}_1 \cdot \mathbf{n} dA + \int_{A_{\text{int}}(t)} \mathbf{u}_1 \cdot \mathbf{n} dA + \int_{A_2(t)} \mathbf{u}_2 \cdot \mathbf{n} dA - \int_{A_{\text{int}}(t)} \mathbf{u}_2 \cdot \mathbf{n} dA = 0. \quad (2.61)$$

## 2.2. One-fluid formulation

---

On the boundary of the material volume, surfaces  $A_1(t)$  and  $A_2(t)$ , the one-fluid velocity  $\mathbf{u}$  is equal to  $\mathbf{u}_1$  and  $\mathbf{u}_2$  respectively. At the interface, the jump condition need to be taken into account. Using the definition of the mass transfer flux Eq. (2.2) we have

$$\mathbf{u}_2 \cdot \mathbf{n} - \mathbf{u}_1 \cdot \mathbf{n} = \left( \frac{1}{\rho_2} - \frac{1}{\rho_1} \right) \dot{m}''.$$
 (2.62)

Hence, the incompressibility condition now reads

$$\int_{V(t)} \nabla \cdot \mathbf{u} dV = \int_{A_{\text{int}}(t)} \left( \frac{1}{\rho_2} - \frac{1}{\rho_1} \right) \dot{m}'' dA,$$
 (2.63)

which gives the following differential form

$$\nabla \cdot \mathbf{u} = \left( \frac{1}{\rho_2} - \frac{1}{\rho_1} \right) \dot{m}'' \delta_{\text{int}},$$

 (2.64)

where the Dirac delta function  $\delta_{\text{int}} \sim A_{\text{int}}/V$  states the fact that the divergence is non-null only at the interface

### 2.2.2 Conservation of linear momentum

The time derivative of the newly defined momentum reads

$$\frac{d}{dt} \int_{V(t)} \rho \mathbf{u} dV = \frac{d}{dt} \int_{V(t)} \chi \rho_1 \mathbf{u} dV + \frac{d}{dt} \int_{V(t)} (1 - \chi) \rho_2 \mathbf{u} dV,$$
 (2.65)

which is equivalent to

$$\frac{d}{dt} \int_{V(t)} \rho \mathbf{u} dV = \frac{d}{dt} \int_{V_1(t)} \rho_1 \mathbf{u} dV + \frac{d}{dt} \int_{V_2(t)} \rho_2 \mathbf{u} dV.$$
 (2.66)

Since the one-fluid velocity  $\mathbf{u}$  is equal to  $\mathbf{u}_1$  and  $\mathbf{u}_2$  within  $V_1(t)$  and  $V_2(t)$  respectively, Eq. (2.31) can be used to express the right-hand-side of the above equation. This gives

$$\begin{aligned} \frac{d}{dt} \int_{V(t)} \rho \mathbf{u} dV &= \oint_{C_{\text{int}}(t)} \sigma \mathbf{N} dl \\ &+ \int_{A_1(t)} \mathbf{T}_1 \cdot \mathbf{n}_1 dA + \int_{A_2(t)} \mathbf{T}_2 \cdot \mathbf{n}_2 dA + \int_{V_1(t)} \rho_1 \mathbf{b}_1 dV + \int_{V_2(t)} \rho_2 \mathbf{b}_2 dV. \end{aligned}$$
 (2.67)

Using the Gauss's theorem for a surface Eq. (2.32) and the constitutive equations Eqs. (2.23) and (2.24), the above equation becomes

$$\begin{aligned} \frac{d}{dt} \int_{V(t)} \rho \mathbf{u} dV &= - \int_{A_1(t)} p_1 \mathbf{n} dA - \int_{A_2(t)} p_2 \mathbf{n} dA \\ &+ \int_{A_1(t)} \mu_1 (\nabla \mathbf{u}_1 + \nabla \mathbf{u}_1^\top) \cdot \mathbf{n} dA + \int_{A_2(t)} \mu_2 (\nabla \mathbf{u}_2 + \nabla \mathbf{u}_2^\top) \cdot \mathbf{n} dA \\ &+ \int_{V_1(t)} \rho_1 \mathbf{g} dV + \int_{V_2(t)} \rho_2 \mathbf{g} dV + \int_{A_{\text{int}}(t)} (\nabla_s \sigma + \sigma \kappa \mathbf{n}) dA, \end{aligned}$$
 (2.68)

## Chapter 2. Governing equations

---

which, using the one-fluid quantities and the Heaviside function, gives

$$\begin{aligned} \frac{d}{dt} \int_{V(t)} \rho \mathbf{u} dV &= - \oint_{\partial V(t)} p \mathbf{n} dA + \int_{\partial V(t)} \chi \mu_1 (\nabla \mathbf{u} + \nabla \mathbf{u}^\top) \cdot \mathbf{n} dA \\ &+ \int_{\partial V(t)} (1 - \chi) \mu_2 (\nabla \mathbf{u} + \nabla \mathbf{u}^\top) \cdot \mathbf{n} dA \\ &+ \int_{V(t)} \chi \rho_1 \mathbf{g} dV + \int_{V(t)} (1 - \chi) \rho_2 \mathbf{g} dV + \int_{A_{\text{int}}(t)} (\nabla_s \sigma + \sigma \kappa \mathbf{n}) dA. \end{aligned} \quad (2.69)$$

The conservation of linear momentum thus reads

$$\begin{aligned} \frac{d}{dt} \int_{V(t)} \rho \mathbf{u} dV &= - \oint_{\partial V(t)} p \mathbf{n} dA + \oint_{\partial V(t)} \mu (\nabla \mathbf{u} + \nabla \mathbf{u}^\top) \cdot \mathbf{n} dA \\ &+ \int_{V(t)} \rho \mathbf{g} dV + \int_{A_{\text{int}}(t)} (\nabla_s \sigma + \sigma \kappa \mathbf{n}) dA, \end{aligned} \quad (2.70)$$

which in differential form becomes

$$\begin{aligned} \frac{\partial \rho \mathbf{u}}{\partial t} + \nabla \cdot (\rho \mathbf{u} \mathbf{u}) \\ = -\nabla p + \nabla \cdot [\mu (\nabla \mathbf{u} + \nabla \mathbf{u}^\top)] + \rho \mathbf{g} + (\nabla_s \sigma + \sigma \kappa \mathbf{n}) \delta_{\text{int}}. \end{aligned} \quad (2.71)$$

### 2.2.3 Enthalpy equation

In the cases studied in the present thesis, it is preferable to solve the enthalpy equation rather than the total energy equation. In particular, we are interested mainly in the temperature field, thus the transport equation for temperature is derived from the enthalpy equation, using the fact that the fluids are incompressible and that temperature changes are relatively small, so that the specific heat capacities can be considered constant.

Neglecting the pressure work, the viscous dissipation and the heat generation, the enthalpy equation for each phase Eq. (2.21) integrated over the sub-volume  $V_k(t)$  pertaining to each phase becomes

$$\int_{V_k(t)} \frac{\partial \rho_k h_k}{\partial t} dV + \oint_{\partial V_k(t)} \rho_k h_k \mathbf{u}_k \cdot \mathbf{n} dA = \oint_{\partial V_k(t)} \lambda_k \nabla T_k \cdot \mathbf{n} dA. \quad (2.72)$$

Summing the above equation for each phase gives

$$\begin{aligned} &\int_{V_1(t)} \frac{\partial \rho_1 h_1}{\partial t} dV + \int_{A_1(t)} \rho_1 h_1 \mathbf{u}_1 \cdot \mathbf{n} dA + \int_{A_{\text{int}}(t)} \rho_1 h_1 \mathbf{u}_{\text{int}} \cdot \mathbf{n} dA \\ &+ \int_{V_2(t)} \frac{\partial \rho_2 h_2}{\partial t} dV + \int_{A_2(t)} \rho_2 h_2 \mathbf{u}_2 \cdot \mathbf{n} dA - \int_{A_{\text{int}}(t)} \rho_2 h_2 \mathbf{u}_{\text{int}} \cdot \mathbf{n} dA \\ &= \int_{A_1(t)} \lambda_1 \nabla T_1 \cdot \mathbf{n} dA + \int_{A_{\text{int}}(t)} \lambda_1 \nabla T_1 \cdot \mathbf{n} dA \\ &+ \int_{A_2(t)} \lambda_2 \nabla T_2 \cdot \mathbf{n} dA - \int_{A_{\text{int}}(t)} \lambda_2 \nabla T_2 \cdot \mathbf{n} dA \\ &- \int_{A_{\text{int}}(t)} \rho_1 h_1 (\mathbf{u}_1 - \mathbf{u}_{\text{int}}) \cdot \mathbf{n} dA + \int_{A_{\text{int}}(t)} \rho_2 h_2 (\mathbf{u}_2 - \mathbf{u}_{\text{int}}) \cdot \mathbf{n} dA, \end{aligned} \quad (2.73)$$

which, using the Reynolds transport theorem Eq. (2.5) and the enthalpy jump condition Eq. (2.47), reduces to

$$\begin{aligned} & \frac{d}{dt} \int_{V_1(t)} \rho_1 h_1 dV + \frac{d}{dt} \int_{V_2(t)} \rho_2 h_2 dV \\ &= \int_{A_1(t)} \lambda_1 \nabla T_1 \cdot \mathbf{n} dA + \int_{A_2(t)} \lambda_2 \nabla T_2 \cdot \mathbf{n} dA \\ & - \int_{A_{\text{int}}(t)} \dot{m}'' (h_2 - h_1) dA + \int_{A_{\text{int}}(t)} \dot{m}'' (h_2 - h_1) dA. \end{aligned} \quad (2.74)$$

The fluids are incompressible, thus their specific heat capacities are function of temperature only, i.e.  $c_k = c_k(T)$ . In the present thesis, the temperature changes are relatively small thus variation of specific heat capacities with temperature can be neglected. As a consequence, the specific enthalpy of each phase is a linear function of temperature. Considering the reference enthalpy of each phase  $h_{k,0}$  taken at some temperature  $T_0$  at the same phase state, we have the following relation for the specific enthalpy

$$h_k = h_{k,0} + c_k (T_k - T_0), \quad (2.75)$$

where  $c_k$  is taken as the specific heat capacity at constant pressure. Substituting the above equation into Eq. (2.74) gives

$$\begin{aligned} & \frac{d}{dt} \int_{V_1(t)} \rho_1 c_1 T_1 dV + \frac{d}{dt} \int_{V_2(t)} \rho_2 c_2 T_2 dV \\ & + (h_{1,0} - c_1 T_0) \frac{d}{dt} \int_{V_1(t)} \rho_1 dV + (h_{2,0} - c_2 T_0) \frac{d}{dt} \int_{V_2(t)} \rho_2 dV \\ &= \int_{A_1(t)} \lambda_1 \nabla T_1 \cdot \mathbf{n} dA + \int_{A_2(t)} \lambda_2 \nabla T_2 \cdot \mathbf{n} dA, \end{aligned} \quad (2.76)$$

which, using the conservation of mass for each phase (Eq. (2.3) together with (2.12)), reduces to

$$\begin{aligned} & \frac{d}{dt} \int_{V_1(t)} \rho_1 c_1 T_1 dV + \frac{d}{dt} \int_{V_2(t)} \rho_2 c_2 T_2 dV \\ &= \int_{A_1(t)} \lambda_1 \nabla T_1 \cdot \mathbf{n} dA + \int_{A_2(t)} \lambda_2 \nabla T_2 \cdot \mathbf{n} dA \\ & - \int_{A_{\text{int}}(t)} \dot{m}'' (h_{2,0} - h_{1,0} - (c_2 - c_1) T_0) dA. \end{aligned} \quad (2.77)$$

## Chapter 2. Governing equations

---

Introducing the Heaviside function, the transport equation for the one-fluid temperature is obtained

$$\int_{V(t)} \frac{\partial \hat{\rho}cT}{\partial t} dV + \oint_{\partial V(t)} \hat{\rho}cT \mathbf{u} \cdot \mathbf{n} dA = \oint_{\partial V(t)} \lambda \nabla T \cdot \mathbf{n} dA \\ - \int_{A_{\text{int}}(t)} \dot{m}'' [h_{21} - (c_2 - c_1) T_0] dA, \quad (2.78)$$

where  $\hat{\rho}c = \chi \rho_1 c_1 + (1 - \chi) \rho_2 c_2$  and  $h_{21} = h_{2,0} - h_{1,0}$ . In differential form, we have

$$\frac{\partial \hat{\rho}cT}{\partial t} + \nabla \cdot (\hat{\rho}cT \mathbf{u}) = \nabla \cdot (\lambda \nabla T) - \dot{m}'' [h_{21} - (c_2 - c_1) T_0] \delta_{\text{int}}. \quad (2.79)$$

Note that the above equation is similar to the equation given in Esmaeeli and Tryggvason (2004a).

---

# CHAPTER 3

---

## Implemented numerical method

---

In this chapter, the numerical method used to solve the governing equations of a two-phase flow with heat and mass transfer are described. The method is implemented using the OpenFOAM (OpenFOAM Foundation, 2013) CFD toolbox version 2.2.x (repository version), thus most of the algorithms and schemes will refer to the documentation of OpenFOAM. The framework used to discretize the governing equations will be first introduced, followed by the description of the interface tracking technique and the interfacial curvature calculation methods adopted in the present thesis. Then the treatment of the various interfacial jumps due to heat and mass transfer will be described. Finally, the algorithm used to couple the pressure and velocity fields and the special treatment of the body forces will be detailed followed by the final solution procedure adopted.

---

### 3.1 Finite volume discretization

---

A standard Finite Volume method (FVM) is used to reduce the governing equations of the problem into a system of linear algebraic equations. The solution of this system is obtained using proper algorithms and linear solvers. It provides estimates of the solution of the governing equations at given locations and instants, determined by the discretization of the spatial and temporal domains. The method can be describe through the following steps:

- Discretization of the computational domain;
- Formulation of the discretized governing equations;
- Solution of the system of linear algebraic equation.

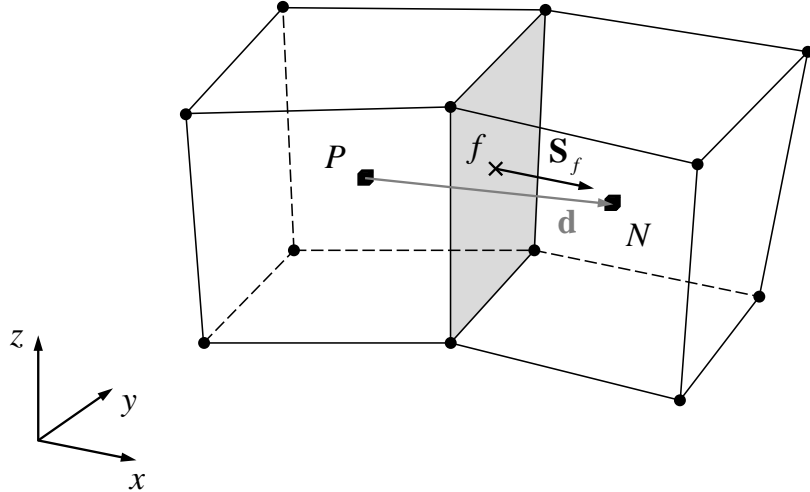


**Figure 3.1:** Typical control volume. The cube symbol ■ denotes the cell center, the cross × the face center and the spheres • the points defining the cell and its faces.

### 3.1.1 Discretization of the computational domain

In the case of transient problems, the discretization of the temporal domain is obtained by prescribing a given number of time-steps to accomplish the desired physical time. The size of the time-step is usually given as a constant, though a variable time-step size may be prescribed in order to meet the stability criteria imposed by some numerical schemes.

The discretization of the spatial domain into control volumes forms the so-called computational mesh. In the general case, convex polyhedra control volumes are considered and fill the spatial domain without overlapping. However, it is more common to use tetrahedra or hexahedra control volumes, or a mix of them with pyramids and prisms control volumes. In the latter case, the computational mesh is often referred to as hybrid. Since a computational cell can have a variable number of neighbors, the data structure adopted is unstructured. In addition, a collocated variable arrangement is considered, in which all dependent variables share the same control volumes (Rhee and Chow, 1983).

A typical hexahedral control volume with one of its neighbor are represented in Figure 3.1. The point  $P$  is the centroid of the control volume  $V_P$  and the point  $N$  is the centroid of the neighboring control volume  $V_N$  sharing one of the faces of  $V_P$ . Two groups of faces are identifiable within the computational mesh: internal faces connecting two control volumes (denoted as owner, with symbol  $P$ , and neighbor, with symbol  $N$ ) and boundary faces connected only to one control volume (denoted as owner, with symbol  $P$ ). The vector  $\mathbf{S}_f = S_f \mathbf{n}_f$  is the surface area vector of the face connecting  $V_P$  and  $V_N$  and oriented toward the neighbor. In the case of a boundary face, the face unit normal vector  $\mathbf{n}_f$  is oriented outward the spatial domain. Finally, the geometrical properties of the control volumes and faces are fully determined by the position of the mesh points.

In the present thesis, non-moving computational mesh are used. In order to improve the accuracy of the results without increasing significantly the computational cost, static

### 3.1. Finite volume discretization

---

**Table 3.1:** Value of  $\rho_\psi$ ,  $\psi$ ,  $\Gamma_\psi$  and  $\Phi_\psi$  for the various governing equations.

Governing equation	$\rho_\psi$	$\psi$	$\Gamma_\psi$	$\Phi_\psi$
Conservation of mass	$\rho$	1	0	0
Conservation of linear momentum	$\rho$	$\mathbf{u}$	$\mu$	$-\nabla p + \mu \nabla \cdot \nabla \mathbf{u}^\top + \rho g + (\nabla_s \sigma + \sigma \kappa \mathbf{n}) \delta_{\text{int}}$
Equation of internal energy	$\hat{\rho c}$	$T$	$\lambda$	$-\dot{m}'' [h_{21} - (c_2 - c_1) T_{\text{int}}] \delta_{\text{int}}$

or dynamic local mesh refinement is used for some of the cases studied. Local mesh refinement consists in the decomposition of a control volume into smaller elements. In the case of hexahedral control volumes, eight hexahedra are obtained using the edges' midpoint. This capability, allowed by the arbitrary shape of the control volume and the collocated variable arrangement, is particularly suited to three-dimensional simulations, where the computational cost drastically increases when global mesh refinement is applied.

#### 3.1.2 Formulation of the discretized governing equations

In the previous chapter the governing equations for a two-phase flow with heat and mass transfer have been derived. It is possible to express them in term of a general transport equation for a quantity  $\psi$ , consisting of a transient, a convection, a diffusion and a source term. The differential form of the general transport equation reads

$$\frac{\partial \rho_\psi \psi}{\partial t} + \nabla \cdot (\rho_\psi \psi \mathbf{u}) - \nabla \cdot (\Gamma_\psi \nabla \psi) = \Phi_\psi, \quad (3.1)$$

where  $\Gamma_\psi$  is the diffusion coefficient and  $\Phi_\psi$  the source term for the quantity  $\psi$ . The value of  $\rho_\psi$  also depends on the the quantity considered and is given in Table 3.1 together with the other parameters. The term  $\mu \nabla \cdot \nabla \mathbf{u}^\top$  is given as a source term because it will receive a different treatment with respect to the diffusion term.

The integration of the general transport equation over the control volume  $V_P$  and the time-step  $\Delta t$  gives

$$\begin{aligned} & \int_t^{t+\Delta t} \left[ \int_{V_P} \frac{\partial \rho_\psi \psi}{\partial t} dV + \int_{V_P} \nabla \cdot (\rho_\psi \psi \mathbf{u}) dV - \int_{V_P} \nabla \cdot (\Gamma_\psi \nabla \psi) dV \right] dt \\ &= \int_t^{t+\Delta t} \left( \int_{V_P} \Phi_\psi dV \right) dt. \end{aligned} \quad (3.2)$$

A brief description of the discretization of each terms is given in the following. For a detailed description, the reader is referred to Jasak (1996).

#### Identities

Considering a linear variation of  $\psi$  within the control volume, the following identi-

### Chapter 3. Implemented numerical method

---

ties are obtained for the volume integral and the cell faces integral

$$\int_{V_P} \psi(\mathbf{x}) dV = \psi_P V_P, \quad (3.3)$$

$$\int_f \mathbf{F} \cdot \mathbf{n}_f dA = \mathbf{F}_f \cdot \mathbf{S}_f, \quad (3.4)$$

$$\int_f \mathbf{F} \mathbf{n}_f dA = \mathbf{F}_f \mathbf{S}_f, \quad (3.5)$$

$$\int_f \psi \mathbf{n}_f dA = \psi_f \mathbf{S}_f, \quad (3.6)$$

where  $\mathbf{F}$  is a given vector. The subscripts  $P$  and  $f$  denote the value at the centroid of the control volume and at the face center, respectively.

Using the above relations and the Gauss's theorem gives the following relations between the volume and surface integrals

$$\int_{V_P} \nabla \cdot \mathbf{F} dV = \sum_f \mathbf{F}_f \cdot \mathbf{S}_f, \quad (3.7)$$

$$\int_{V_P} \nabla \mathbf{F} dV = \sum_f \mathbf{F}_f \mathbf{S}_f, \quad (3.8)$$

$$\int_{V_P} \nabla \psi dV = \sum_f \psi_f \mathbf{S}_f. \quad (3.9)$$

Since the unit normal vector  $\mathbf{n}_f$  is oriented outward the owner control volume of the face, it is necessary to split the summation over the cell faces into two sums to account for the change in sign:

$$\sum_f \mathbf{a}_f \cdot \mathbf{S}_f = \sum_{\text{owner}} \mathbf{a}_f \cdot \mathbf{S}_f - \sum_{\text{neighbor}} \mathbf{a}_f \cdot \mathbf{S}_f, \quad (3.10)$$

where the vector  $\mathbf{a}_f$  is either equal to  $\mathbf{F}_f$ ,  $\mathbf{F}_f \mathbf{I}$  or  $\psi_f \mathbf{I}$ .

#### Face interpolation

A collocated variable arrangement is used in the present thesis. In the above identities, values at the cell faces appear and need to be calculated from the estimates at the cell center. If not otherwise specified, the value at the cell faces are linearly interpolated from the cell center values according to

$$\mathbf{a}_f = \alpha_x \mathbf{a}_P + (1 - \alpha_x) \mathbf{a}_N, \quad (3.11)$$

where the interpolation factor  $\alpha_x$  is defined as the ratio of the distances  $\overline{fN}$  and  $\overline{PN}$

$$\alpha_x = \frac{\overline{fN}}{\overline{PN}}, \quad (3.12)$$

where  $f$  is the face center. Such interpolation is second order accurate and is also referred to as Central Differencing (CD).

### Convection term

Following the introduced identities, the discretization of the convection term reads

$$\int_{V_P} \nabla \cdot (\rho_\psi \psi \mathbf{u}) dV = \sum_f (\rho_\psi)_f \phi_f \psi_f, \quad (3.13)$$

where  $\phi_f = \mathbf{u}_f \cdot \mathbf{S}_f$  is the face velocity flux. The calculation of the face velocity flux will be discussed in Section 3.5. The value of  $\psi_f$  can be obtained using the CD scheme introduced previously. However, this can cause unphysical oscillations in convection-dominated flows, violating the boundedness of the solution.

The boundedness of the solution can be guaranteed using the so-called Upwind Differencing (UD) discretization scheme, in which the value of  $\psi_f$  is determined according to the direction of the flow:

$$\psi_f = \begin{cases} \psi_P & \text{for } \phi_f \geq 0, \\ \psi_N & \text{for } \phi_f < 0. \end{cases} \quad (3.14)$$

Though the UD scheme insures boundedness of the solution, a numerical diffusion term is implicitly introduced and the solution obtained can thus be severely influenced. In addition, it has only first order accuracy.

In order to provide bounded and accurate solutions, several differencing schemes were developed. Some of the most common ones are based on the blending between a high order scheme and the UD scheme, with a blending factor which depends on the gradient of the interpolated variable. The blending factor is also referred to as the flux limiter. The value of the flux limiter is obtained considering the Total Variation Diminishing (TVD) condition (van Leer, 1974; Sweby, 1984). Using the CD scheme as the high order scheme, the face interpolation of  $\psi$  gives

$$\psi_f = \psi_{UD} + \Theta(r) (\psi_{CD} - \psi_{UD}), \quad (3.15)$$

where  $\Theta(r)$  is the flux limiter, which depends on the ratio of the consecutive gradients of  $\psi$

$$r = \frac{\psi_C - \psi_U}{\psi_D - \psi_C}. \quad (3.16)$$

The points  $U$ ,  $C$  and  $D$  are chosen according to the direction of the flow on the face  $f$ .

Some other schemes, such as the gamma differencing scheme introduced in Jasak (1996), are based on the Normalized Variable Diagram (NVD). The advantage of these schemes is to allow a bounded solution also when the time-step is high. They are therefore particularly suitable for steady-state problems.

If not otherwise specified, the convection differencing scheme used in the present thesis is a TVD scheme using the van Leer limiter (van Leer, 1974).

### Diffusion term

Using the identities given previously, the discretized form of the diffusion term is obtained and follows

$$\int_{V_P} \nabla \cdot (\Gamma_\psi \nabla \psi) dV = \sum_f (\Gamma_\psi)_f (\nabla \psi)_f \cdot \mathbf{n}_f S_f. \quad (3.17)$$

As noticed in Jasak (1996), if the mesh is orthogonal, i.e. vectors  $\mathbf{d}$  and  $\mathbf{S}_f$  in Figure 3.1 are parallel, it is possible to express the face normal gradient of  $\psi$  as

$$(\nabla \psi)_f \cdot \mathbf{n}_f = \frac{\psi_N - \psi_P}{|\mathbf{d}|}, \quad (3.18)$$

where the two values of  $\psi$  around the face are used. An alternative is to linearly interpolate the cell-centered gradient of the two cells sharing the face

$$(\nabla \psi)_f = \alpha_x (\nabla \psi)_P + (1 - \alpha_x) (\nabla \psi)_N, \quad (3.19)$$

with the cell-centered gradient computed as

$$(\nabla \psi)_P = \frac{1}{V_P} \sum_f \psi_f \mathbf{S}_f. \quad (3.20)$$

Both types of estimate of  $(\nabla \psi)_f \cdot \mathbf{n}_f$  are second order accurate. However, Eq. (3.18) has a smaller truncation error because a more compact stencil is used. Though it may suffer from non-orthogonality, Eq. (3.18) is therefore preferred in the computation of the diffusion term.

In order to deal with the problem of mesh non-orthogonality, the face normal gradient is split into an orthogonal contribution and a non-orthogonal correction as follows

$$(\nabla \psi)_f \cdot \mathbf{n}_f = \underbrace{|\Delta| \frac{\psi_N - \psi_P}{|\mathbf{d}|}}_{\text{orthogonal contribution}} + \underbrace{(\mathbf{n}_f - \Delta) \cdot (\nabla \psi)_f}_{\text{non-orthogonal correction}}, \quad (3.21)$$

where  $\Delta = \mathbf{d}/(\mathbf{d} \cdot \mathbf{n}_f)$  and  $(\nabla \psi)_f$  is computed from Eqs. (3.19) and (3.20).

The term  $\nabla \cdot (\mu \nabla \mathbf{u}^\top)$  in the linear momentum conservation equation is not computed using the above equation. Instead, a cell-centered estimate is calculated for  $\nabla \mathbf{u}^\top$  and is then interpolated to the face in a similar manner as in Eqs. (3.19) and (3.20).

### Source terms

The source terms other than  $\nabla \cdot (\mu \nabla \mathbf{u}^\top)$  are not function of  $\psi$ . However, a source term may depend on  $\psi$  in a general case. In such conditions, the source term is linearized as follows

$$\Phi_\psi(\psi) = \Phi_u + \Phi_p \psi, \quad (3.22)$$

where the first term represent the explicit part of the source term and the last term the implicit contribution. Note that  $\Phi_u$  and  $\Phi_p$  may also depends on  $\psi$ .

### 3.1. Finite volume discretization

---

The discretization of the source term reads

$$\int_{V_P} \Phi_\psi(\psi) dV = \Phi_u V_P + \Phi_p \psi_P V_P. \quad (3.23)$$

#### Temporal discretization

Using the introduced spatial discretization of the various terms, the semi-discretized form of the transport equation is obtained

$$\begin{aligned} & \int_t^{t+\Delta t} \left[ \left( \frac{\partial \rho_\psi \psi}{\partial t} \right)_P V_P + \sum_f (\rho_\psi)_f \phi_f \psi_f - \sum_f (\Gamma_\psi)_f (\nabla \psi)_f \cdot \mathbf{n}_f S_f \right] dt \\ &= \int_t^{t+\Delta t} (\Phi_u V_P + \Phi_p \psi_P V_P) dt. \end{aligned} \quad (3.24)$$

Considering a linear temporal variation of  $\psi$ , the time derivative can be calculated as

$$\left( \frac{\partial \rho_\psi \psi}{\partial t} \right)_P = \frac{(\rho_\psi)_P^n \psi_P^n - (\rho_\psi)_P^o \psi_P^o}{\Delta t}, \quad (3.25)$$

where

$$\psi^n = \psi(t + \Delta t), \quad (3.26)$$

$$\psi^o = \psi(t). \quad (3.27)$$

The temporal integrals of the convection, diffusion and source terms depend on the temporal discretization scheme adopted. The Euler Explicit discretization scheme consider the temporal integral of  $\psi$  as

$$\int_t^{t+\Delta t} \psi(t) dt = \psi^o \Delta t. \quad (3.28)$$

Assuming  $\rho_\psi$ ,  $\Gamma_\psi$ ,  $\Phi_u$  and  $\Phi_p$  constant during the time-step, the following expressions are obtained

$$\psi_f = \alpha_x \psi_P^o + (1 - \alpha_x) \psi_N^o, \quad (3.29)$$

$$(\nabla \psi)_f \cdot \mathbf{n}_f = |\Delta| \frac{\psi_N^o - \psi_P^o}{|d|} + (\mathbf{n}_f - \Delta) \cdot (\nabla \psi)_f^o, \quad (3.30)$$

which can be used to formulate the temporal integral of the convection, diffusion and implicit source terms. The drawback of the explicit scheme is its conditional stability and its first order accuracy. For the stability of the convection term, the Courant-Friedrichs-Lowy (CFL) number should be inferior to unity (Courant et al., 1928). The CFL number is defined as

$$\text{CFL} = \frac{\mathbf{u}_f \cdot \mathbf{n}_f \Delta t}{|d|}. \quad (3.31)$$

### Chapter 3. Implemented numerical method

---

While for the diffusion term, the stability condition requires that the time-step size should be lower than the diffusion time scale:

$$\Delta t \leq \frac{\rho_\psi |d|^2}{\Gamma_\psi}. \quad (3.32)$$

The stability of the source terms depends on the source term itself and specific stability analysis should be performed.

In the Euler Implicit scheme, the temporal integral of  $\psi$  is given as

$$\int_t^{t+\Delta t} \psi(t) dt = \psi^n \Delta t, \quad (3.33)$$

while in the Crank-Nicolson scheme, it follows

$$\int_t^{t+\Delta t} \psi(t) dt = \frac{1}{2} (\psi^n + \psi^o) \Delta t. \quad (3.34)$$

Both the above schemes are unconditionally stable. However, while the Crank-Nicolson scheme is second order accurate, the Euler Implicit scheme is first order accurate. Note that, though the schemes are stable, they may produce inaccurate results if the time-step is relatively high. In order to maintain accuracy and boundedness in transient problems, the value of the time-step size should remain close to the stability criteria of the various terms.

If not otherwise specified, the Crank-Nicolson scheme is used in the present thesis.

#### 3.1.3 Solution of the system of linear algebraic equation

For each control volume, the discretized form of the transport equation can be reduced to the following algebraic equation

$$a_P \psi_P^n + \sum_N a_N \psi_N^n = R_P, \quad (3.35)$$

where the coefficients  $a_P$  and  $a_N$  depends on the discretization scheme used. All the explicit terms, i.e. depending on the old time, are collected in  $R_P$ . We are interested in determining  $\psi_P^n$ . Since its value also depends on the new neighbor values, a system of algebraic equations is obtained:

$$\mathbf{A} \cdot \Psi = \mathbf{R}, \quad (3.36)$$

where  $\mathbf{A}$  is a sparse matrix with  $a_P$  on the diagonal and  $a_N$  off the diagonal.  $\Psi$  is the vector containing the values of  $\psi$  at each cell center and  $\mathbf{R}$  is the vector containing all the explicit terms expressed for each control volume.

This system can be solved using direct or iterative methods. Direct methods are particularly suited for small systems due to the high memory usage and number of operations required for large systems. As a results, iterative methods are generally used to solve fluid flow problems based on the FVM discretization. Iterative methods consist of an initial guess which is continuously updated until a given tolerance is reach. They are more economical in terms of memory and the number of iterations required to reach the given tolerance depends on the size of the problem and on the algorithm used

to update the estimates. Some requirements on the matrix  $\mathbf{A}$  also influence the number of iterations and the convergence of the method. In order to fulfill these requirements, the so-called under-relaxation of the original system of equation is commonly used, in particular when a steady-state solution is looked for.

## 3.2 Interface tracking

In section 2.2, the derivation of the governing equation using the one-fluid formulation is given. Such formulation is possible thanks to the introduction of a Heaviside function  $\chi$  which determines the spatial and temporal distribution of each phase within the solution domain. The transport equation for  $\chi$  is given as

$$\frac{\partial \chi}{\partial t} + \mathbf{u}_{\text{int}} \cdot \nabla \chi = 0, \quad (3.37)$$

which simply states that the distribution of  $\chi$  follows the boundary of phase 1.

In the present thesis, the so-called Volume-Of-Fluid (VOF) interface tracking method is used to obtain a smooth equivalent of the Heaviside function. It consists in tracking the volume fraction  $F$  of one of the phases within each control volume. The volume fraction can be defined as the volume averaged of the Heaviside function within a control volume:

$$F = \frac{1}{V_P} \int_{V_P} \chi dV. \quad (3.38)$$

This gives a straightforward derivation of the material properties. For example, the density in each control volume reads

$$\begin{aligned} \rho_P &= \frac{1}{V_P} \int_{V_P} \rho dV \\ &= \frac{1}{V_P} \int_{V_P} \chi \rho_1 + (1 - \chi) \rho_2 dV \\ &= \rho_1 \frac{1}{V_P} \int_{V_P} \chi dV + \rho_2 \frac{1}{V_P} \int_{V_P} (1 - \chi) dV \\ &= F \rho_1 + (1 - F) \rho_2. \end{aligned} \quad (3.39)$$

A similar relation is obtained for  $\mu_P$ ,  $\lambda_P$  and  $(\hat{\rho}c)_P$  are estimated differently due to the different treatments adopted for the energy equation.

The transport equation for the volume fraction can be derived from the transport equation of the Heaviside function. This gives

$$\frac{\partial F}{\partial t} + \mathbf{u}_{\text{int}} \cdot \nabla F = 0. \quad (3.40)$$

If there is no mass transfer, the boundary conditions at the interface state that the velocity field is continuous, i.e.,  $\mathbf{u}_1 = \mathbf{u}_2 = \mathbf{u}_{\text{int}}$ . Thus, using the incompressibility condition ( $\nabla \cdot \mathbf{u} = 0$ ), the transport equation of the volume fraction can be expressed in a conservative form as

$$\frac{\partial F}{\partial t} + \nabla \cdot (F \mathbf{u}) = 0. \quad (3.41)$$

### Chapter 3. Implemented numerical method

---

The volume fraction is a relatively sharp function, thus if standard convection differencing schemes are used, the interface will be diffused over several cells. In order to avoid this issue, specific schemes were developed and can be classified into two groups: geometrical schemes and high-resolution schemes.

If not otherwise specified, the high-resolution scheme of Ubbink and Issa (1999) implemented in the OpenFOAM library (OpenFOAM Foundation, 2013) is used in the present thesis. In order to avoid numerical diffusion, the interface is compressed using a suitable velocity  $\mathbf{u}_r$ . The transport equation of the volume fraction is modified as follows

$$\frac{\partial F}{\partial t} + \nabla \cdot (F \mathbf{u}) + \nabla \cdot [F(1-F) \mathbf{u}_r] = 0. \quad (3.42)$$

The semi-discretized equation of the volume fraction for each control volume reads

$$\frac{\partial F_P}{\partial t} + \frac{1}{V_P} \sum_f \left[ \langle F \rangle_{c \rightarrow f}^{\text{VL}} \phi - \langle F \rangle_{c \rightarrow f}^{\text{IC'}} \phi'_r \right] = 0, \quad (3.43)$$

where  $\langle \cdot \rangle_{c \rightarrow f}^{\text{VL}}$  denotes face interpolation using the Van Leer flux limiter and the flux  $\phi$ , and  $\langle \cdot \rangle_{c \rightarrow f}^{\text{IC'}}$  denotes face interpolation using the “interfaceCompression” convective scheme of OpenFOAM (OpenFOAM Foundation, 2013) and the flux  $\phi'_r$  calculated as

$$\phi'_r = -\langle 1 - F \rangle_{c \rightarrow f}^{\text{IC}} \phi_r, \quad (3.44)$$

with  $\langle \cdot \rangle_{c \rightarrow f}^{\text{IC}}$  calculated using the flux  $-\phi_r$  given as follows

$$\phi_r = \min \left( C_F \left| \frac{\phi}{S_f} \right|, \left| \frac{\phi}{S_f} \right| \right) \mathbf{S}_f \cdot \mathbf{n}_{\text{int}}. \quad (3.45)$$

$C_F$  is a coefficient which determines the magnitude of the compression. Its value is fixed at  $C_F = 2$  in the simulations performed in this thesis. In addition,  $\mathbf{n}_{\text{int}}$  points toward phase 1 (i.e., toward  $F = 1$ ) and is calculated as

$$\mathbf{n}_{\text{int}} = \frac{\nabla F}{|\nabla F|}. \quad (3.46)$$

Equation (3.43) is finally solved using the Multidimensional Universal Limiter with Explicit Solution (MULES) solver (OpenFOAM Foundation, 2013) in order to maintain the boundedness of the solution and to conserve the fluids’ mass.

### 3.3 Interfacial curvature calculation

---

In order to compute the surface tension term normal to the interface (see Eq. (2.71)), local estimates of the interfacial mean curvature are required. In addition, a proper implementation is required to avoid unphysical capillary forces which lead to the so-called spurious currents (Scardovelli and Zaleski, 1999; Popinet and Zaleski, 1999).

### 3.3.1 Original method: Gauss integration

A simple expression for the estimation of the interfacial curvature is given by the divergence of the interface unit normal vector

$$\kappa = -\nabla \cdot \mathbf{n}_{\text{int}}, \quad (3.47)$$

where  $\mathbf{n}_{\text{int}}$  points toward phase 1 (i.e., toward  $F = 1$ ). The original method implemented in OpenFOAM calculates the interface unit normal vector from the volume fraction gradient, as in Eq. (3.46). Then the Gauss theorem is used to estimate the divergence operator. In the following, this method will be denoted as  $\kappa_{\text{Gauss}}$  and the discretized form the interfacial curvature calculation reads

$$\kappa_{\text{Gauss}} = -\frac{1}{V_P} \sum_f \mathbf{S}_f \cdot \left( \frac{\langle \nabla F \rangle_{c \rightarrow f}}{\left| \langle \nabla F \rangle_{c \rightarrow f} \right| + \epsilon_n} \right), \quad (3.48)$$

where  $\langle \cdot \rangle_{c \rightarrow f}$  denotes linear interpolation from cell center to face center, and  $\epsilon_n$  a very small value depending on the average grid size.

### 3.3.2 First proposed method: node-based gradient

The method is similar to the original one, however more accurate estimates of the interface unit normal vectors are obtained using a node-based gradient scheme. In addition, the estimation of the Dirac delta function in the surface tension term, Eq. (3.71), is performed using a curtailed volume fraction to avoid instabilities due to residual volume fraction far from the interface.

In the node-based gradient scheme, the value of volume fraction at the face center is linearly interpolated from node values, which are linearly interpolated from cell center values. The discretized form of the interface unit normal vector is

$$\mathbf{n}_{\text{int}} = \frac{\mathbf{n}_{\text{int}}^*}{|\mathbf{n}_{\text{int}}^*| + 10^{-10}}, \quad \mathbf{n}_{\text{int}}^* = \frac{1}{V_P} \sum_f \mathbf{S}_f \langle \langle F \rangle_{c \rightarrow n} \rangle_{n \rightarrow f}. \quad (3.49)$$

This node-based gradient scheme uses larger computational stencils than in a cell-based gradient scheme, i.e., more neighboring values are employed. This results in a higher accuracy of the interface unit normal vector. The interfacial curvature,  $\kappa_{\text{nbg}}$ , is then computed using a Gauss integration of the interface unit normal vectors

$$\kappa_{\text{nbg}} = -\frac{1}{V_P} \sum_f \mathbf{S}_f \cdot \left( \frac{\langle \mathbf{n}_{\text{int}} \rangle_{c \rightarrow f}}{\left| \langle \mathbf{n}_{\text{int}} \rangle_{c \rightarrow f} \right| + 10^{-10}} \right), \quad (3.50)$$

The curtailing of the volume fraction is performed as follows

$$F_c = \frac{1}{1 - C_{F_c}} \left[ \min \left( \max \left( F, \frac{C_{F_c}}{2} \right), 1 - \frac{C_{F_c}}{2} \right) - \frac{C_{F_c}}{2} \right], \quad (3.51)$$

with  $C_{F_c} = 0.01$  for the simulations performed in this thesis.

### 3.3.3 Second proposed method: recursive weighted interpolations

As will be shown in Section 4.1.1, the local estimates of interfacial curvature obtained using the original method are poorly accurate. In particular, a non-uniform distribution of the estimates in the direction normal to the interface is obtained. An attempt to tackle these issues is made with the implementation of a method based on recursive weighted interpolations. It is similar to the method proposed by Raeini et al. (2012), however the interpolations are node-based and different weighting functions are employed. In addition, the filtering procedure introduced in Raeini et al. (2012) is not used here as well as the smoothing of the volume fraction. With the former technique, non-physical behaviors have been observed during the simulation of rising bubbles, while a decoupling between surface tension and the volume fraction has been observed when the volume fraction is smoothed.

The method will be denoted as  $\kappa_{\text{rwi}}$  and consists in the following steps:

- calculation of the interface unit normal vector from the volume fraction;
- propagation and smoothing of the interface unit normal vector;
- calculation of the interfacial curvature from the interface unit normal vector;
- propagation and smoothing of the interfacial curvature.

As with the previous method, the volume fraction is curtailed to evaluate the Dirac delta function in Eq. (3.71).

#### Calculation of the interface unit normal vector

Various methods can be used to compute the interface unit normal vectors. Here, the node-based gradient scheme introduced previously is used.

#### Propagation and smoothing of the interface unit normal vector

Since the local interface unit normal vectors are estimated at the cell center (and not on the interface), values within cells having the volume fractions approaching  $F = 0.5$  are more representative of the true interface unit normal vector than values within cells having the volume fraction close to  $F = 0$  or  $F = 1$ . Thus in order to propagate the most reliable values along the direction normal to the interface, a recursive weighted interpolation is performed. This also results in a slight smoothing of the estimates in the direction tangent to the interface. The discretized form of the new interface unit normal vector is given as

$$(\mathbf{n}_{\text{int}})_{s,i+1,j+1} = w (\mathbf{n}_{\text{int}})_{s,0,j} + (1 - w) (\mathbf{n}_{\text{int}})_s^*, \quad (3.52)$$

with

$$(\mathbf{n}_{\text{int}})_{s,0,0} = \mathbf{n}_{\text{int}}, \quad (\mathbf{n}_{\text{int}})_{s,0,j} = (\mathbf{n}_{\text{int}})_{s,i,j-1}, \quad (3.53)$$

and

$$(\mathbf{n}_{\text{int}})_s^* = \frac{\left\langle \left\langle w (\mathbf{n}_{\text{int}})_{s,i,j} \right\rangle_{c \rightarrow n} \right\rangle_{n \rightarrow c}}{\langle \langle w \rangle_{c \rightarrow n} \rangle_{n \rightarrow c}}, \quad w = \sqrt[4]{4F(1-F) + 10^{-12}}. \quad (3.54)$$

### 3.3. Interfacial curvature calculation

---

Two different loops are performed: an inner loop with index  $i$  and an outer loop with index  $j$ . Note that the new interface unit normal vector is re-normalized at the end of each inner iteration. The various simulations performed suggest a value of  $i = 2$  and  $j = 1$  for optimal accuracy and stability, i.e.,  $(\mathbf{n}_{\text{int}})_s = (\mathbf{n}_{\text{int}})_{s,2,1}$ . Outer iterations may be beneficial for highly non-orthogonal meshes.

#### Calculation of the interfacial curvature

Two schemes can be used to compute the interfacial curvature from the divergence of the interface unit normal vector: a cell-based or a node-based scheme. The discretized form of the cell-based scheme reads

$$\kappa_{\text{rwi}}^* = -\frac{1}{V_P} \sum_f \mathbf{S}_f \cdot \left( \frac{\langle(\mathbf{n}_{\text{int}})_s\rangle_{c \rightarrow f}}{\left| \langle(\mathbf{n}_{\text{int}})_s\rangle_{c \rightarrow f} \right| + 10^{-10}} \right), \quad (3.55)$$

while the node-based scheme is given as

$$\kappa_{\text{rwi}}^* = -\frac{1}{V_P} \sum_f \mathbf{S}_f \cdot \left( \frac{\langle\langle(\mathbf{n}_{\text{int}})_s\rangle_{c \rightarrow n}\rangle_{n \rightarrow f}}{\left| \langle\langle(\mathbf{n}_{\text{int}})_s\rangle_{c \rightarrow n}\rangle_{n \rightarrow f} \right| + 10^{-10}} \right). \quad (3.56)$$

If not stated otherwise, the cell-based scheme is used in the simulations presented in this thesis.

#### Propagation and smoothing the interfacial curvature

The same considerations as for the interface unit normal vector can be applied for the interfacial curvature, i.e., the most accurate estimates are within cells in which the volume fraction is closed to  $F = 0.5$ . For this reason, recursive weighted interpolations are performed as well to propagate the interfacial curvature in the direction normal to the interface. The interfacial curvature thus reads

$$(\kappa_{\text{rwi}})_{s,i+1,j+1} = w (\kappa_{\text{rwi}})_{s,0,j} + (1 - w) (\kappa_{\text{rwi}})_s^*, \quad (3.57)$$

with

$$(\kappa_{\text{rwi}})_{s,0,0} = \kappa_{\text{rwi}}^*, \quad (\kappa_{\text{rwi}})_{s,0,j} = (\kappa_{\text{rwi}})_{s,i,j-1}, \quad (3.58)$$

and

$$(\kappa_{\text{rwi}})_s^* = \frac{\langle\langle w (\kappa_{\text{rwi}})_{s,i,j} \rangle_{c \rightarrow n}\rangle_{n \rightarrow c}}{\langle\langle w \rangle_{c \rightarrow n}\rangle_{n \rightarrow c}}, \quad w = \sqrt[4]{4F(1-F) + 10^{-12}}. \quad (3.59)$$

Two loops are performed: a inner loop with index  $i$  and an outer loop with index  $j$ . The various simulations performed suggest a value of  $i = 2$  and  $j = 2$  for optimal accuracy and stability. In the following we therefore denote the interfacial curvature from this method by  $\kappa_{\text{rwi}} = (\kappa_{\text{rwi}})_{s,2,2}$ .

### 3.3.4 Height function method

The above methods for interfacial curvature calculation are implemented in the OpenFOAM library (OpenFOAM Foundation, 2013). In order to have a reference in terms of accuracy of the interfacial curvature calculation, the Gerris code is used in some of simulations presented in this thesis. A generalized height function is used in the Gerris code (Popinet, 2009) to estimate the curvature of the interface. When the interface is under-resolved, i.e., when the radius of curvature of the interface is comparable to the mesh size, consistent height functions cannot be found and the algorithm switches automatically to a parabola fitting of the interface. If the fitting is not successful, then the curvature is set to zero.

In the following,  $\kappa_{\text{hf}}$  will denote the curvature estimated using the generalized height function. When the mesh is well-resolved, the height function method is used and the curvature is computed as follows in two dimensions

$$\kappa_{\text{hf}} = \frac{-h''}{(1 + h'^2)^{3/2}} \Big|_{x_{\text{local}}=0}. \quad (3.60)$$

In axisymmetrical domains we have

$$\kappa_{\text{hf}} = \begin{cases} \frac{-h''}{(1+h'^2)^{3/2}} \Big|_{x_{\text{local}}=0} - \frac{h'}{r(1+h'^2)^{1/2}} \Big|_{x_{\text{local}}=0} & \text{if } y_{\text{local}} = -\text{sign}(n_z)z, \\ \frac{-h''}{(1+h'^2)^{3/2}} \Big|_{x_{\text{local}}=0} - \frac{\text{sign}(n_r)}{(r-\text{sign}(n_r)h)(1+h'^2)^{1/2}} \Big|_{x_{\text{local}}=0} & \text{otherwise,} \end{cases} \quad (3.61)$$

where  $h$  is the so called height function computed from the volume fraction field. At each interfacial cell, i.e., a cell containing an interface segment, a local Cartesian reference frame  $(x_{\text{local}}, y_{\text{local}})$  with origin at the cell center is set. Its orientation depends on the interface unit normal vector: if  $|n_x| > |n_y|$ , then  $y_{\text{local}} = -\text{sign}(n_x)x$  otherwise  $y_{\text{local}} = -\text{sign}(n_y)y$ , with  $\mathbf{n}_{\text{int}} = (n_x, n_y)$  pointing from  $F = 0$  to  $F = 1$ . In axisymmetrical domains we have  $\mathbf{n}_{\text{int}} = (n_r, n_z)$ . The heights of fluid are then computed by summation of the volume fraction along the  $y_{\text{local}}$ -direction, which gives an estimate of the relative interface position with respect to the  $y_{\text{local}}$ -coordinate.  $h'$  and  $h''$  are the first and second order derivatives of  $h$  with respect to the local coordinate  $x_{\text{local}}$ , estimated using centered differences.  $(r - \text{sign}(n_r)h)$  represents the distance from the interface to the  $z$ -axis. The local approximations of  $\kappa$  are then diffused to the adjacent cells to allow a uniform distribution of  $\kappa$  in the direction normal to the interface. Such a technique provides a second order accurate estimate of the curvature, however square/cubic cells are required. The validation and estimation of the numerical accuracy of the technique for surface tension driven flows is given in Popinet (2009).

## 3.4 Interfacial jumps due to heat and mass transfer

---

In this section, the treatment of the interfacial jumps due to heat and mass transfer will be described. As noticed in the previous chapter, a two-phase flow with heat and mass transfer present jumps in material properties, in the velocity field and in the temperature gradient. The modified transport equation for the volume fraction will be first

### 3.4. Interfacial jumps due to heat and mass transfer

---

introduced followed by the suitable transport equations for mass, momentum and energy. In order to solve the energy equation, a Ghost Fluid Method is implemented. Finally, the technique used to compute the mass transfer flux will be explained.

#### 3.4.1 Transport of the volume fraction

In order to derive the transport equation for the volume fraction when mass transfer occur, it is more convenient to start from the non-conservative form of the transport equation (Eq. (3.40)). The interface velocity can be expressed in function of the fluids' velocity and the mass transfer rate using the mass jump condition Eq. (2.30), the definition of the mass transfer flux Eq. (2.2) and the no-slip condition Eq. (2.49). This gives

$$\mathbf{u}_{\text{int}} = \frac{1}{2} (\mathbf{u}_1 + \mathbf{u}_2) + \frac{1}{2} \left( \frac{1}{\rho_1} + \frac{1}{\rho_2} \right) \dot{m}'' \mathbf{n}_{\text{int}}, \quad (3.62)$$

where  $\mathbf{n}_{\text{int}}$  is defined as pointing toward phase 1, i.e.,  $\mathbf{n}_{\text{int}} = \mathbf{n}_2$ , due to the way it is computed in the code. The first term represents the transport due to convection while the last term account for the mass transfer. The first term is taken into account implicitly by the one-fluid velocity,  $\mathbf{u}$ , however the transport equation needs to be modified to account for the divergence of the velocity field. For the second term, we define a velocity related to the mass transfer denoted as  $\mathbf{u}_m$ . The transport equation now reads

$$\frac{\partial F}{\partial t} + \mathbf{u} \cdot \nabla F + \mathbf{u}_m \cdot \nabla F = 0. \quad (3.63)$$

In order to solve the above equation using the FVM, it is transformed as follows

$$\frac{\partial F}{\partial t} + \nabla \cdot [F(\mathbf{u} + \mathbf{u}_m)] - F \nabla \cdot (\mathbf{u} + \mathbf{u}_m) = 0. \quad (3.64)$$

While compression of the interface could be done from the combined fluxes (due to convection and mass transfer), the simulations performed have shown that a separate compression term for each flux is preferable. Thus the transport equation finally reads

$$\begin{aligned} & \frac{\partial F}{\partial t} + \nabla \cdot [F(\mathbf{u} + \mathbf{u}_m)] - F \nabla \cdot (\mathbf{u} + \mathbf{u}_m) \\ & + \nabla \cdot [F(1 - F) \mathbf{u}_r] + \nabla \cdot [F(1 - F) \mathbf{u}_{mr}] = 0. \end{aligned} \quad (3.65)$$

The semi-discretized form follows the one derived for two-phase flow without mass transfer, with a modified flux to account for mass transfer and a source term to account for the divergence of the velocity fields.

The various simulations performed have also demonstrated an excessive smearing of the volume fraction in two- and three-dimensional simulations. To tackle this issue, additional compression steps are performed by solving the following equation

$$\frac{\partial F}{\partial \tau_c} + \nabla \cdot (F(1 - F) \mathbf{n}_{\text{int}}) = \nabla \cdot (D_F \nabla F), \quad (3.66)$$

where  $\tau_c$  is a pseudo-time and  $D_F$  is an artificial diffusion coefficient controlling the thickness of the interface. The equation is solved using a Euler explicit time discretization scheme. The term  $F(1 - F)\mathbf{n}_{\text{int}}$  is interpolated linearly to the cell faces and

### Chapter 3. Implemented numerical method

---

$D_F = \frac{\Delta}{2}$  with  $\Delta$  the mesh element size of interfacial cells. The pseudo-time-step size is defined as:

$$\Delta\tau_c = \min\left(\frac{\Delta}{2}, \frac{\Delta t}{2}\right). \quad (3.67)$$

At each time-step, two pseudo-time-steps are performed after each solution of the volume fraction. The MULES solver is used to solve (3.66) in order to maintain a bounded solution for the volume fraction.

#### 3.4.2 Mass, momentum and energy equations

Due to the jump in velocity at the interface, the interpolation used in the convection differencing scheme is ambiguous if the mass flux is used instead of the velocity flux. This is because the value of volume fraction at the face may be erroneous. For this reason, a non-conservative form of the momentum and energy equations is adopted. The conservation of mass is not considered explicitly in the equations solved, instead the condition on the divergence of the velocity field (Eq. (2.64)) is used. The Dirac delta function is approximated as the magnitude of the gradient of volume fraction, which is representative of the interfacial area density ( $A_{\text{int}}/V_P$ )

$$\delta_{\text{int}} \approx |\nabla F|. \quad (3.68)$$

The divergence of the velocity field thus reads

$$\nabla \cdot \mathbf{u} = \left( \frac{1}{\rho_2} - \frac{1}{\rho_1} \right) \dot{m}'' |\nabla F|. \quad (3.69)$$

The non-conservative form of the momentum equation is given as

$$\begin{aligned} & \rho \left( \frac{\partial \mathbf{u}}{\partial t} + \nabla \cdot (\mathbf{u} \mathbf{u}) - \mathbf{u} \nabla \cdot \mathbf{u} \right) \\ &= -\nabla p + \nabla \cdot [\mu (\nabla \mathbf{u} + \nabla \mathbf{u}^\top)] + \rho \mathbf{g} + \sigma \kappa \nabla F, \end{aligned} \quad (3.70)$$

where a constant surface tension coefficient is considered, i.e., Marangoni effects are neglected, and the Continuum-Surface-Force (CSF) approach of Brackbill et al. (1992) is used to express the surface tension term as a localized body force. This is done by approximating the Dirac delta function with the gradient of the volume fraction:

$$\sigma \kappa \delta_{\text{int}} \mathbf{n} \approx \sigma \kappa \nabla F. \quad (3.71)$$

The solution of the energy equation is the most delicate part of the model. In effect, its derivation using the one-fluid temperature and a smoothed Heaviside function, such as the volume fraction, is not trivial at all. Several terms appear from the averaging procedure (see, e.g., Whitaker (1999) and Ishii and Hibiki (2006)) that need to be closed in some way. The equation obtained is not the one derived previously, Eq. (2.79), since the Heaviside function is not sharp. Eq. (2.79) only serves as a starting point for the derivation.

For this reason, it is preferred to solve the energy equation for each phase separately, Eq. (2.21). However, since it is more efficient to solve for a single temperature field,

### 3.4. Interfacial jumps due to heat and mass transfer

---

a Ghost-Fluid-Method (GFM) is implemented to impose the Dirichlet boundary condition at the interface, i.e.,  $T_1 = T_2 = T_{\text{int}} = T_{\text{sat}}$ . The method proposed by Gibou et al. (2002) is used to modify the stencil used in the implicit calculation of the diffusion term. In the simulations performed in this thesis, the convection term is not corrected to account for the temperature at the interface. Modifying the convection term may thus constitute an improvement of the present model.

The non-conservative form of the energy equation, expressed in terms of the one-fluid temperature, thus reads

$$\widehat{\rho c} \left( \frac{\partial T}{\partial t} + \nabla \cdot (T \mathbf{u}) - T \nabla \cdot \mathbf{u} \right) = \nabla \cdot (\lambda \nabla T), \quad (3.72)$$

with  $\widehat{\rho c}$  and  $\lambda$  expressed using a sharp Heaviside function estimated at cell center, i.e.,

$$\begin{aligned} \widehat{\rho c}_P &= \chi_P \rho_1 c_1 + (1 - \chi_P) \rho_2 c_2, \\ \lambda_P &= \chi_P \lambda_1 + (1 - \chi_P) \lambda_2, \end{aligned} \quad (3.73)$$

where

$$\chi_P = \begin{cases} 1 & \text{if } F \geq 0.5, \\ 0 & \text{otherwise.} \end{cases} \quad (3.74)$$

#### 3.4.3 Calculation of the mass transfer flux

The mass transfer flux  $\dot{m}''$  is given by the enthalpy jump condition Eq. (2.47). After rearranging the terms and considering an interface unit normal vector pointing towards phase 1, this gives

$$\dot{m}'' = \frac{\lambda_1 \nabla_n T_1 - \lambda_2 \nabla_n T_2}{h_{21}}. \quad (3.75)$$

Since the temperature field is shared by both phases, it is not possible to estimate the normal gradients of temperature at the interface using standard discretization schemes.

In the present thesis, the method implemented by Kunkelmann (2011) is employed. It consists in performing a contour-based reconstruction of the interface, i.e., the surface of iso-value  $F = 0.5$  is search within each cell. From this reconstruction, it is possible to compute a signed distance function to the interface  $d_{\text{int}}$ , also called level-set. By convention, the level-set is positive within phase 1, negative within phase 2 and null at the interface. Using the reconstructed level-set, it is then possible to estimate the normal gradients of temperature using the following relation

$$\nabla_n T_k = \frac{T_k - T_{\text{int}}}{d_{\text{int}}}, \quad (3.76)$$

which is valid for both phase since the level-set changes sign.

In order to improve the accuracy of the estimates, the gradients are not computed directly in cells containing a reconstructed interface, i.e., “interfacial cells”. Instead, they are computed using the neighboring cells which are not interfacial cells. The value of the gradient of each phase is then propagated by recursively averaging neighboring values as suggested in Kunkelmann (2011).

### 3.5 Pressure-velocity coupling

---

Because of the flow incompressibility, the pressure term needed in Eq. (3.70) cannot be determined by an explicit transport equation. In order to derive an equation for the pressure, the condition on the divergence of the velocity field will be used together with the momentum equation. A segregated algorithm is then used to solve the system of equations.

The non-linear term in the momentum equation ( $\nabla \cdot (\mathbf{u}\mathbf{u})$ ) is linearized in order to reduce the complexity of the system of equations. That is the face velocity flux is treated as explicit and satisfy the conservation of mass equation as well as the condition on the divergence of the velocity.

The discretized form of the momentum equation (Eq. (3.70)) expressed for each control volume can be written as follows

$$a_P \mathbf{u}_P^n + \sum_N a_N \mathbf{u}_N^n = \mathbf{r}_P - (\nabla p)_P^n. \quad (3.77)$$

where the coefficients  $a_P$ ,  $a_N$  and the source terms  $\mathbf{r}_P$  depend on the unknown velocity field due to the explicit treatment of the some terms such as the face velocity flux and the non-orthogonal corrections.

The discretized form of the condition on the divergence of the velocity field (Eq. (3.69)) reads

$$\sum_f \mathbf{S}_f \cdot \mathbf{u}_f^n = \sum_f \phi_f = \left( \frac{1}{\rho_2} - \frac{1}{\rho_1} \right) \dot{m}_P'' (|\nabla F|)_P, \quad (3.78)$$

where  $\phi_f$  is face velocity flux. The new velocity can be obtained as follow

$$\boxed{\mathbf{u}_P^n = \frac{\mathbf{H}_P(\mathbf{u}^n)}{a_P} - \frac{1}{a_P} (\nabla p)_P^n,}$$

(3.79)

where

$$\mathbf{H}_P(\mathbf{u}^n) = - \sum_f a_N \mathbf{u}_N^n + \mathbf{r}_P^n. \quad (3.80)$$

The face velocity in Eq. (3.78) can be expressed similarly as

$$\mathbf{u}_f^n = \left( \frac{\mathbf{H}}{a} \right)_f - \left( \frac{1}{a} \right)_f (\nabla p)_f^n, \quad (3.81)$$

where  $(\mathbf{H}/a)_f$  and  $(1/a)_f$  are obtained from interpolation of their counterparts in the two cells sharing the face. In OpenFOAM this is done using a Rhee-Chow interpolation (Rhee and Chow, 1983), which is modified to prevent a checkerboard pressure field at very small time step (Yu et al., 2002). In the original Rhee-Chow interpolation, we have

$$\left( \frac{\mathbf{H}}{a} \right)_f^{\text{RC}} = \left\langle \frac{\mathbf{H}_P(\mathbf{u}^n)}{a_P} \right\rangle_{c \rightarrow f}, \quad \left( \frac{1}{a} \right)_f^{\text{RC}} = \left\langle \frac{1}{a_P} \right\rangle_{c \rightarrow f}, \quad (3.82)$$

### 3.5. Pressure-velocity coupling

In OpenFOAM, the first of the above equations is modified as follows

$$\left(\frac{\mathbf{H}}{a}\right)_f^{\text{mRC}} = \left(\frac{\mathbf{H}}{a}\right)_f^{\text{RC}} + \frac{C_{\text{mRC}}}{\Delta t} \mathbf{n}_f \left[ \left\langle \frac{\rho_P^o}{a_P} \right\rangle_{c \rightarrow f} \frac{\phi_f^o}{S_f} - \left( \mathbf{n}_f \cdot \left\langle \frac{\rho_P^o \mathbf{u}_P^o}{a_P} \right\rangle_{c \rightarrow f} \right) \right], \quad (3.83)$$

where

$$C_{\text{mRC}} = 1 - \min \left( \frac{\left| \phi_f^o - \mathbf{S}_f \cdot \langle \mathbf{u}_P^o \rangle_{c \rightarrow f} \right|}{|\phi_f^o| + \epsilon_\phi}, 1 \right), \quad (3.84)$$

with  $\epsilon_\phi$  a very small number.

Substituting Eq. (3.81) into Eq. (3.78), the equation for pressure is obtained

$$\boxed{\sum_f \left(\frac{1}{a}\right)_f^{\text{RC}} \mathbf{S}_f \cdot (\nabla p)_f^n = \sum_f \mathbf{S}_f \cdot \left(\frac{\mathbf{H}}{a}\right)_f^{\text{mRC}} - \left(\frac{1}{\rho_2} - \frac{1}{\rho_1}\right) \dot{m}_P'' (|\nabla F|)_P}, \quad (3.85)$$

where  $\mathbf{S}_f \cdot (\nabla p)_f^n$  is calculated using Eq. (3.21). After the solution of the pressure from the above equation, the conservative velocity fluxes at the faces are obtained as follows:

$$\boxed{\phi_f^n = \mathbf{S}_f \cdot \left(\frac{\mathbf{H}}{a}\right)_f^{\text{mRC}} - \left(\frac{1}{a}\right)_f^{\text{RC}} \mathbf{S}_f \cdot (\nabla p)_f^n.} \quad (3.86)$$

The cell centered velocity field is then updated using Eq. (3.79).

The form of the equations shows linear dependence of velocity on pressure and vice-versa. This inter-equation coupling requires a special treatment. The Pressure Implicit with Splitting of Operators (PISO) algorithm, originally proposed by Issa (1986), is adopted in the present thesis. Coupling between pressure and velocity is achieved in this method as follows:

- **Momentum predictor:** the momentum equation (Eq. (3.77)) is solved using the pressure gradient at the previous time-step ( $(\nabla p)_P^o$ ). The gives an approximation of the new velocity from which the old pressure gradient is removed.
- **Pressure solution:** the predicted velocities are used to assemble the  $\mathbf{H}_P(\mathbf{u})$  operator. Using the modified Rhee-Chow interpolation, the pressure equation (Eq. (3.85)) is solved. This provides an estimate of the new pressure field.
- **Explicit velocity correction:** using the pressure solution, the face velocity fluxes are made conservative using Eq. (3.86). The velocity field is also corrected using Eq. (3.79). Since the  $\mathbf{H}_P(\mathbf{u})$  operator is calculated using the predicted velocities, the correction is explicit.

In order to account for the error from the transported influence of neighboring velocities (the  $\mathbf{H}_P(\mathbf{u})/a_P$  term in Eq. (3.79)), the pressure solution and explicit velocity correction steps are repeated. In each loop, the  $\mathbf{H}_P(\mathbf{u})$  term is updated using the new velocity field. However, the new face velocity flux is not updated in the  $\mathbf{H}_P(\mathbf{u})$  operator because a solution of the momentum equation is required, i.e., the momentum predictor step should be repeated. It is therefore assumed that the non-linear coupling is less important than the pressure-velocity coupling.

If not stated otherwise, two pressure solution - explicit velocity correction loops are performed in the simulations presented in this thesis.

## 3.6 Treatment of body forces

---

When body forces are added to the problem, an important issue is raised if they are predominant with respect to the convection and diffusion terms. For instance, in the case of a null velocity field, the pressure gradient term should balance the body forces locally. If this condition is not satisfied, unphysical velocities appear due to the local imbalances. In practice, the operator used to express the pressure gradient should be similar to the operator used to express the body forces.

### 3.6.1 Gravity acceleration

The gravity acceleration term does not show a gradient operator in its original form. In order to apply compatible gradient operator between pressure and gravity, a modified pressure,  $p^*$ , is introduced as follows:

$$p^* = p - \rho \mathbf{g} \cdot \mathbf{x}, \quad (3.87)$$

where  $\mathbf{x}$  is the position vector. The modified pressure is simply the pressure removed from its hydrostatic component. Hence, assuming quiescent fluids, the modified pressure is zero. Taking the gradient of  $p^*$ , we have

$$\begin{aligned} \nabla p^* &= \nabla p - \nabla (\rho \mathbf{g} \cdot \mathbf{x}) \\ &= \nabla p - \rho \mathbf{g} - \mathbf{g} \cdot \mathbf{x} \nabla \rho, \end{aligned} \quad (3.88)$$

where we used the fact that  $(\nabla \mathbf{x})$  gives the identity matrix and that the cross products  $(\nabla \times \mathbf{x})$  and  $(\nabla \times \mathbf{g})$  lead to a null vector. The pressure gradient and gravity terms in the momentum equation, Eq. (3.70), can therefore be substituted by the gradient of the modified pressure and the gradient of the density by the inner product of the gravity vector and position vector. That is

$$-\nabla p + \rho \mathbf{g} = -\nabla p^* + \mathbf{g} \cdot \mathbf{x} \nabla \rho, \quad (3.89)$$

Since the gravity effects are now expressed using a gradient operator, it is possible to satisfy the condition previously introduced. This is done by modifying the pressure equation, Eq. (3.85), as follows

$$\begin{aligned} \sum_f \left( \frac{1}{a} \right)_f^{\text{RC}} \mathbf{S}_f \cdot (\nabla p^*)_f^n &= \sum_f \mathbf{S}_f \cdot \left( \frac{\mathbf{H}}{a} \right)_f^{\text{mRC}} \\ &- \sum_f \left( \frac{1}{a} \right)_f^{\text{RC}} (\mathbf{g} \cdot \mathbf{x}_f) \mathbf{S}_f \cdot (\nabla \rho)_f - \left( \frac{1}{\rho_2} - \frac{1}{\rho_1} \right) \dot{m}_P'' (|\nabla F|)_P, \end{aligned} \quad (3.90)$$

### 3.6. Treatment of body forces

where both  $(\mathbf{S}_f \cdot (\nabla p^*)_f^n)$  and  $(\mathbf{S}_f \cdot (\nabla \rho)_f)$  terms are calculated using Eq. (3.21), and  $\mathbf{x}_f$  is the position vector of the face center. The face velocity fluxes and cell centered velocities are then corrected as follows

$$\begin{aligned}\phi_f^n &= \mathbf{S}_f \cdot \left( \frac{\mathbf{H}}{a} \right)_f^{\text{mRC}} - \left( \frac{1}{a} \right)_f^{\text{RC}} \mathbf{S}_f \cdot (\nabla p^*)_f^n \\ &\quad - \left( \frac{1}{a} \right)_f^{\text{RC}} (\mathbf{g} \cdot \mathbf{x}_f) \mathbf{S}_f \cdot (\nabla \rho)_f,\end{aligned}\tag{3.91}$$

$$\begin{aligned}\mathbf{u}_P^n &= \frac{\mathbf{H}_P(\mathbf{u}^n)}{a_P} - \frac{1}{a_P} \left\langle \mathbf{S}_f \cdot (\nabla p^*)_f^n \right\rangle_{f \rightarrow c} \\ &\quad - \frac{1}{a_P} \left\langle (\mathbf{g} \cdot \mathbf{x}_f) \mathbf{S}_f \cdot (\nabla \rho)_f \right\rangle_{f \rightarrow c},\end{aligned}\tag{3.92}$$

where  $\langle \cdot \rangle_{f \rightarrow c}$  means reconstruction of the cell center vector from the face fluxes. Such estimation of the pressure gradient and gravity acceleration at the cell center is necessary to get the balance between the two terms. In addition, the face normal gradient operator used in the calculations also includes the non-orthogonal correction. Thus the method is also well suited to general meshes.

#### 3.6.2 Surface tension

In the spirit of the “balanced” formulation proposed by Francois et al. (2006), the implementation of surface tension is performed in a similar manner as for the gravity acceleration. The form of the surface tension source in the CSF approach of Brackbill et al. (1992), Eq. (3.71), includes the gradient of the volume fraction. The implementation within the momentum and pressure equations is therefore straightforward. The final form of the discretized pressure equation and the discretized face velocity fluxes and cell centered velocities corrections are given as

$$\boxed{\begin{aligned}\sum_f \left( \frac{1}{a} \right)_f^{\text{RC}} \mathbf{S}_f \cdot (\nabla p^*)_f^n &= \sum_f \mathbf{S}_f \cdot \left( \frac{\mathbf{H}}{a} \right)_f^{\text{mRC}} \\ &\quad - \sum_f \left( \frac{1}{a} \right)_f^{\text{RC}} (\mathbf{g} \cdot \mathbf{x}_f) \mathbf{S}_f \cdot (\nabla \rho)_f \\ &\quad + \sum_f \left( \frac{1}{a} \right)_f^{\text{RC}} \sigma(\kappa)_f \mathbf{S}_f \cdot (\nabla F)_f - \left( \frac{1}{\rho_2} - \frac{1}{\rho_1} \right) \dot{m}_P''(|\nabla F|)_P,\end{aligned}}\tag{3.93}$$

$$\boxed{\begin{aligned}\phi_f^n &= \mathbf{S}_f \cdot \left( \frac{\mathbf{H}}{a} \right)_f^{\text{mRC}} - \left( \frac{1}{a} \right)_f^{\text{RC}} \mathbf{S}_f \cdot (\nabla p^*)_f^n \\ &\quad - \left( \frac{1}{a} \right)_f^{\text{RC}} (\mathbf{g} \cdot \mathbf{x}_f) \mathbf{S}_f \cdot (\nabla \rho)_f + \left( \frac{1}{a} \right)_f^{\text{RC}} \sigma(\kappa)_f \mathbf{S}_f \cdot (\nabla F)_f,\end{aligned}}\tag{3.94}$$

$$\boxed{\begin{aligned}\mathbf{u}_P^n &= \frac{\mathbf{H}_P(\mathbf{u}^n)}{a_P} - \frac{1}{a_P} \left\langle \mathbf{S}_f \cdot (\nabla p^*)_f^n \right\rangle_{f \rightarrow c} \\ &\quad - \frac{1}{a_P} \left\langle (\mathbf{g} \cdot \mathbf{x}_f) \mathbf{S}_f \cdot (\nabla \rho)_f \right\rangle_{f \rightarrow c} + \frac{1}{a_P} \left\langle \sigma(\kappa)_f \mathbf{S}_f \cdot (\nabla F)_f \right\rangle_{f \rightarrow c},\end{aligned}} \quad (3.95)$$

where  $(\mathbf{S}_f \cdot (\nabla F)_f)$  is calculated using Eq. (3.21). Though a weighted interpolation may be used for the evaluation of the face curvature  $(\kappa)_f$ , as suggested in Renardy and Renardy (2002) and Raeini et al. (2012), a standard linear interpolation has proven more stable results in the simulations performed, in particular when the interface is moving. Note that for the *node-based gradient* and *recursive weighted interpolations* methods,  $(\nabla F)_f$  is evaluated using a curtailed volume fraction,  $F_c$ , obtained from Eq. (3.51).

### 3.7 Solution procedure

---

The final solution procedure is given as:

1. Solve volume fraction transport equation;
2. Compute the level-set using the contour-based reconstruction of the interface;
3. Calculate the interface properties (normal, curvature) and propagate them;
4. Update material properties  $(\rho, \mu, c, \lambda)$
5. Solve the energy equation;
6. Calculate the heat and mass transfer source terms;
7. Momentum predictor;
8. PISO loop (2 iterations)
  - (a) Pressure solution;
  - (b) Explicit velocity correction;
9. Return to 1. if total time not reached.

---

# CHAPTER 4

---

## Verification and validation of the method

---

In this chapter, the validation of the numerical method is presented. First the validation of the two-phase model for the isothermal case is given, with proper benchmarks. Then the validation of the two-phase model with heat and mass transfer is introduced.

### 4.1 Isothermal two-phase model

The validation of the isothermal two-phase model is firstly performed through the estimation of the interfacial curvature of a perfectly spherical interface. Then the typical test case of a stationary axisymmetric circular interface is performed after introducing the concept of spurious currents. Finally, the capillary wave test case for the air-water system is analyzed to give insights into the temporal accuracy of the methods.

#### 4.1.1 Interfacial curvature estimates of a perfectly spherical interface

In order to verify and compare the accuracy of the various interfacial curvature calculation methods, a convergence study is performed, using routines written ad hoc in MATLAB® language (The MathWorks, 2011). A unit square domain, discretized using a uniform orthogonal mesh, is considered. Cylindrical coordinates,  $(r, z)$ , with axisymmetry and zero normal gradient boundary conditions are adopted. The accuracy of Eqs. (3.48), (3.50), (3.57) and (3.60) is evaluated via a perfectly spherical interface of radius  $r_e = 0.75$ , centered at the origin. The exact solution for the curvature is  $\kappa_{\text{exact}} = 2/r_e$ . Various mesh resolutions ranging from  $16 \times 16$  ( $r_e/\Delta = 12$ ) to  $256 \times 256$  ( $r_e/\Delta = 192$ ) are adopted, where  $\Delta$  is the mesh element size.

The volume fraction field used in the present analysis is calculated in a particular way so that it corresponds exactly to the spherical interface. For each mesh resolution, the analytical surface representation of the spherical interface is intersected with the

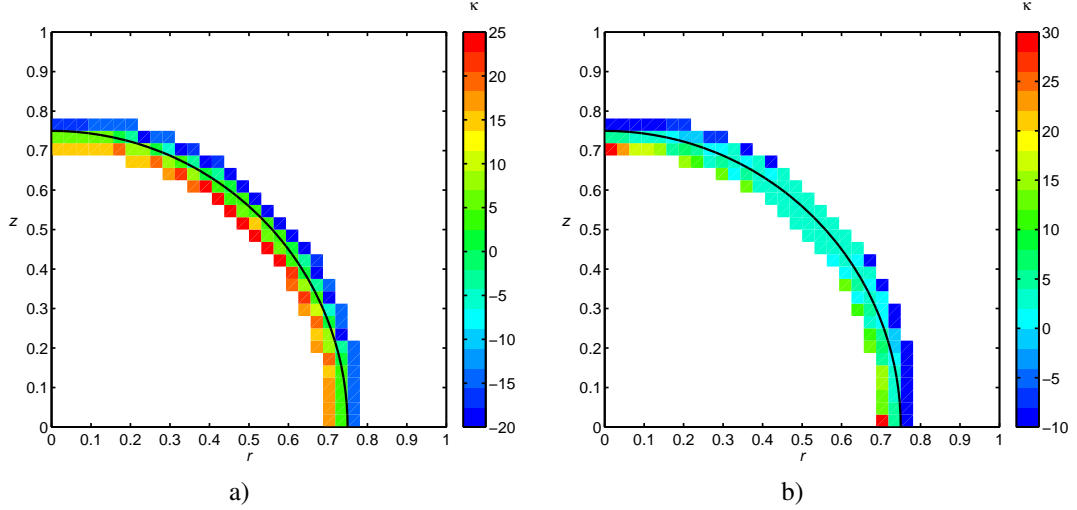


**Figure 4.1:** Cell contour of the estimated interfacial curvature of a perfectly spherical interface using a) the Gauss method and b) the node-based gradient method ( $r_e/\Delta = 24$ ).

underlying mesh. Using the intersection with the edges of the mesh, triangle or quadrilateral are obtained in cells cut by the interface (“interfacial cells”). The area of the intersection is then computed by summation of the area of the triangle or quadrilateral and the remaining circular segment. The volume fraction is then given by the ratio between the intersection area and the cell area.

The results in terms of contour of the estimated interfacial curvature at the cell center are displayed in Figure 4.1 and Figure 4.2 for the *Gauss* and *node-based gradient* methods, and the *recursive weighted interpolations* and *height function* methods respectively, using a mesh resolution of  $32 \times 32$  ( $r_e/\Delta = 24$ ). Only interfacial cells and a layer of one cell width above and below the interfacial cells are displayed. As it can be observed in the previous chapter, cell center values in the neighborhood of an interface are required to compute the surface tension term. Non-null capillary forces therefore appear in the interfacial cells as well as in the one-cell neighborhood of the interfacial cells (as displayed in Figure 4.1 and Figure 4.2). Consequently, accurate estimates of interfacial curvature should also be available in the one-cell neighborhood of the interfacial cells. With the *Gauss* and *node-based gradient* methods (see Figure 4.1), the most accurate estimates are in the interfacial cells while the worst estimates lie in the one cell neighborhood, with negative interfacial curvatures in the cells above the interface. On the other hand, the results obtained with the *recursive weighted interpolations* and the *height function* methods (see Figure 4.2) show a more uniform distribution with more accurate estimates, in particular for the *height function* method (the exact interfacial curvature is  $\kappa_{\text{exact}} = 2.6667$ ). In these cases, the uniform distribution is due to the method used to diffuse the local interfacial curvature estimates.

The results in terms of the relative maximum error norm of the interfacial curvature with respect to the mesh resolution are presented in Figure 4.3. The relative maximum error norm of the interfacial curvature  $L_\infty(\kappa)$  is calculated as follow

$$L_\infty(\kappa) = \frac{\max(|\kappa - \kappa_{\text{exact}}|)}{\kappa_{\text{exact}}} \quad (4.1)$$

#### 4.1. Isothermal two-phase model

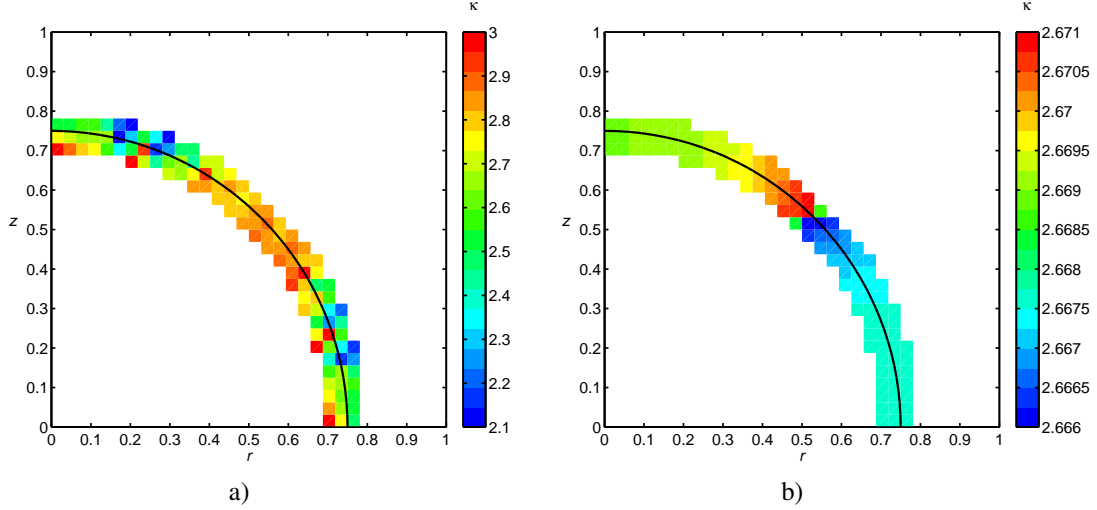


**Figure 4.2:** Cell contour of the estimated interfacial curvature of a perfectly spherical interface using a) the recursive weighted interpolations method and b) the height function method ( $r_e/\Delta = 24$ ).

with  $\kappa$  taken from the interfacial cells and its one-cell neighborhood. The present analysis shows that the maximum error norm of the *Gauss*, *node-based gradient* and *recursive weighted interpolations* methods diverges with mesh refinement. However the *recursive weighted interpolations* shows more accurate estimate with differences of one to two orders of magnitude in the relative error norm. On the other hand, a second order convergence is obtained for the *height function* method (as expected from the analyses performed by Popinet (2009)). Therefore computing the interfacial curvature using the *height function* method (Eq. (3.60)) is expected to perform well compared to the other schemes. Similar results have been obtained in Magnini et al. (2013a), in which a comparison of the *Gauss* method with a self-implementation of the *height function* method in ANSYS FLUENT (ANSYS, 2010), using external routines, is presented. We note however that due to the uniform distribution of the estimates, the *recursive weighted interpolations* method should be more stable than the *Gauss* method.

Another aspect that can be observed from the present analysis is that due to the discretization, the initial shape of the interface is not “numerically” spherical (see Figure 4.2). Therefore, an initial oscillating transient is expected in each simulation because the interface tends to evolve toward the “numerically” spherical shape, or a shape that balance the various forces. It is important to note that the velocity field observed in this preliminary phase may be a physical velocity field.

##### 4.1.2 Description of the spurious currents

Spurious currents are unphysical velocities appearing near the two-phase interface and can lead to unphysical deformations of the interface depending on their magnitude (Scardovelli and Zaleski, 1999; Popinet and Zaleski, 1999). Their origin is often attributed to the calculation of surface tension. Indeed, combining Eqs. (3.71) and (3.70) (with gravity switched off) and considering a perfectly spherical bubble, the pressure

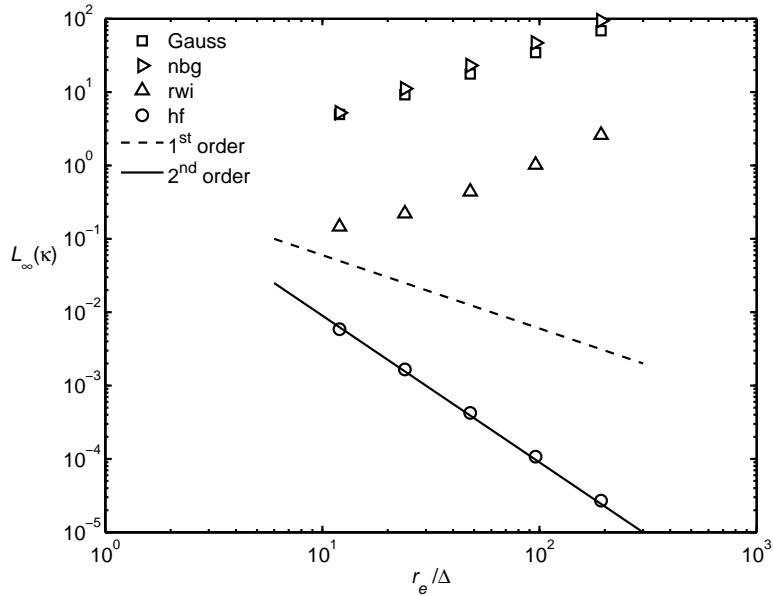


**Figure 4.3:** Convergence rate of the relative error norm  $L_\infty(\kappa)$  computed from interfacial cells and its one-cell neighborhood.

field should satisfy

$$\nabla p = \sigma \kappa \nabla F. \quad (4.2)$$

As pointed by Renardy and Renardy (2002), Francois et al. (2006) and Popinet (2009), the above equation can be verified if the gradient operators used in Eq. (4.2) are consistent and if the estimated curvature is constant. The first condition can be verified by using a balanced Continuum Surface Force method (Francois et al., 2006), which is implemented in the numerical method adopted in the present study, as described in the previous chapter. A balanced formulation is also implemented in the Gerris Flow Solver code (Popinet, 2009) used for the simulations using the *height function* method. The second condition can be satisfied by diffusing the local interfacial curvature estimates in the direction normal to the interface, provided that the local estimates are enough accurate. When one of the above conditions is not achieved, local imbalances between the pressure gradient and capillary force appear, which may lead to unphysical velocities.

Referring to Section 4.1.1, the *Gauss* and *node-based gradient* methods present a non-uniform distribution of the estimated interfacial curvature along the direction normal to the interface. As a consequence, the second condition may be hardly satisfied and spurious currents are expected to be observed for these methods within the simulations performed in this thesis. Spurious currents are also expected with the *recursive weighted interpolations* method due to the slightly noisy distribution of interfacial curvature, however the magnitude of the spurious currents should be smaller than with the first two methods.

**Table 4.1:** Summary of the mesh element sizes.

Resolution	$\max(d_e/\Delta)$	$\min(d_e/\Delta)$
Coarse	20	5
Intermediate	40	5
Fine	80	5

### 4.1.3 Stationary axisymmetric circular interface

The simulation of a stationary interface is a typical benchmark for the evaluation of the magnitude of the spurious currents obtained with a given interfacial curvature calculation method. In effect, the exact solution is a null velocity field and a pressure jump across the interface given by the Laplace law,

$$p_g - p_l = \sigma\kappa, \quad (4.3)$$

which permits to isolate the effects of surface tension from the other driving forces usually present in real applications.

In the present study, air bubbles in water are analyzed, with three different bubble diameters,  $d_e$ , corresponding to the diameters used in the rising bubble simulations in Chapter 5. An axisymmetric formulation is adopted and the dimensions of the computational domain are  $[0, 3d_e]$  in the  $r$ -direction and  $[0, 3d_e]$  in the  $z$ -direction. The bubble is initially positioned at the origin  $(0, 0)$ . Three different mesh element sizes are analyzed and the computational mesh is obtained using static local refinements as follows ( $\mathbf{x} = (r, z)$  is the cell center position vector):

- a background mesh of  $16 \times 16$  elements ( $d_e/\Delta \approx 5$ ) is generated;
- the elements with  $|\mathbf{x}|$  below  $1.5d_e$  are refined one time ( $d_e/\Delta \approx 10$ );
- the elements with  $|\mathbf{x}|$  below  $d_e$  are refined until the desired resolution is reached.

The characteristics of the different meshes are summarized in Table 4.1 and the computational domain for the *coarse* mesh resolution is displayed in Figure 4.4. The boundary conditions adopted are axisymmetry for the left boundary and imposed pressure for the other boundaries with a null normal gradient to the boundary for the velocity components (see Figure 4.4 for details). The computational mesh for the other resolutions are displayed in Figure 4.5.

The initial conditions are null velocity and pressure fields. For the first three methods, the volume fraction field is initialized by the following equation:

$$F = \max \left[ \min \left( 1 - \frac{|\mathbf{x}| - d_e/2 + \Delta}{2\Delta}, 1 \right), 0 \right], \quad (4.4)$$

which provides a volume fraction field of a circular interface of diameter  $d_e$ , diffused over two mesh elements. This is suitable for the interface tracking method adopted in OpenFOAM, which diffuses the volume fraction over 2 to 3 mesh elements. Within the Gerris code, the volume fraction is initialized using the intersections of the analytical circular shape with the edges of the mesh.

## Chapter 4. Verification and validation of the method

---

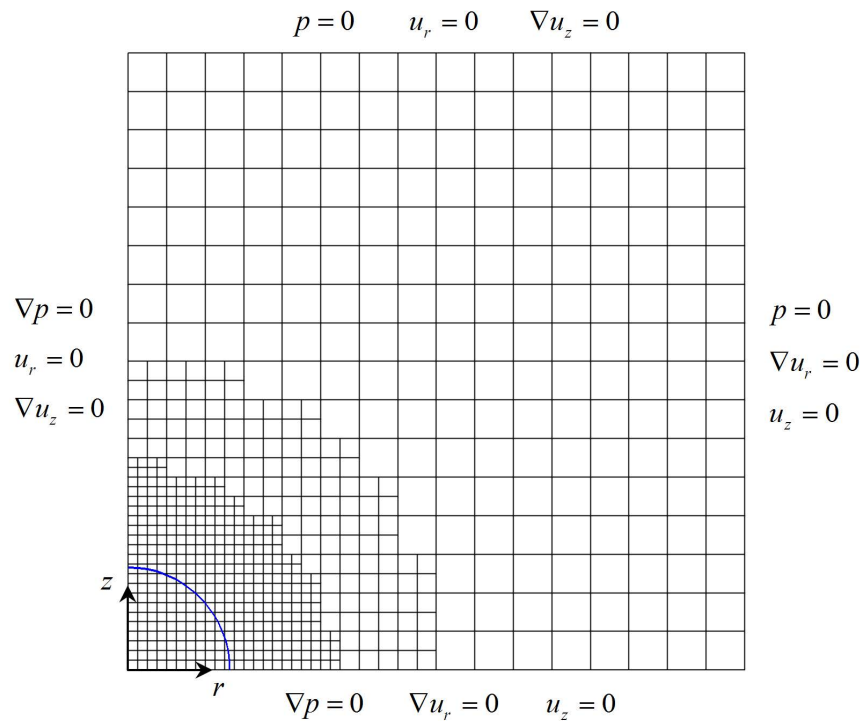


**Figure 4.4:** Boundary conditions and computational mesh corresponding to the coarse resolution.

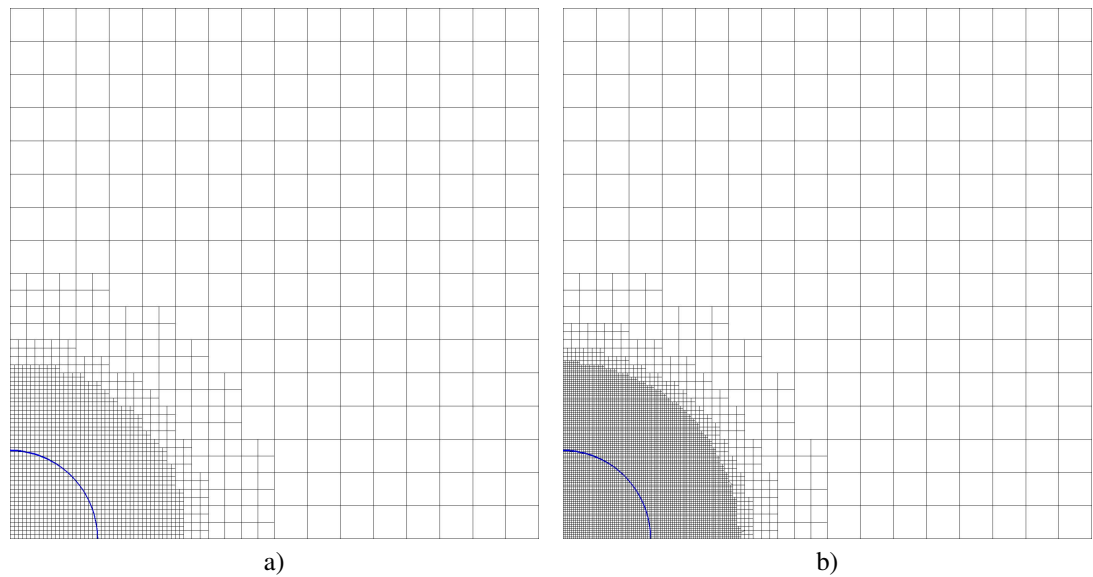


**Figure 4.5:** Computational mesh corresponding to the a) intermediate and b) fine resolutions.

#### 4.1. Isothermal two-phase model

---

Liquid water ( $\rho_l = 1000 \text{ kg m}^{-3}$ ;  $\mu_l = 10^{-3} \text{ Pa s}$ ) and air ( $\rho_g = 1.225 \text{ kg m}^{-3}$ ;  $\mu_g = 1.73 \times 10^{-5} \text{ Pa s}$ ) are used as working fluids, with a surface tension coefficient typical of ambient conditions ( $\sigma = 0.0728 \text{ N m}^{-1}$ ). The three bubble size scenarios are indicated as “Large,” “Medium” and “Small” corresponding to the diameters 0.9mm, 0.5mm and 0.3mm, respectively.

The total physical duration of the simulation is calculated according to the following viscous time scale:

$$T_\mu = \frac{\rho_l d_e^2}{\mu_l}, \quad (4.5)$$

where the  $l$  subscript relates to the liquid phase. The time is made dimensionless using  $T_\mu$ , and the time-step size is determined such that:

$$CFL < 0.1, \quad (4.6)$$

$$\Delta t < \frac{\rho_g \Delta^2}{\mu_g}, \quad (4.7)$$

$$\Delta t < \sqrt{\frac{\frac{(\rho_l + \rho_g)}{2} \Delta^3}{\pi \sigma}}, \quad (4.8)$$

where the subscript  $g$  relates to the gaseous phase. Following such criteria, the inertial, viscous and capillary time scales are well resolved and the boundedness of the solution is guaranteed.

Table 4.2 summarizes the results in terms of the maximum dimensionless velocity and the pressure jump across the interface, at time  $t = T_\mu$ . The velocity is made dimensionless using the following velocity scale

$$U_\sigma = \sqrt{\frac{\sigma}{\rho_l d_e}}. \quad (4.9)$$

The relative error in the pressure jump is calculated using the Laplace law (Eq. (4.3)). Large differences are observed between the *height function* method and the other methods concerning the maximum magnitude of the spurious currents. Moreover, a continuous reduction of the maximum velocity with time is noticed with the *height function* method while it remains constant for the other methods, indicating a converging behavior for the *height function* method only. Despite these differences, a smaller magnitude of the spurious currents is observed with the *recursive weighted interpolations* method with respect to the first two methods. This may be explained by the higher accuracy in the interfacial curvature estimates, as noted in Section 4.1.1. Concerning the pressure jump, very good accuracy is obtained with the *height function* and *recursive weighted interpolations* methods while a relatively high error is noticed for the *Gauss* and *node-based gradient* methods.

It is important to note that all these results for the first three methods do not improve with mesh refinement. This is explained by the fact that the accuracy of the interfacial curvature estimates do not converge with mesh refinement, as shown in Section 4.1.1. Despite only the results for the Coarse mesh resolution are displayed in Table 4.2 for the *height function* method, a convergence of the results with mesh refinement is obtained with this method.

## Chapter 4. Verification and validation of the method

---

**Table 4.2:** Maximum dimensionless velocity and pressure jump obtained in the static bubble simulations at time  $t = T_\mu$ .

Case	$\Delta p_{\text{ref}}$ [Pa]	Method	Mesh	$ \mathbf{u} _{\max}/U_\sigma$	$\Delta p$ [Pa]	Error $\Delta p$ [%]
Large	323.6	Gauss	Coarse	2.16	303.4	6.2
			Intermediate	2.06	301.8	6.7
			Fine	1.88	305.1	5.7
		nbg	Coarse	$4.79 \times 10^{-1}$	313.3	3.2
			Intermediate	$7.23 \times 10^{-1}$	312.7	3.4
			Fine	1.20	309.5	4.4
		rwi	Coarse	$3.01 \times 10^{-1}$	324.2	0.2
			Intermediate	$5.74 \times 10^{-2}$	321.7	0.6
			Fine	$4.90 \times 10^{-2}$	321.5	0.6
		hf	Coarse	$3.97 \times 10^{-6}$	324.9	0.4
Medium	582.4	Gauss	Coarse	1.85	546.0	6.3
			Intermediate	1.78	546.0	6.3
			Fine	1.87	549.5	5.6
		nbg	Coarse	$3.81 \times 10^{-1}$	564.0	3.2
			Intermediate	$3.83 \times 10^{-1}$	564.2	3.1
			Fine	$8.61 \times 10^{-1}$	558.5	4.1
		rwi	Coarse	$2.60 \times 10^{-1}$	583.3	0.2
			Intermediate	$4.20 \times 10^{-2}$	580.1	0.4
			Fine	$3.35 \times 10^{-2}$	579.0	0.6
		hf	Coarse	$5.35 \times 10^{-6}$	584.7	0.4
Small	970.7	Gauss	Coarse	1.60	910.0	6.2
			Intermediate	1.49	907.5	6.5
			Fine	1.17	916.3	5.6
		nbg	Coarse	$3.07 \times 10^{-1}$	939.9	3.2
			Intermediate	$2.73 \times 10^{-1}$	940.0	3.2
			Fine	$6.47 \times 10^{-1}$	931.5	4.0
		rwi	Coarse	$1.95 \times 10^{-1}$	972.5	0.2
			Intermediate	$3.26 \times 10^{-2}$	967.2	0.4
			Fine	$2.33 \times 10^{-2}$	965.1	0.6
		hf	Coarse	$7.04 \times 10^{-6}$	974.6	0.4

$$\text{Error } \Delta p [\%] = 100 |\Delta p - \Delta p_{\text{ref}}| / \Delta p_{\text{ref}};$$

$$\Delta p_{\text{ref}} = \sigma \kappa_{\text{exact}};$$

## 4.1. Isothermal two-phase model

---

**Table 4.3:** Summary of the fluid properties for the capillary wave test case.

Fluid	density $\rho$ [kg/m <sup>3</sup> ]	dynamic viscosity $\mu$ [kg/(m s)]
Air	1.2	$1.8 \times 10^{-5}$
Water	1000	$1.003 \times 10^{-3}$

### 4.1.4 Planar capillary wave

The capillary wave test case, initially introduced in Popinet and Zaleski (1999), is appropriate to the evaluation of the spatial and temporal accuracy of an interfacial curvature calculation method for the simulation of viscous, surface tension driven two-phase flows. For example, this benchmark has been used recently in Gerlach et al. (2006) and Popinet (2009). A similar test case is also used in Tubović and Jasak (2012).

Two fluids are initially at rest and the flat interface between the two phases is subject to a sinusoidal perturbation. The gravity acceleration is not considered, thus surface tension act as the only driving force. The interface will oscillate around its equilibrium position with an amplitude that will decay due to viscous dissipation. The solution to this initial value problem has been found by Prosperetti (1981) in the limit of vanishingly small amplitudes.

As in Popinet (2009), a two-dimensional computational domain of  $[-\lambda/2, \lambda/2] \times [-3\lambda/2, 3\lambda/2]$  is adopted so that the influence of the boundary conditions on the solution is negligible (the Prosperetti solution is valid for infinite domains). Here  $\lambda = 2\pi/K$  is the wavelength and  $K$  is the wavenumber. The initial perturbation amplitude is  $\lambda/100$  as in Popinet and Zaleski (1999), Gerlach et al. (2006) and Popinet (2009). Air and water are considered with properties summarized in Table 4.3. The Laplace number relative to the water phase ( $\text{La} = \rho\sigma\lambda/\mu^2$ ) is chosen equal to 3000 as in Popinet (2009). The normal-mode oscillation frequency  $\omega_0$  is given by the dispersion relation

$$\omega_0^2 = \frac{\sigma K^3}{\rho_1 + \rho_2}. \quad (4.10)$$

The duration of the simulation is set to  $25/\omega_0$  and we define the dimensionless time as  $\tau = t\omega_0$ . The  $L_2$  error norm, giving an evaluation of the error between the numerical and theoretical solutions, is calculated as

$$L_2(h) = \frac{100}{\lambda} \sqrt{\frac{\omega_0}{25} \int_{\tau=0}^{\tau=25} (h - h_{\text{exact}})^2}. \quad (4.11)$$

The results in terms of the  $L_2$  error norm are summarized in Table 4.4 for different mesh resolutions. The accuracy of the *Gauss* and *node-based gradient* methods is relatively equivalent with a convergence of the results toward the analytical solution. The *recursive weighted interpolations* method is the less accurate in this case. This is most probably due to the smoothing of the interface unit normal vectors and interfacial curvature. On the other hand, the *height function* method presents similar results at the lowest resolution, however its convergence rate is higher, resulting in more accurate results at higher mesh resolutions.

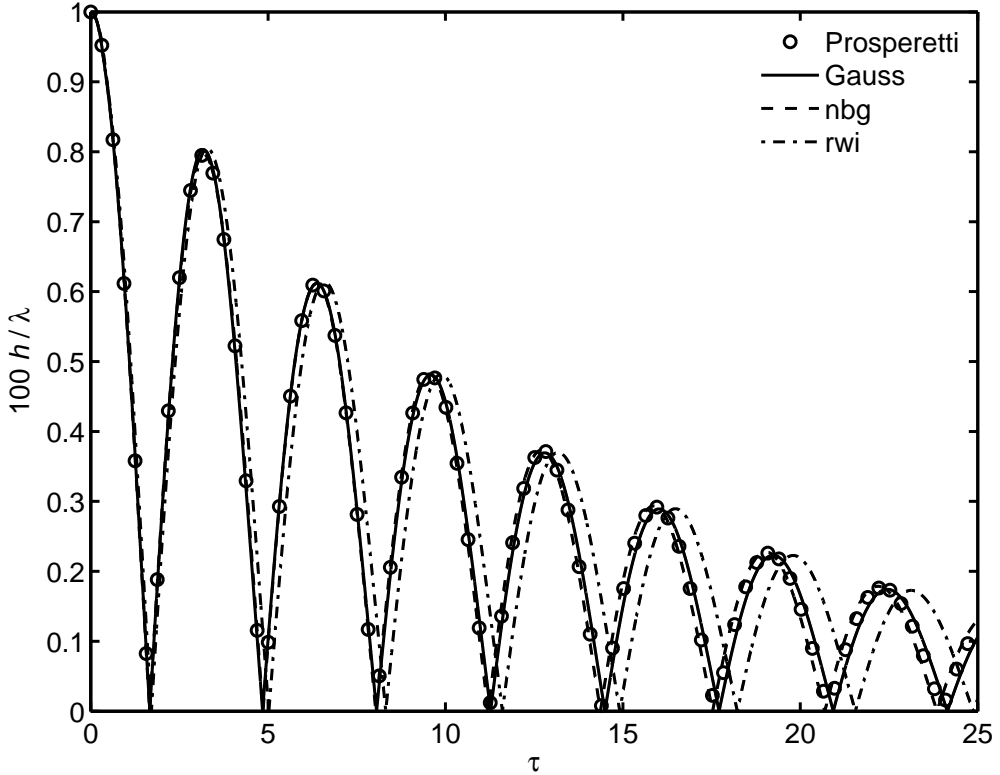


**Figure 4.6:** Time history of the relative amplitude of an air-water capillary wave ( $\text{La} = 3000$ ). The mesh resolution is  $128 \times 384$ .

**Table 4.4:** Convergence of the  $L_2$  error norm for the air-water capillary wave test case.

Method/resolution	8	16	32	64	128
Gauss	0.2073	0.0924	0.0210	0.0156	0.0134
nbg	0.1956	0.1020	0.0431	0.0143	0.0104
rwi	0.2072	0.1712	0.1287	0.1081	0.0845
hf (Popinet, 2009)	0.1971	0.0754	0.0159	0.00576	0.00313

Figure 4.6 shows the time evolution of the relative amplitude of the capillary wave for the finest mesh resolution. The results of the *height function* method are not displayed for clarity. It can be observed that the damping of the relative amplitude of the capillary wave is correctly reproduced by all the methods. However, discrepancies are observed regarding the frequency of the oscillations. The *Gauss* method slightly under-estimate it while the *node-based gradient* slightly over-estimate it. On the other hand, the frequency obtained with the *recursive weighted interpolations* method is highly under-estimated with respect to the other methods. This means that this method has a less accurate temporal accuracy and may not be suitable for cases where the evolution of a deformed two-phase interface is of interest. The method may be more appropriate to cases where the stability of the solution is preferred, which is the case of the simulations performed in this thesis.

## 4.2 Phase change model

In order to validate the phase change model, the typical one-dimensional benchmarks (Stefan problem and sucking interface problem) are firstly performed. Then the more challenging test case of the spherical vapor bubble growth in superheated liquid is performed in three-dimensions.

### 4.2.1 One-dimensional Stefan problem

The one-dimensional Stefan problem considered in Welch and Wilson (2000) is investigated with the heat and mass transfer model proposed in this thesis. Water properties at saturation pressure of 1 atm are considered (see Table 4.5). Liquid and vapor are assumed incompressible and initially at rest. In this Stefan problem, the liquid initially fill the computational domain at saturation temperature and a thin layer of vapor is considered attached to the left solid boundary, which is at a higher temperature than saturation. The vapor experiences an increase in temperature and a temperature gradient forms at the interface which drives the mass transfer from the liquid phase to the vapor phase (see Figure 4.7). In this condition, the vapor is motionless and the liquid is pushed away from the solid boundary. The interface is also pushed toward the right boundary, with a different velocity with respect to the liquid phase. This test case permits to estimate the accuracy of the diffusion term in the energy equation, which governs the rate of mass transfer since heat is provided from the left wall by diffusion into the motionless vapor phase.

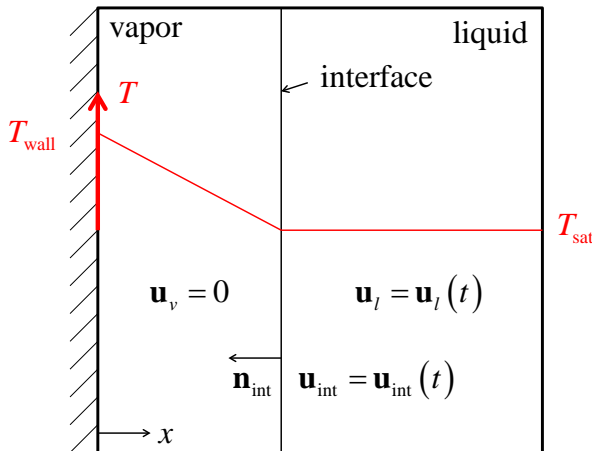


**Figure 4.7:** Domain definition for the Stefan problem.

**Table 4.5:** Water properties at saturation pressure of 1 atm ( $T_{\text{sat}} = 373.15$  K).

Phase	$\rho$ [kg/m <sup>3</sup> ]	$\mu$ [kg/(m s)]	$c_p$ [J/(kg K)]	$\lambda$ [W/(m K)]
Vapor	0.6	$1.23 \times 10^{-5}$	2080	0.025
Liquid	958	$2.82 \times 10^{-4}$	4216	0.68

## Chapter 4. Verification and validation of the method

---

**Table 4.6:** Mesh resolutions and results for the Stefan problem.

Resolution	Elements	$\Delta x [\mu\text{m}]$	$x_{\text{int}}(t = 0.1\text{s}) [\mu\text{m}]$	Error $x_{\text{int}} [\%]$
Coarse	64	15.625	201.2	4.79
Intermediate	128	7.8125	196.9	2.55
Fine	256	3.90625	194.4	1.25

$$\text{Error } x_{\text{int}} [\%] = 100 [x_{\text{int}} - (x_{\text{int}})_{\text{analytical}}] / (x_{\text{int}})_{\text{analytical}};$$

The solution of this one-dimensional Stefan problem given in Welch and Wilson (2000) is considered. The evolution of the interface position follows

$$x_{\text{int}} = 2\gamma\sqrt{\alpha_v t}, \quad (4.12)$$

where  $\alpha_v = \lambda_v / (\rho_v c_{p,v})$  is the thermal diffusivity of the vapor phase and  $\gamma$  is the solution of the transcendental equation

$$\gamma \exp(\gamma^2) \operatorname{erf}(\gamma) = \frac{c_{p,v} (T_{\text{wall}} - T_{\text{sat}})}{h_{lv} \sqrt{\pi}}, \quad (4.13)$$

with  $\operatorname{erf}(x)$  the error function and  $h_{lv} = 2256 \text{ kJ/kg}$  the latent heat of vaporization. The evolution of the temperature profile is given as

$$T(x, t) = T_{\text{wall}} + \left( \frac{T_{\text{sat}} - T_{\text{wall}}}{\operatorname{erf}(\gamma)} \right) \operatorname{erf}\left(\frac{x}{2\sqrt{\alpha_v t}}\right), \quad (4.14)$$

Three grid spacing  $\Delta x$  are analyzed (see Table 4.6) with a wall temperature of 10 K higher than the saturation temperature. The length of the domain is set to 1 mm. The liquid-vapor interface is initially positioned at  $x_{\text{int}} = 31.25 \mu\text{m}$ , corresponding to an initial time of 2.7 ms. The temperature in the vapor phase is initialized using the analytical solution at  $t = 2.7 \text{ ms}$ . The simulation is run until the time  $t = 0.1 \text{ s}$  is reached. The corresponding analytical solution is  $(x_{\text{int}})_{\text{analytical}} = 192 \mu\text{m}$  and a linear temperature profile from the left wall to the interface.

The results of the simulations in terms of final interface position are summarized in Table 4.6, while the time histories of the interface position are displayed in Figure 4.8. A good accuracy is obtained with a relative error contained within 5% of the analytical solution for all the mesh resolutions. The treatment of the diffusion term using the implemented method is therefore enough accurate. Note that if the discretization of the diffusion term does not account for the interface temperature, i.e., if the Ghost Fluid Method is not employed, the error in the results increases, leading to the necessity of much finer mesh elements to obtain the same degree of accuracy. The solution may also not converge toward the theoretical one.

### 4.2.2 One-dimensional sucking interface problem

The one-dimensional sucking interface problem considered in Welch and Wilson (2000) is also investigated with the heat and mass transfer model proposed in this thesis. Water properties at saturation pressure of 1 atm are considered (see Table 4.5). Liquid and vapor are assumed incompressible and initially at rest. This is another kind of Stefan

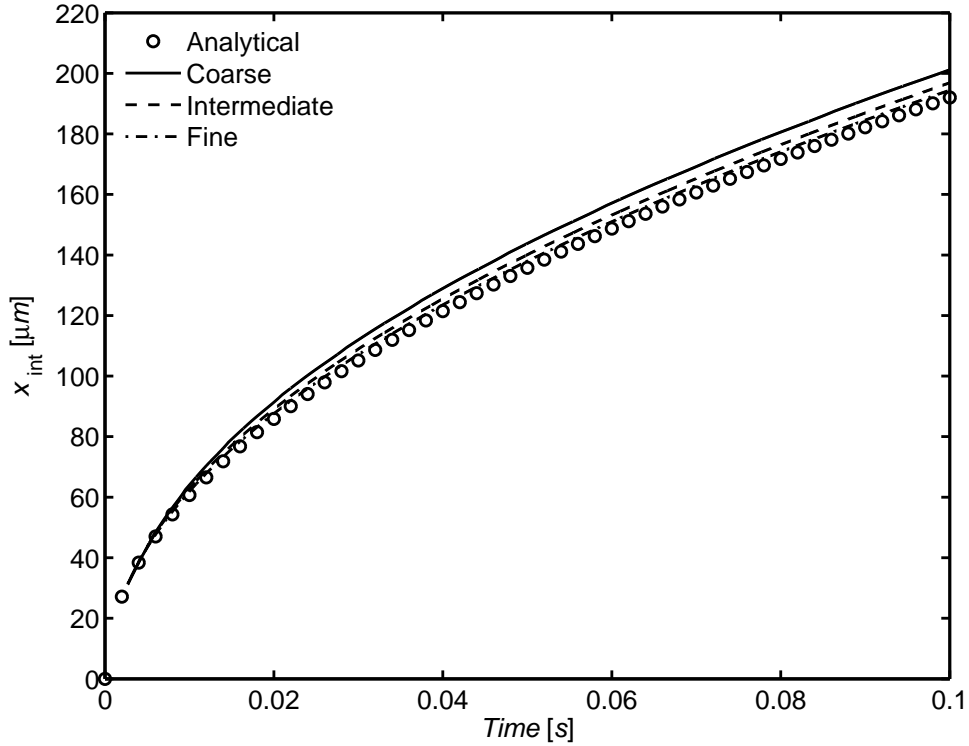


**Figure 4.8:** Time evolution of the interface position for the Stefan problem.

problem, in which the liquid initially fill the computational domain and is superheated. The temperature of the left wall is fixed at the saturation temperature thus the heat absorbed through evaporation comes from the liquid only. An infinitely thin vapor layer is located at the left wall, triggering the mass transfer between the phases. In this situation, the vapor is motionless and the liquid and the interface are pushed away from the left wall. Since the liquid is moving, a thermal boundary layer forms near the interface and develops as the interface moves (see Figure 4.9). This test case is useful to determine the accuracy of the convection term.

In Welch and Wilson (2000), a similarity solution is given where an ODE equation needs to be solved. However, an analytical solution can be obtained from the problems presented in Carslaw and Jaeger (1959) and will be given here. Like previously, the evolution of the interface position follows

$$x_{\text{int}} = 2\gamma\sqrt{\alpha_v t}, \quad (4.15)$$

In the general case where  $T_{\text{wall}} \neq T_{\text{sat}}$ ,  $\gamma$  is the solution of the following transcendental equation

$$\exp(\gamma^2) \operatorname{erf}(\gamma) \left[ \gamma - \frac{(T_{\infty} - T_{\text{sat}}) c_{p,v} \lambda_l \sqrt{\alpha_v} \exp\left(-\gamma^2 \frac{\rho_v^2 \alpha_v}{\rho_l^2 \alpha_l}\right)}{h_{lv} \sqrt{\pi} \lambda_v \sqrt{\alpha_l} \operatorname{erfc}\left(\gamma \frac{\rho_v \sqrt{\alpha_v}}{\rho_l \sqrt{\alpha_l}}\right)} \right] \quad (4.16)$$

$$= \frac{c_{p,v} (T_{\text{wall}} - T_{\text{sat}})}{h_{lv} \sqrt{\pi}},$$

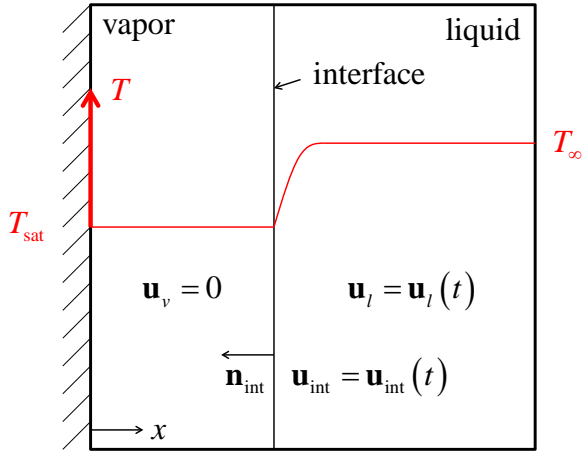


**Figure 4.9:** Domain definition for the sucking interface problem.

**Table 4.7:** Mesh resolutions and results for the sucking interface problem.

Resolution	Elements	$\Delta x [\mu\text{m}]$	$x_{\text{int}}(t = 1.1\text{s}) [\text{mm}]$	Error $x_{\text{int}} [\%]$
Coarse	64	156.25	6.945	-4.71
Intermediate	128	78.125	8.204	12.57
Fine	256	39.0625	7.883	8.16

$$\text{Error } x_{\text{int}} [\%] = 100 [x_{\text{int}} - (x_{\text{int}})_{\text{analytical}}] / (x_{\text{int}})_{\text{analytical}};$$

with  $\text{erfc}(x)$  the complementary error function and  $h_{lv} = 2256 \text{ kJ/kg}$  the latent heat of vaporization. The evolution of the temperature profile for the vapor phase is given as

$$T_v(x, t) = T_{\text{wall}} + \left( \frac{T_{\text{sat}} - T_{\text{wall}}}{\text{erf}(\gamma)} \right) \text{erf} \left( \frac{x}{2\sqrt{\alpha_v t}} \right), \quad (4.17)$$

while the evolution of the temperature profile for the liquid phase is given as

$$T_l(x, t) = T_{\infty} - \left( \frac{T_{\infty} - T_{\text{wall}}}{\text{erfc} \left( \gamma \frac{\rho_v \sqrt{\alpha_v}}{\rho_l \sqrt{\alpha_l}} \right)} \right) \text{erfc} \left( \frac{x}{2\sqrt{\alpha_l t}} + \frac{\gamma (\rho_v - \rho_l)}{\rho_l} \sqrt{\frac{\alpha_v}{\alpha_l}} \right). \quad (4.18)$$

Note that if  $T_{\infty} = T_{\text{sat}}$ , the solution corresponds to the previous Stefan problem.

Three grid spacing  $\Delta x$  are analyzed (see Table 4.7) with an initial liquid temperature of 5 K higher than the saturation temperature. The length of the domain is set to 10 mm. The liquid-vapor interface is initially positioned at  $x_{\text{int}} = 312.5 \mu\text{m}$ . Like in Welch and Wilson (2000), the temperature profile is initialized from the analytical solution at  $t = 0.1 \text{ s}$  and the simulation is run until the time  $t = 1.1 \text{ s}$  is reached. The corresponding analytical solution for the position of the interface is  $(x_{\text{int}})_{\text{analytical}} = 7.288 \text{ mm}$ .

The results in terms of final interface position, corrected to account for the different origin, are summarized in Table 4.7. The time evolutions of the interface position are displayed in Figure 4.10, while the instantaneous profiles of temperature are shown in

## 4.2. Phase change model

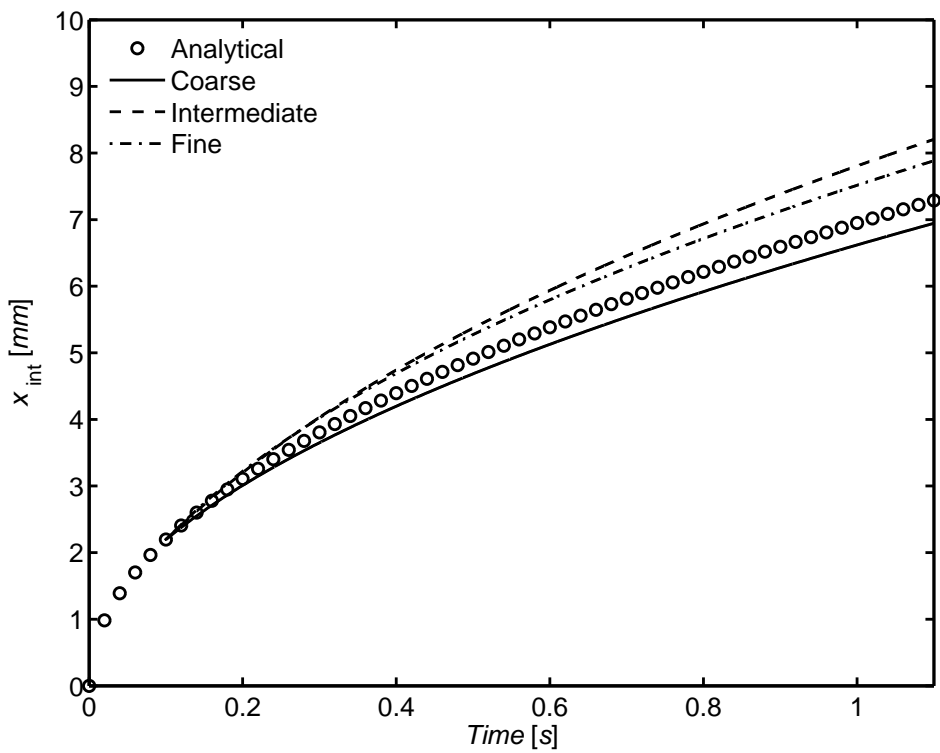


**Figure 4.10:** Time evolution of the interface position for the sucking interface problem.

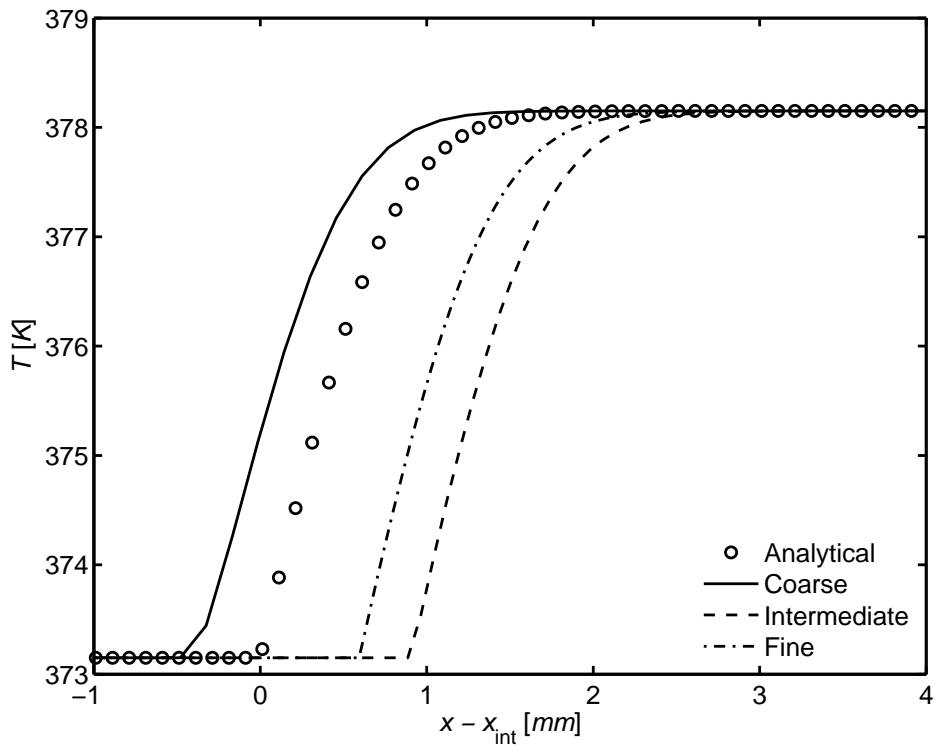


**Figure 4.11:** Temperature profiles at  $t = 1.1\text{s}$  for the sucking interface problem.

Figure 4.11. A higher dependency on the mesh resolution is observed compared to the previous problem. A non-linear evolution of the convergence with mesh refinement is also noticed, which may be caused by the convection term because it has not been modified to account for the interface temperature. Considering the mesh element sizes employed, the error is acceptable and below 10% for the fine mesh resolution. The thickness of the thermal boundary layer is also well reproduced. Since, the diffusion term seems to be well implemented according to the results of the previous test case, the convection term should be the most critical part of the model in this benchmark. A higher accuracy is therefore achievable by improving the discretization of the convection term and taking into account the temperature at the interface.

#### 4.2.3 Spherical vapor bubble growth

The growth of a spherical vapor bubble in a superheated liquid is considered here. This is a typical benchmark to assess the accuracy of phase change models in more than one dimension. It has been used by Son (2001), Kunkelmann and Stephan (2009), Kunkelmann and Stephan (2010b), Magnini et al. (2013a) and Sato and Ničeno (2013). The evaporation of a spherical bubble presents two different stages. In the first stage, the growth of the bubble is controlled by surface tension and inertia. In the second stage, the growth is controlled only by the rate at which heat can be transferred by diffusion and convection from the superheated liquid to the two-phase interface. A detailed description of each phase is provided in Plesset and Zwick (1954). Using the similarity approach, Scriven (1959) obtained an analytical solution for the second stage of the bubble growth. In a similar way to the sucking interface problem, the analytical solution will be used to initialize the simulations.

Due to the curvature of the interface, surface tension effects are present near the interface and are particularly significant when the radius of the bubble is small, as it has been observed in the static bubble test case. If the interfacial curvature calculation method is not enough accurate, strong spurious currents may appear near the interface and interact badly with the temperature field, leading to erroneous estimates of the mass transfer rate at the interface. In addition to surface tension effects, the interface unit normal vectors are no more aligned with the mesh thus introducing additional difficulties in estimating correctly the local mass transfer rate at the liquid-vapor interface. This test case is therefore useful to estimate the accuracy of the mass transfer calculation method and the interaction of the phase-change model with the surface tension model.

The analytical solution for the bubble radius,  $r_{\text{int}}(t)$ , is

$$r_{\text{int}}(t) = 2\beta_g \sqrt{\alpha_v t}, \quad (4.19)$$

where  $\beta_g$  is the “growth constant” obtained from

$$\begin{aligned} & 2\beta_g^2 \int_0^1 \exp \left( -\beta_g^2 \left( (1-\eta)^{-2} - 2 \left( 1 - \frac{\rho_v}{\rho_l} \right) \eta - 1 \right) \right) d\eta \\ &= \frac{\rho_l c_{p,l} (T_\infty - T_{\text{sat}})}{\rho_v (h_{lv} + (c_{p,l} - c_{p,v}) (T_\infty - T_{\text{sat}}))}. \end{aligned} \quad (4.20)$$

The vapor is at saturation temperature while the analytical solution for the liquid

## 4.2. Phase change model

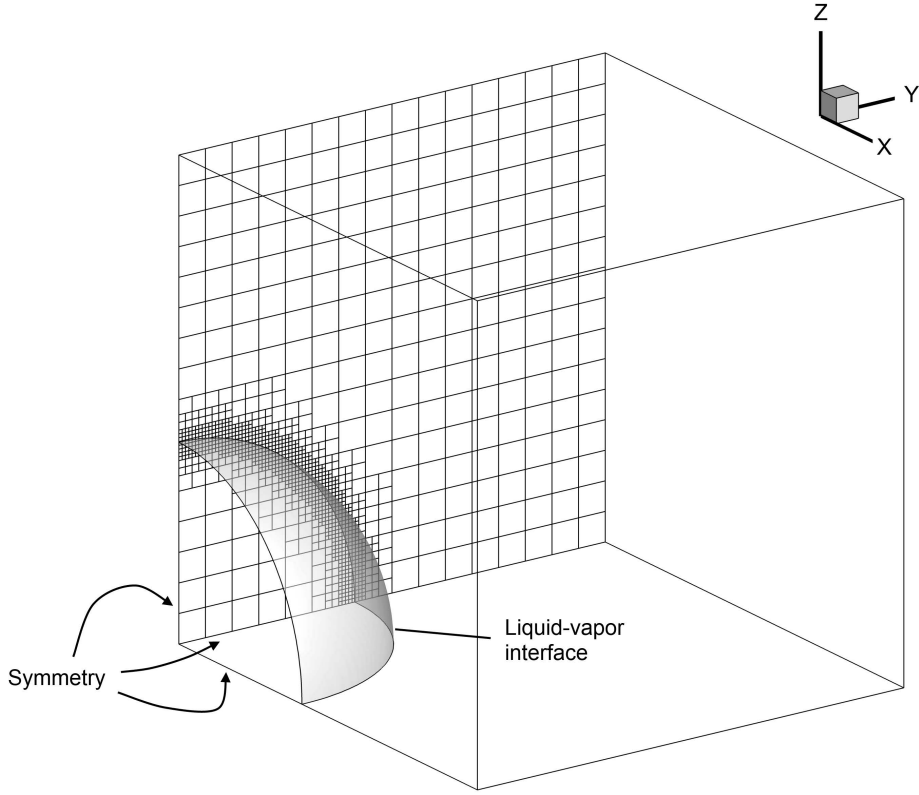


**Figure 4.12:** Domain definition for the spherical vapor bubble growth problem.

temperature is

$$T_l(r, t) = T_\infty - 2\beta_g^2 \left( \frac{\rho_v (h_{lv} + (c_{p,l} - c_{p,v}) (T_\infty - T_{\text{sat}}))}{\rho_l c_{p,l}} \right) \times \int_{1 - \frac{r_{\text{int}}(t)}{r}}^1 \exp \left( -\beta_g^2 \left( (1 - \eta)^{-2} - 2 \left( 1 - \frac{\rho_v}{\rho_l} \right) \eta - 1 \right) \right) d\eta. \quad (4.21)$$

A three-dimensional cubic computational domain of side 250  $\mu\text{m}$  is chosen for the simulations, in order to allow dynamic mesh refinement (in OpenFOAM this is only available in three-dimension). One-eighth of the bubble is simulated using symmetry boundary conditions for the left, bottom and back boundaries (see Figure 4.12). The mesh resolution is highest near the interface and is then progressively reduced to a maximum element size of 15.625  $\mu\text{m}$ . Three minimum mesh element sizes  $\Delta_{\min}$  are analyzed (see Table 4.8) with an initial liquid temperature of 5 K higher than the saturation temperature.

The simulation is initialized using the analytical solution at  $t = 0.07$  ms, corresponding to a bubble radius of 103.135  $\mu\text{m}$ . The simulation is run until the time  $t = 0.3$  ms is reached, corresponding to a bubble radius of 213.5  $\mu\text{m}$ .

The results in terms of final bubble radius are summarized in Table 4.8 while the time evolutions of the bubble radius are shown in Figure 4.13. Like in the previous test case, a high dependency on the mesh resolution is observed and the results may

## Chapter 4. Verification and validation of the method

---

**Table 4.8:** Mesh resolutions and results for the spherical vapor bubble growth problem.

Resolution	$\Delta_{\min}$ [ $\mu\text{m}$ ]	$r_{\text{int}}(t = 0.3\text{ms})$ [ $\mu\text{m}$ ]	Error $r_{\text{int}}$ [%]
Coarse	7.8125	161.6	-24.31
Intermediate	3.90625	194.7	-8.81
Fine	1.953125	217.9	2.06

$$\text{Error } r_{\text{int}} [\%] = 100 [r_{\text{int}} - (r_{\text{int}})_{\text{analytical}}] / (r_{\text{int}})_{\text{analytical}};$$

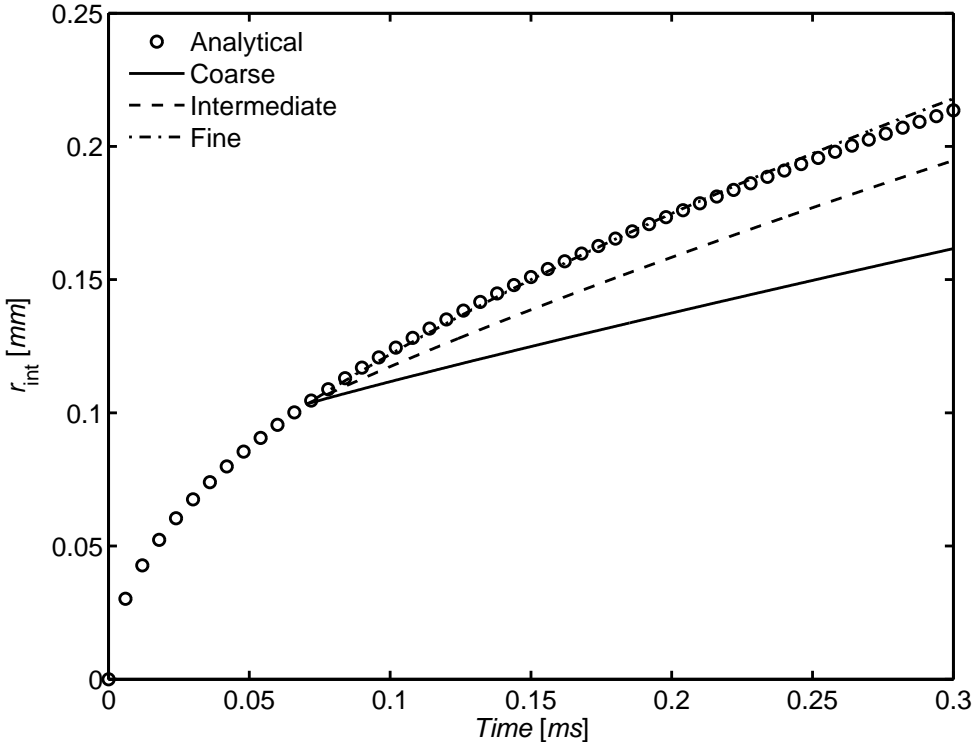


**Figure 4.13:** Time evolution of the interface position for the spherical vapor bubble growth problem.

not converge toward the analytical solution. The profiles of temperature at  $t = 0.3$  ms are also displayed in Figure 4.14. Despite the discrepancy of the bubble growth rate for the Coarse and Intermediate mesh resolutions, the thermal boundary layer are well reproduced for all the cases.

We note that the results may be drastically improved by modifying the discretization of the convection term as well as by improving the estimates of the mass transfer rate. For instance, the methods implemented in Sato and Ničeno (2013) may be more suitable. An improvement of the interfacial curvature calculation may also be benefit through the reduction of the spurious currents.

Despite these drawbacks, the implemented method is enough stable to be used as a starting point for the development of a more accurate model. In effect, some useful features are available such as dynamic mesh refinement capabilities and a sharp treatment of the mass transfer model. Preliminary investigations of boiling phenomena may also be performed.

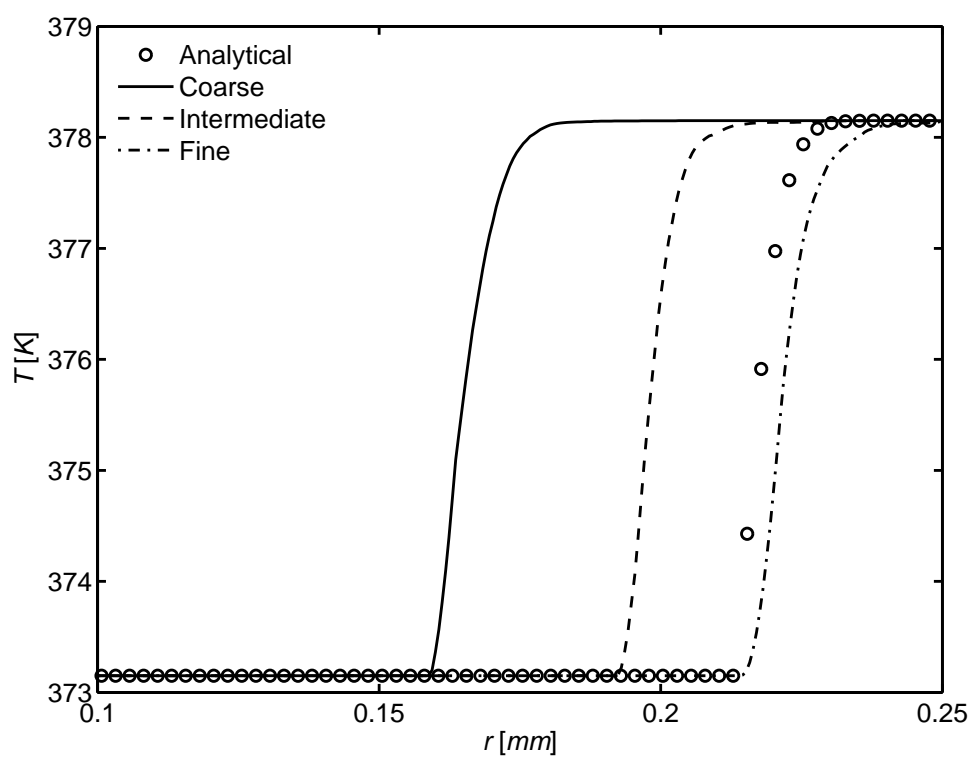


**Figure 4.14:** Temperature profiles at  $t = 0.3\text{ms}$  for the spherical vapor bubble growth problem.



---

# CHAPTER 5

---

## Results on isothermal spherical rising bubbles

---

In this chapter, the rise of isothermal spherical air bubbles in stagnant pure water is investigated using the various implemented interfacial curvature calculation methods. The performances of each method are therefore assessed on realistic cases. The dynamics of small spherical bubbles, which are subject to high surface tension forces, is also of fundamental importance for a number of industrial and natural processes. For instance, gas-liquid flows involving heat and mass transfer display such characteristics during bubble collapse and nucleation. Small bubbles are also employed to improve the efficiency of chemical reactors by increasing the surface area available for mass transfer.

To characterize the interaction forces between the liquid and the gas phases, several experimental studies have been performed in the past on single rising bubbles in stagnant liquids (Peebles and Garber, 1953; Clift et al., 1978; Bhaga and Weber, 1981; Duineveld, 1995; Zun and Groselj, 1996; Dai et al., 1998; Tomiyama et al., 2002; Parkinson et al., 2008; Sanada et al., 2008). Theoretical predictions have been proposed as well. For very small bubbles in the viscous dominant regime, i.e., when the bubble Reynolds number is less than unity ( $d_e \leq 100$  microns for an air-water system), Hadamard (1911) and Rybczynski (1911) proposed a drag law in which slip at the interface is considered. In practice this happens only in pure liquids, as verified by Parkinson et al. (2008) using ultra-pure and contaminated water for comparison. In effect, the presence of surfactants modifies the state of the gas-liquid interface in such a way that the bubble is comparable to a rigid sphere (Tomiyama et al., 2002; Parkinson et al., 2008; Dijkhuizen et al., 2010a). In this condition, the well known Stokes' drag law for solid particles can be used. When inertial forces cannot be neglected, i.e., when larger spherical bubbles are considered, the theoretical predictions of Moore (1963, 1965) agree very well with the experiments of Duineveld (1995) and Sanada

et al. (2008). For a more thorough overview of bubble formation and rise as well as drag correlations, the interested reader is referred to Kulkarni and Joshi (2005).

Despite the apparent simplicity of spherical bubbles, their detailed numerical simulation using an interface tracking technique is rather difficult. The main reason for this difficulty is often attributed to the presence of spurious currents around the interface originating from the treatment of the surface tension (Scardovelli and Zaleski, 1999). The so called static bubble test case is frequently chosen to analyze these spurious currents and several studies have been performed (see e.g., Scardovelli and Zaleski (1999); Popinet and Zaleski (1999); Renardy and Renardy (2002); Francois et al. (2006); Gerlach et al. (2006); Popinet (2009); Nichita et al. (2010); Magnini and Pulvirenti (2011); Magnini et al. (2013a)). When the fluids have high density and viscosity ratios, for instance an air-water system, numerical instabilities also readily appear. As a consequence, the first numerical study on rising air bubbles in stagnant water with diameters down to 1 mm was only recently carried out, by Dijkhuizen et al. (2005). They used a Front Tracking (FT) technique with proper modifications in order to simulate small bubbles. Later, Hua et al. (2008) also proposed a modified FT technique able to simulate air bubbles in water with diameters down to 500 microns. The model developed in Dijkhuizen et al. (2005) has been further improved and FT simulations of rising bubbles with diameters down to 300 microns have been successfully performed by Dijkhuizen et al. (2010a,b,c).

---

## 5.1 Reference data

---

A gas bubble released in a stagnant liquid will rise under the effect of buoyancy. After an initial transient, the velocity of the rising bubble will reach an asymptotic value defined as the terminal rise velocity, which is characteristic of the phenomenon. Many different sizes and shapes of bubbles are observed at different regimes, which can be defined by using two dimensionless groups, the Morton ( $Mo = \mu_l^4 g \rho_l^{-1} \sigma^{-3}$ ) and Eötvös ( $Eo = \rho_l g d_e^2 \sigma^{-1}$ ) (or Bond) numbers, from which the bubble Reynolds number ( $Re$ ) can be determined, as shown in Figure 5.1. The Reynolds, Morton, and Eötvös numbers capture the effects of the inertial, viscous, gravitational, and surface tension forces, which determine the bubbles' shapes, sizes, and characteristic terminal rise velocities. Additional dimensionless parameters affecting the physics of the problem are the density and viscosity ratios.

The choice of the operating fluids and gravitational acceleration determine the Morton number (for the air-water system at ambient conditions,  $Mo = 2.54 \times 10^{-11}$ , i.e.,  $\log Mo = -10.6$ ). The size of the bubble then defines the Eötvös number, from which an estimate of the shape and terminal rise velocity can be obtained. According to Figure 5.1, at low Eo numbers, spherical bubbles are observed, followed by ellipsoidal, spherical-cap, and skirted spherical-cap bubbles at increasing Eo numbers. An oscillatory (wobbling) behavior is observed at high Re numbers and, depending on the nature of the flow, also in the bubble wake (Fan and Tsuehiya, 1990).

Several authors (Fan and Tsuehiya, 1990; Haberman and Morton, 1954; Wu and Gharib, 1998) have studied the influence of vortex shedding on the shape and behavior of the bubble. Indeed, the recirculation and the wake at the bottom of the bubble can generate non-rectilinear trajectories with a full three-dimensional dynamics at large Re

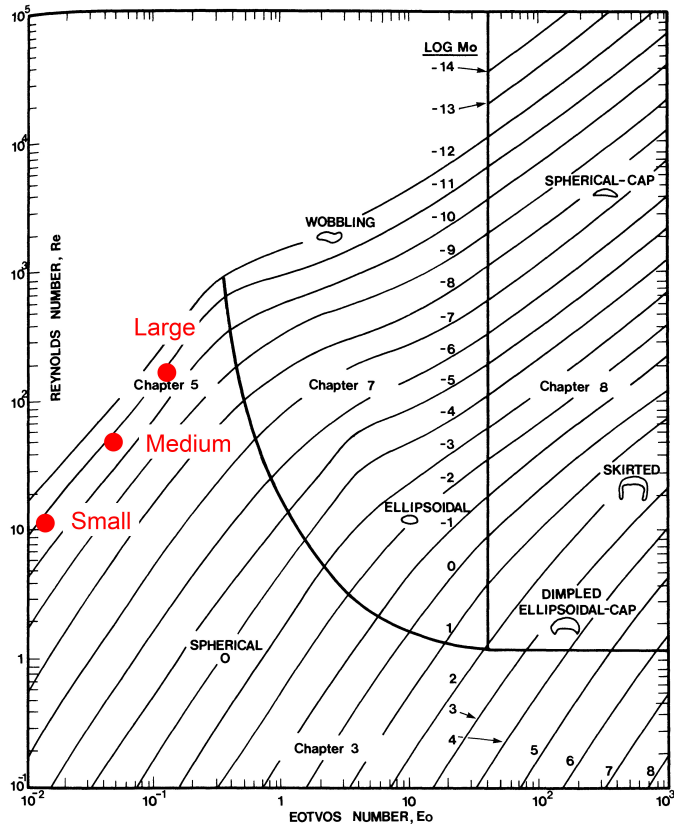


**Figure 5.1:** Shape regimes for bubbles rising in stagnant liquids (Clift et al., 1978).

numbers. Studying the behavior of rising air bubbles in clean water, Wu and Gharib (1998) found for a spherical bubble a transition from a rectilinear to a zig-zag motion at  $Re = 157 \pm 10$ , while for an ellipsoidal bubble, the transition is observed at  $Re = 564$ . Bhaga and Weber (1981) studied air bubbles rising in water-sugar solutions of different concentrations ( $Mo > 4 \times 10^{-3}$ , i.e.,  $\log Mo > -2.4$ ) and have observed closed and symmetric streamlines in the wake following the bubbles at  $Re < 110$ .

Figure 5.2 shows Clift's map (left) and a map from Tomiyama (2004) (right), linking the equivalent diameter, the  $Eo$  number, and the terminal rise velocity for both clean and contaminated water. In both diagrams, a bifurcation of the measured terminal rise velocities for bubble diameters greater than about 0.6 mm can be observed. This phenomenon was initially attributed to the presence of surfactants (Clift et al., 1978). Recently, some authors (Wu and Gharib, 1998; Tomiyama et al., 2002) have concluded that the initial bubble shape has the greatest influence. As pointed out by Tomiyama (2004) (Figure 5.2, right), a higher velocity and a low aspect ratio  $E$  (Tomiyama et al., 2002) are observed for bubbles with a high initial shape deformation. In addition, such bubbles follow a rectilinear path until a critical bubble Reynolds number of about 400 is reached. Yang et al. (2003) carried out a sensitivity analysis of the terminal rise velocity of bubbles undergoing shape or volume oscillations, reporting results in disagreement with this theory. Alves et al. (2005) studied bubbles kept stationary in a downward liquid flow and observed a reduction in the terminal rise velocity when the bubble surface is contaminated. Actually, the discussion about the causes of this

## Chapter 5. Results on isothermal spherical rising bubbles

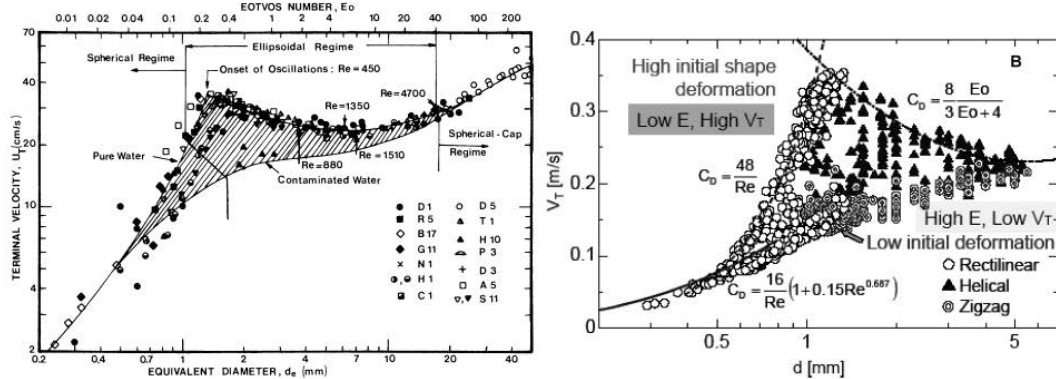


**Figure 5.2:** Terminal rise velocity of air bubbles in water at 20°C by Clift et al. (1978), left, and Tomiyama (2004), right.

significant variation of velocity is still open (Tomiyama, 2004; Celata et al., 2006).

In the present study, the numerical results are compared with the experimental data and the theoretical models based on the assumption of clean water (i.e., no contaminants affecting the bubble surface properties) and assuming limited deviations from a spherical shape (i.e., an aspect ratio  $E \approx 1$ ). For bubbles with  $0.4 < d_e < 1.1$  mm, the experimental data obtained by Dai et al. (1998), Duineveld (1995), and Sanada et al. (2008) are available. They show good agreement with the values of the drag coefficient and terminal rise velocity obtained analytically by Moore (1965). The Moore's terminal rise velocity,  $U_{\text{Moore}}^\infty$ , can be obtained starting from the expressions of the drag coefficient  $C_D$  given by the balance between the buoyancy and the drag forces acting on a spherical bubble,

$$C_D = \frac{4gd_e}{3(U^\infty)^2}, \quad (5.1)$$

and that theoretically derived by Moore (1965) in a generalized form for ellipsoidal bubble,

$$C_D = \frac{48G(E)}{\text{Re}} \left[ 1 + \frac{H(E)}{\text{Re}^{1/2}} + \dots \right], \quad (5.2)$$

with  $G(E)$  and  $H(E)$  functions of the bubble aspect ratio  $E$ ,

$$G(E) = \frac{E^{4/3} (E^2 - 1)^{4/3} \left[ (E^2 - 1)^{1/2} - (2 - E^2) \sec^{-1} E \right]}{3 \left( E^2 \sec^{-1} E - (E^2 - 1)^{1/2} \right)^2}, \quad (5.3)$$

$$H(E) = 0.0108E^4 - 0.157E^3 + 1.5725E^2 - 2.0195E - 1.67. \quad (5.4)$$

Merging the expressions reported for  $C_D$  (Eq. (5.1) and Eq. (5.2)) the following equation for  $U^\infty$  is obtained,

$$U^\infty \left[ 1 + \frac{H(E)}{\text{Re}^{1/2}} \right] = \frac{d_e^2 g \rho_l}{36 \mu_l G(E)}. \quad (5.5)$$

### 5.1. Reference data

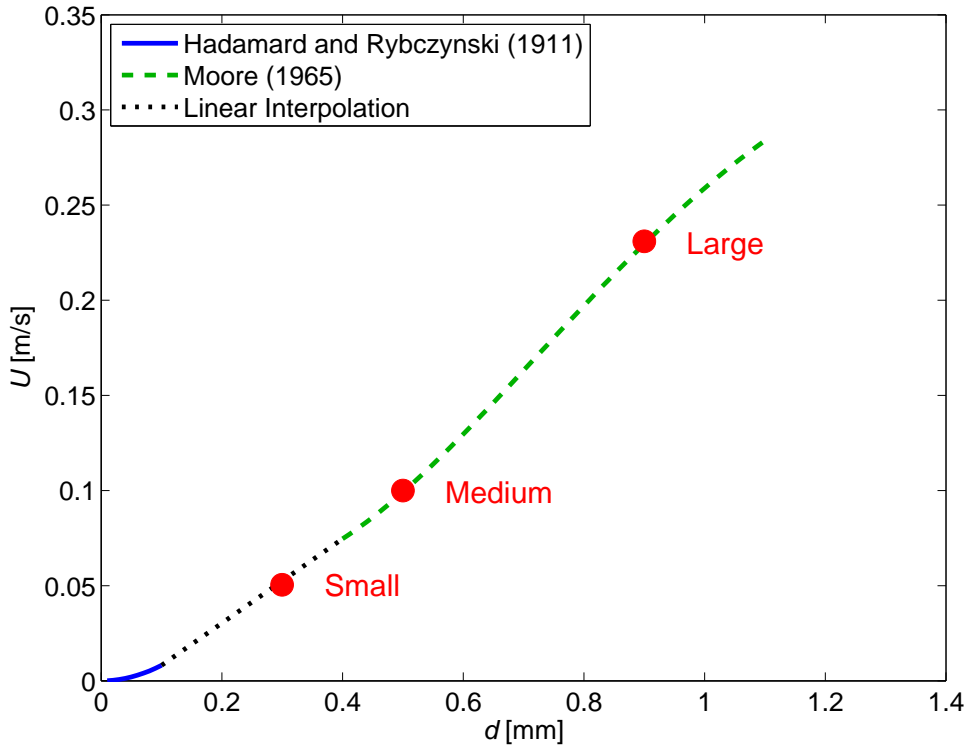


**Figure 5.3:** Analytical terminal rise velocity values for air bubble in water at 20°C.

This can be closed by using the approximated expression of the bubble Weber number ( $We = \rho_l(U^\infty)^2 d_e \sigma^{-1}$ ) in function of  $E$  given by Moore (1965),

$$We(E) = \frac{4(E^3 + E - 2) \left[ E^2 \sec E - (E^2 - 1)^{1/2} \right]^2}{E^{4/3} (E^2 - 1)^3}. \quad (5.6)$$

The Moore's terminal rise velocity,  $U_{\text{Moore}}^\infty$ , is defined by iterative calculation until both Eq. (5.5) and Eq. (5.6) are satisfied, as shown in Duineveld (1995).

For diameters  $d_e < 0.1$  mm, the experimental data by Parkinson et al. (2008) show good agreement for a single air bubble rising in clean water with Hadamard's and Rybczynski's solution ( $U_{H-R}^\infty$ ) (Hadamard, 1911; Rybczynski, 1911),

$$U_{H-R}^\infty = \frac{(d_e/2)^2 \Delta \rho g}{3 \mu_l}, \quad (5.7)$$

with  $\mu_g \ll \mu_l$  and  $\Delta \rho = \rho_l - \rho_g$ .

Figure 5.3 shows Moore's theory (Moore, 1965) for larger diameters and Hadamard's and Rybczynski's solution (Hadamard, 1911; Rybczynski, 1911) for smaller diameters. For the comparative study of interface curvature calculation methods, three bubble size scenarios are chosen and are indicated as "Large," "Medium" and "Small" (see Figure 5.1 and Figure 5.3). Liquid water ( $\rho_l = 1000 \text{ kg m}^{-3}$ ;  $\mu_l = 10^{-3} \text{ Pa s}$ ) and air ( $\rho_g = 1.225 \text{ kg m}^{-3}$ ;  $\mu_g = 1.73 \times 10^{-5} \text{ Pa s}$ ) are used as working fluids, with a surface tension coefficient typical of ambient conditions ( $\sigma = 0.0728 \text{ N m}^{-1}$ ). In Table 5.1, the characteristic dimensions and terminal rise velocities calculated from Figure 5.3 for

## Chapter 5. Results on isothermal spherical rising bubbles

---

**Table 5.1:** Characteristics of the three scenarios chosen for the comparative study.

Case	$d_e$ (mm)	Eo	$U_{\text{ref}}^{\infty}$ (m s $^{-1}$ )	$\text{Re}(U_{\text{ref}}^{\infty})$
Large	0.9	0.109	0.23	207
Medium	0.5	0.034	0.10	50
Small	0.3	0.012	0.05	15

the three scenarios are reported, as well as the associated Eo and Re. For the Small bubble size, a linear interpolation is used to calculate the terminal rise velocity due to the absence of reference data.

## 5.2 Boundary conditions and initialization

---

The domain used for the simulations is determined using some criteria available in the literature. According to the sensitivity analyses realized by Harmathy (1960) and Hua and Lou (2007), a domain with a length of at least  $10d_e$  in the rising direction of the bubble is required to avoid the influence of the boundary conditions. Lebaigue et al. (2003) also suggested using a  $10d_e$  extension in all directions or, alternatively, using the semi-empirical relation

$$\frac{U^{\infty,\text{confined}}}{U^{\infty}} \approx 1 - \left( \frac{d_e}{D} \right)^2, \quad (5.8)$$

with  $D$  the characteristic dimension of the domain in a plane perpendicular to the gravity direction. According to the work of Harmathy (1960), this approach captures the influence on the terminal rise velocity whereas the shape of the bubble is not affected by the domain extension.

The limited Reynolds numbers (see Table 5.1) in the scenarios analyzed here ensure a rectilinear trajectory of the rising bubble without any oscillation, as suggested by the experiments performed by Tomiyama (2004). An axisymmetric formulation is therefore adopted in order to simplify the problem. The domain extension, expressed in terms of the bubble initial diameter  $d_e$ , is thus  $18d_e$  along the  $z$ -direction, i.e., the revolution axis, and  $6d_e$  along the  $r$ -direction, i.e., the direction perpendicular to gravity. The extension in the  $r$ -direction guarantees that the boundary condition affects the final terminal rise velocity by less than 1%, according to Eq. (5.8).

Various mesh sizes  $\Delta$  are analyzed to assess the grid independence of the results. The sensitivity analysis performed by Hua and Lou (2007) shows that a mesh resolution of  $d_e/\Delta > 20$  ensures grid independence. A uniform mesh sizing method is adopted where the mesh is adapted statically to the desired resolution in a band of width  $1.5d_e$ . In the outer regions, the mesh becomes gradually coarser, since no characteristic phenomena and low velocities are expected there.

Table 5.2 summarizes the decreasing mesh sizes (“Coarse”, “Intermediate” and “Fine”) used within the simulations and Figure 5.4 gives an overview of the domain and boundary conditions.

A constant value for the pressure is applied at the upper boundary of the rectangular domain, axisymmetric conditions at the left boundary, and free slip conditions at the

## 5.2. Boundary conditions and initialization

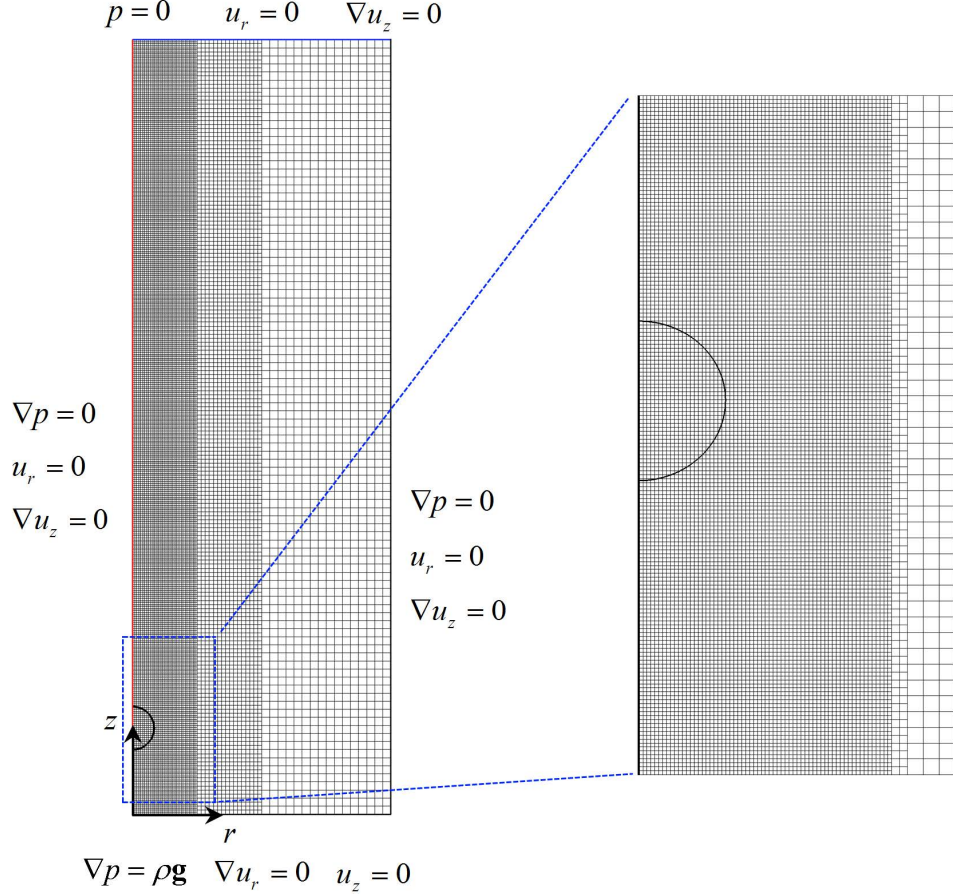


**Figure 5.4:** Overview of the domain extension, boundary conditions and meshing strategies.

**Table 5.2:** Summary of the mesh element sizes.

Resolution	$\max(d_e/\Delta)$	$\min(d_e/\Delta)$
Coarse	20	5
Intermediate	40	5
Fine	80	5

right and bottom boundaries. Zero normal gradient boundary condition is applied for the volume fraction  $F$  at all boundaries. Null velocity and pressure fields are set as initial conditions and the bubble is initially centered at  $(0, 2d_e)$ . For the first three interfacial curvature calculation methods, implemented in OpenFOAM, the volume fraction is initialized as follows

$$F = \max \left[ \min \left( 1 - \frac{|\mathbf{x} - (0, 2d_e)| - d_e/2 + \Delta}{2\Delta}, 1 \right), 0 \right], \quad (5.9)$$

while for the *height function* method, implemented in the Gerris code, the bubble is initialized using the intersection of the analytical bubble shape with the edges of the mesh.

## Chapter 5. Results on isothermal spherical rising bubbles

---

The time step size is restricted by the stability criteria for the convection, viscous and surface tension terms, like in the static bubble test case.

### 5.3 Results

---

In this section, the numerical results obtained with the four interfacial curvature calculation methods presented in the previous section are compared. The terminal rise velocity of the bubbles and the velocity field are mainly discussed.

#### 5.3.1 Calculation of the terminal rise velocity

The terminal velocity of a bubble can be determined either

- by evaluating the speed of the center of mass of the bubble  $z_m$ ; or
- by identifying a specific point on the interface, such as the apex ( $z_{max}$ ), and then calculating its rising speed.

The center of mass of the bubble is computed by

$$z_m = \frac{\sum z F V_{cell}}{\sum F V_{cell}}, \quad (5.10)$$

with  $z$  the cell-center position in the rise direction,  $F$  the volume fraction of the gaseous phase and  $V_{cell}$  the cell volume.

In cases with large bubble shape deformations, the “center-of-mass” approach is commonly used for capturing the acceleration–deceleration behavior observed before reaching the asymptotic terminal velocity (Lebaigue et al., 2003). However the “center-of-mass” approach is limited in the cases where break-up of the bubble, i.e., loss of mass, is observed. On the other hand, the “apex” approach is not affected by bubble break-up, however it is not able to capture the acceleration–deceleration behavior of bubbles with large shape deformations. In the cases studied here, the bubbles possess a spherical or quasi-spherical shape and an axisymmetric flow field, i.e., there are no large bubble deformations or break-ups. As a result, the “center-of-mass” approach is adopted for the computation of the terminal rise velocity.

#### 5.3.2 Grid convergence analysis

The results in terms of the terminal rise velocity obtained with the selected bubble diameters (Large, Medium and Small) for the Coarse, Intermediate, and Fine meshes are reported in Tables 5.3 and 5.4 for the four interfacial curvature calculation methods. Regarding the *Gauss* method, inaccurate results are obtained for all the bubble diameters and mesh resolutions. In particular, for the Medium and Small bubble diameters, the bubble is almost not rising. For the *node-based gradient* and *recursive weighted interpolations* methods, a relatively high dependency on the mesh resolution is observed, with the results not converging toward the reference solution. For the Large bubble diameter, the results accuracy are acceptable, while for the other two cases the results are mostly above 30% of relative error. On the other hand, the *height function* method demonstrates to be very accurate for all the three cases, with relative errors contained within 10%.

### 5.3. Results

**Table 5.3:** Simulated terminal rise velocities compared with reference data (see Section 5.1). Large and Medium cases.

Case	$U_{\text{ref}}^{\infty}$ (m s $^{-1}$ )	Method	Mesh	$U^{\infty}$ (m s $^{-1}$ )	Error (%)
Large	0.23	Gauss	Coarse	0.102	55.7
			Intermediate	0.111	51.5
			Fine	0.115	49.8
	nbg		Coarse	0.247	7.2
			Intermediate	0.243	5.6
			Fine	0.260	13.1
	rwi		Coarse	0.207	10.0
			Intermediate	0.173	24.9
			Fine	0.150	34.6
Medium	0.10	Gauss	Coarse	0.000	100
			Intermediate	0.028	71.8
			Fine	0.0544	45.6
	nbg		Coarse	0.162	61.9
			Intermediate	0.145	45.1
			Fine	0.156	55.9
	rwi		Coarse	0.093	7.0
			Intermediate	0.090	9.8
			Fine	0.044	55.9
hf			Coarse	0.089	10.8
			Intermediate	0.098	2.3
			Fine	0.094	5.7

$$\text{Error} (\%) = 100 |U^{\infty} - U_{\text{ref}}^{\infty}| / U_{\text{ref}}^{\infty};$$

#### 5.3.3 Characterization of the bubble rise

The time evolution of the bubble rise velocity for the three methods implemented in OpenFOAM are displayed in Figures 5.5, 5.6 and 5.7 for the case Large, Medium and Small, respectively, and for the Coarse mesh resolution. The results for the *height function* method are shown in Figures 5.8, 5.9 and 5.10. As shown in these figures, the initial phase of the rise is characterized by an acceleration until the steady-state terminal rise velocity is reached.

## Chapter 5. Results on isothermal spherical rising bubbles

---

**Table 5.4:** Simulated terminal rise velocities compared with reference data (see Section 5.1). Small case.

Case	$U_{\text{ref}}^{\infty}$ (m s <sup>-1</sup> )	Method	Mesh	$U^{\infty}$ (m s <sup>-1</sup> )	Error (%)
Small	0.05	Gauss	Coarse	0.000	100
			Intermediate	0.002	96.9
			Fine	0.000	100
	nbg	Coarse	0.108	115.8	
			Intermediate	0.076	52.7
			Fine	0.080	59.5
	rwi	Coarse	0.077	53.8	
			Intermediate	0.070	39.6
			Fine	0.040	20.7
hf	0.05	Coarse	0.046	8.0	
			Intermediate	0.049	2.6
			Fine	0.045	10.0

$$\text{Error} (\%) = 100|U^{\infty} - U_{\text{ref}}^{\infty}|/U_{\text{ref}}^{\infty};$$

Regarding the methods implemented in OpenFOAM, the quality of the results decreases as the bubble diameter is reduced, explained by the higher capillary forces due to the increasing interfacial curvature. The bubble is also not able to rise when the *Gauss* method is employed for the Medium and Small bubble diameters, as shown in Figures 5.6 and 5.7. In these cases, the bubble oscillates around its initial position. Concerning the *recursive weighted interpolations* method, a non-physical trend of the rising velocity is observed for the Medium and Small bubble diameters while the trend is of good quality for the Large case. On the other hand, the results obtained with the *node-based gradient* method are physical for all the three bubble diameters, however the rising velocity is overestimated. The results for the Intermediate and Fine mesh resolutions are not displayed for the sake of clarity, however similar trends are obtained, with a different terminal rise velocity.

The evolutions of the rising velocity in the simulations using the *height function* method present the most physical trends, with a converging behavior while the mesh resolution is increased. In the case Large (see Figure 5.8), the Coarse mesh presents a lower initial acceleration which leads to an underestimate of the terminal rise velocity, that is reached approximately at the same instant from all the tested meshes. This trend does not persist for the Medium and Small cases where a different behavior, characterized by a higher initial acceleration, is observed for the Coarse mesh. A higher dependence of the acceleration phase on the spatial discretization is therefore noticed when the capillary forces increase, i.e., when the bubble size decreases, suggesting the use of finer meshes for smaller bubble dimensions.

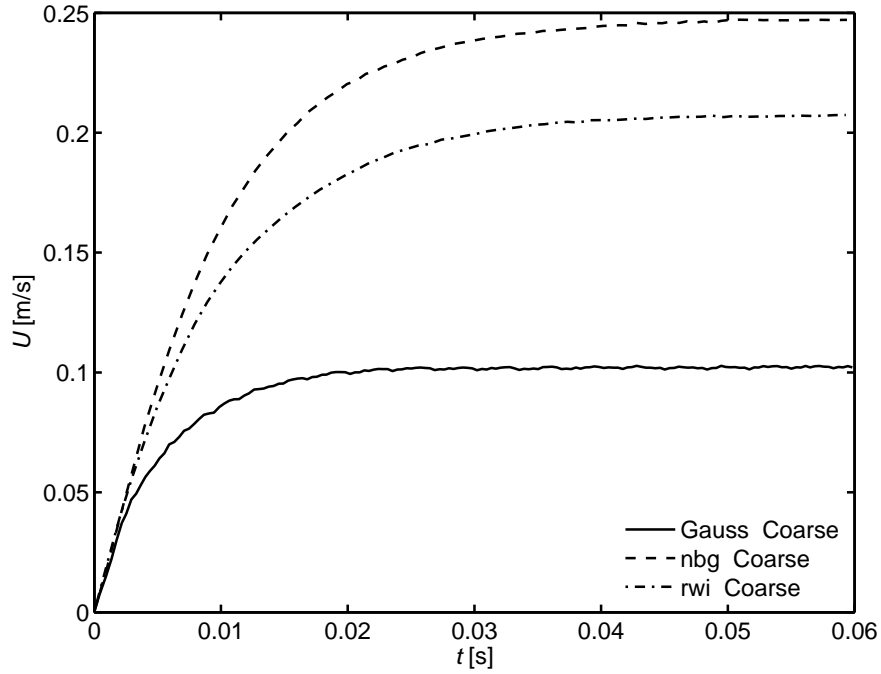


**Figure 5.5:** Bubble rise velocity history for the case Large ( $d_e = 0.9$  mm). Results from the Gauss, nbg and rwi methods (OpenFOAM code).

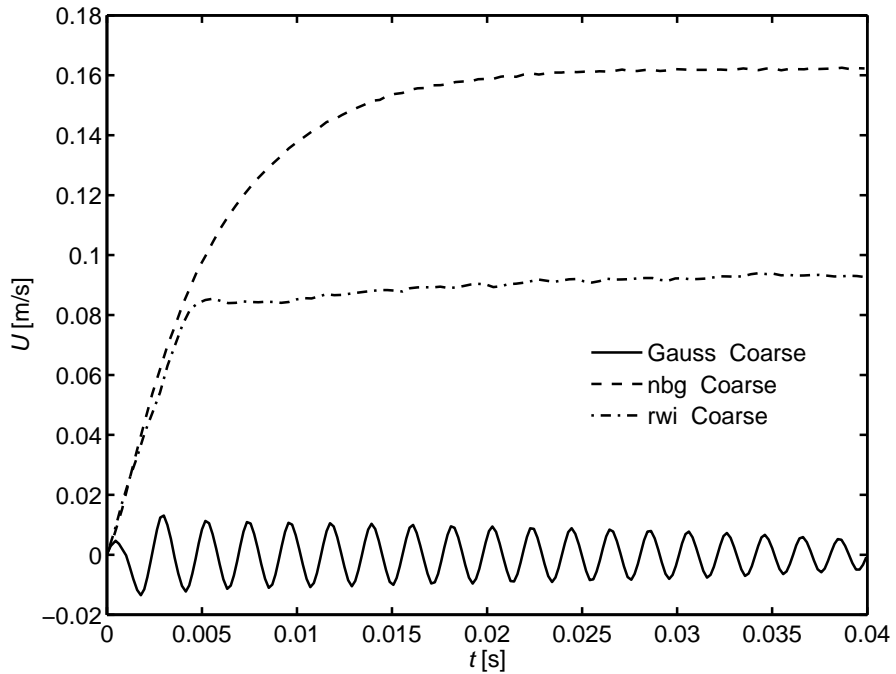


**Figure 5.6:** Bubble rise velocity history for the case Medium ( $d_e = 0.5$  mm). Results from the Gauss, nbg and rwi methods (OpenFOAM code).

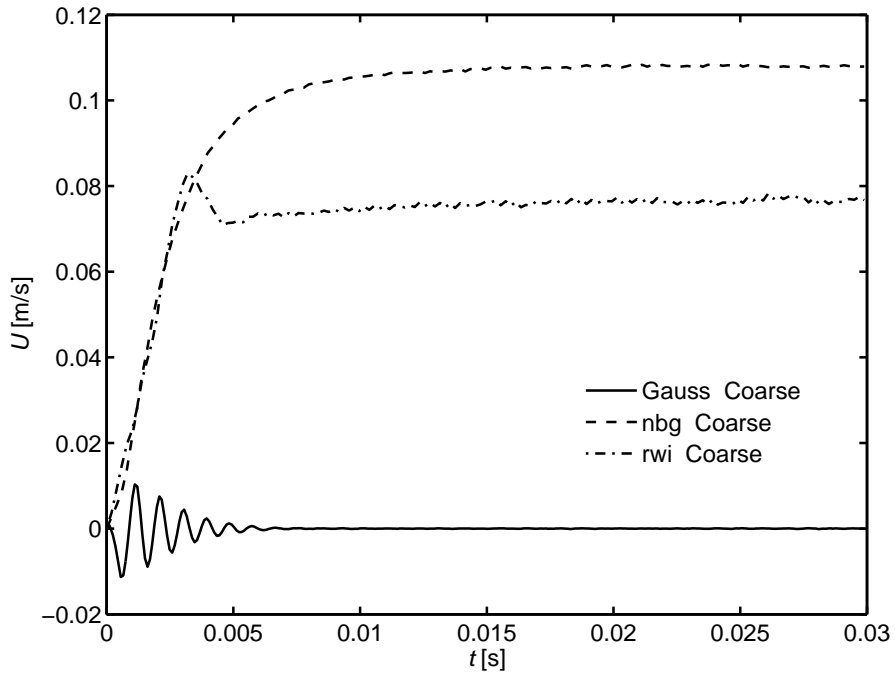


**Figure 5.7:** Bubble rise velocity history for the case Small ( $d_e = 0.3$  mm). Results from the Gauss, nbg and rwi methods (OpenFOAM code).

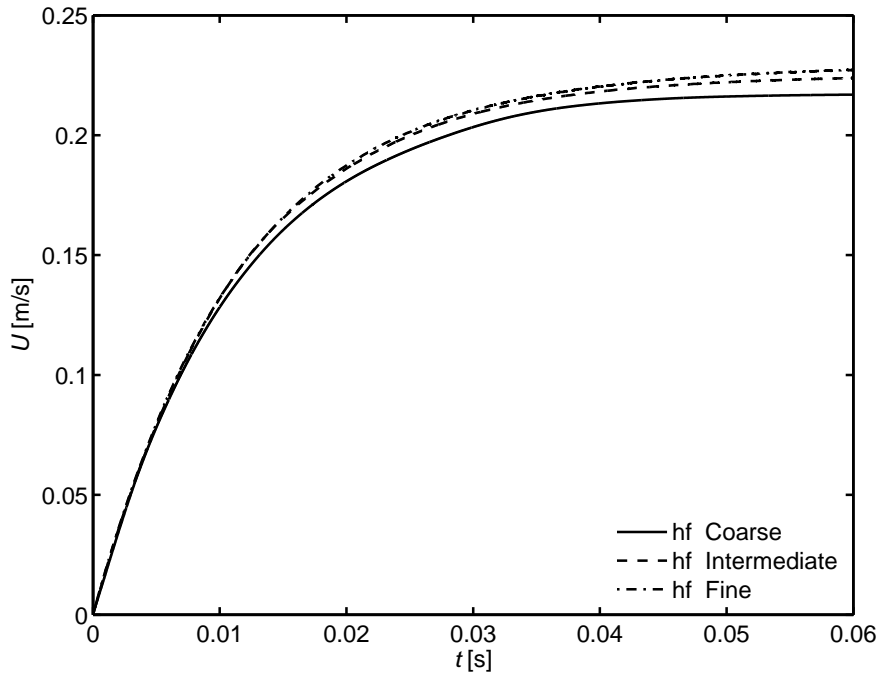


**Figure 5.8:** Bubble rise velocity history for the case Large ( $d_e = 0.9$  mm). Results from the hf method (Gerris Flow Solver code).

### 5.3. Results

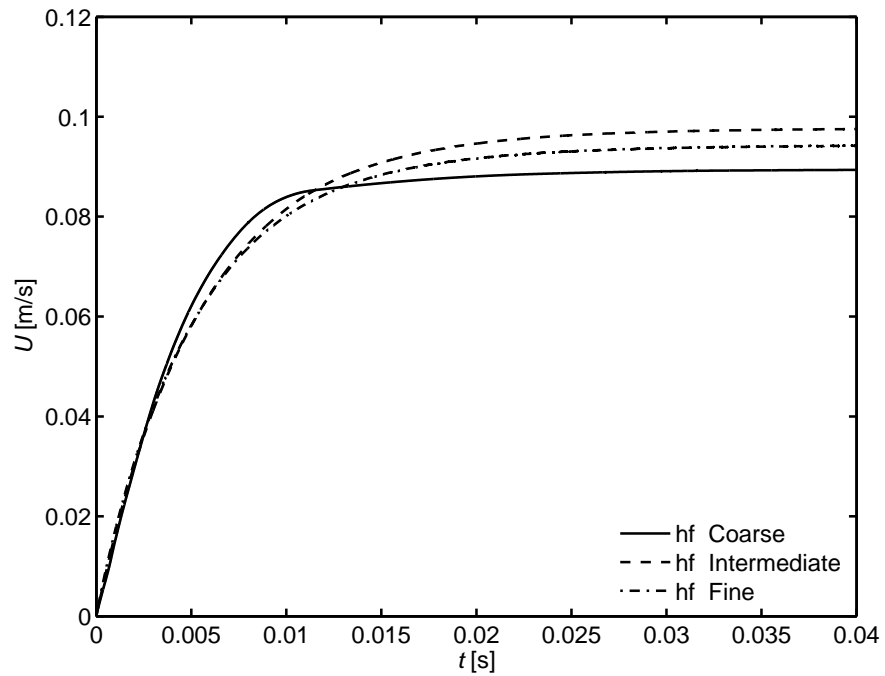


**Figure 5.9:** Bubble rise velocity history for the case Medium ( $d_e = 0.5$  mm). Results from the hf method (Gerris Flow Solver code).

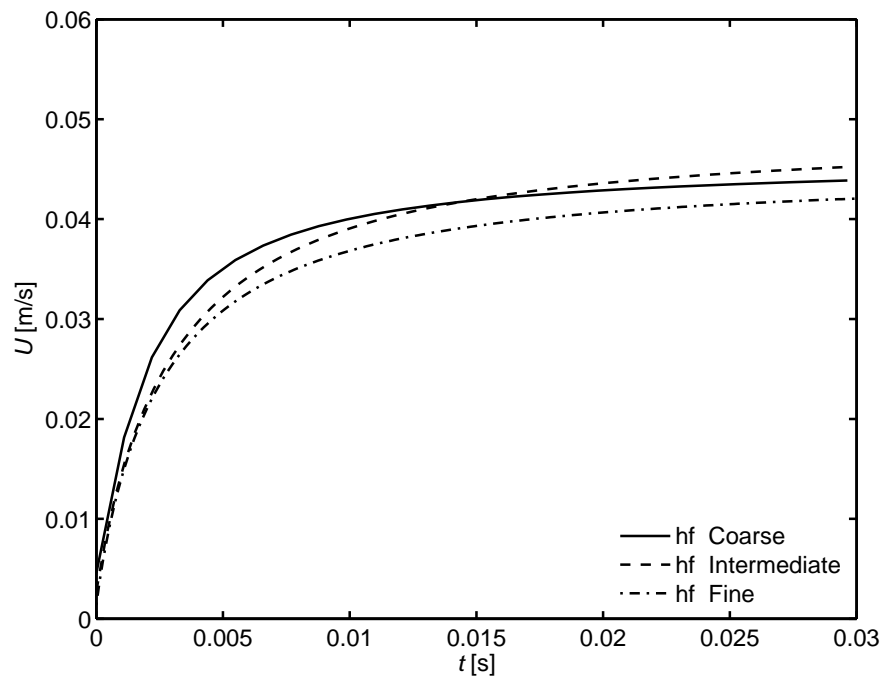


**Figure 5.10:** Bubble rise velocity history for the case Small ( $d_e = 0.3$  mm). Results from the hf method (Gerris Flow Solver code).

### 5.3.4 Flow field description

The behavior shown in Figures 5.5, 5.6 and 5.7 can be better understood and explained by looking at the velocity field around the bubble during its rise. As shown in Figure 5.11 and 5.12, for the *height function* method, a physically correct distribution of the velocity vectors is observed with its maximum velocity in the proximity of the axis of symmetry. Furthermore, a regular vortex at the lateral extremities of the bubble is observed, while the bubble maintains a spherical shape. For the *Gauss* method, the presence of spurious is clearly noticed however the bubble shape remains spherical. On the contrary, for the *node-based gradient* and *recursive weighted interpolations* methods, the bubble shape is nearly spherical however the effects of spurious currents on the flow field are significantly reduced. In particular, the velocity field obtained with the *recursive weighted interpolations* method is very close to the one obtained with the *height function* method.

As the bubble diameter becomes smaller, the spurious currents observed with the *Gauss* become more significant compared to the velocity of the bubble. This is due to the increasing capillary forces. These stronger spurious velocities are able to markedly modify the transport of the bubble, influencing the rise velocity until the bubble definitively stops, as observed for the case Small. As the bubble size is reduced, an increased influence of the spurious currents on the velocity field is also observed for the *node-based gradient* and *recursive weighted interpolations* methods.

Despite these drawbacks, the results obtained with the *recursive weighted interpolations* method are acceptable considered the challenges induced with such bubble dimensions. The method can therefore be used to investigate heat and mass transfer phenomena. Ideally, the *height function* method should be used however it is limited to orthogonal meshes. In alternative to the *recursive weighted interpolations* method, the *node-based gradient* method may be employed, with comparable accuracy and stability. In alternative, a coupled level-set volume-of-fluid method could be implemented in order to improve the accuracy of the interfacial curvature calculation method. However, a correct and efficient implementation is not trivial, especially when non-orthogonal meshes are adopted.

### 5.3. Results

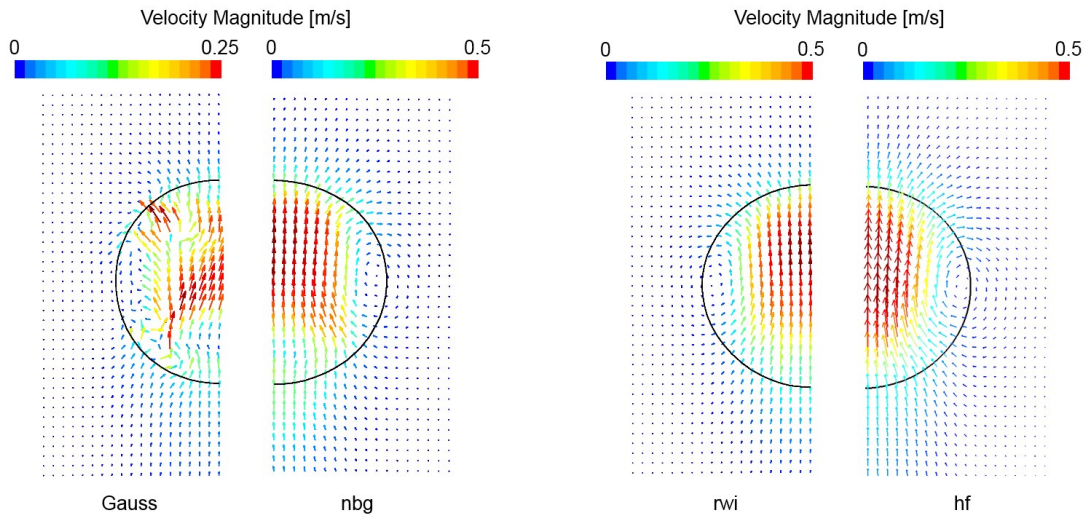


**Figure 5.11:** Velocity vector field around the bubble for the case Large ( $d_e = 0.9 \text{ mm}$ ). Results from the Coarse mesh resolution at  $t = 0.05 \text{ s}$ .

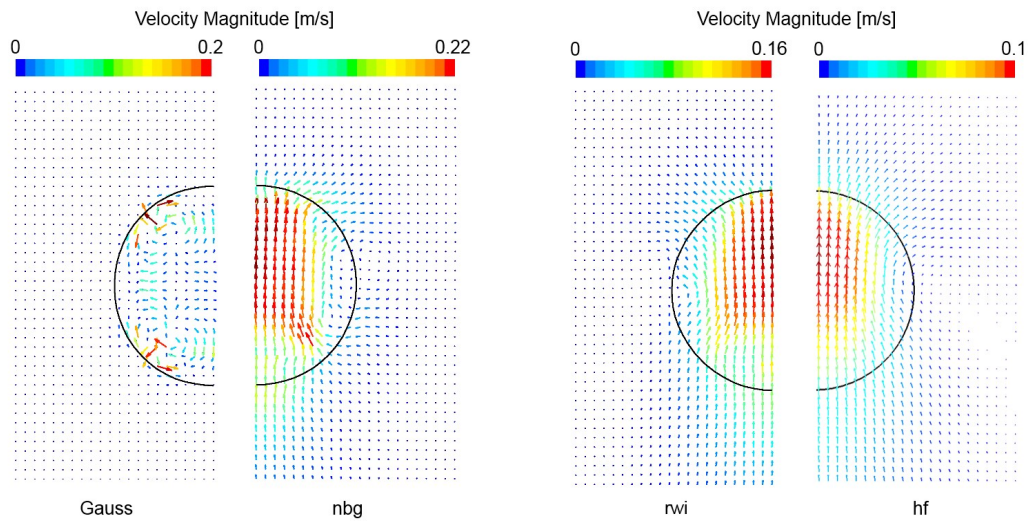


**Figure 5.12:** Velocity vector field around the bubble for the case Small ( $d_e = 0.3 \text{ mm}$ ). Results from the Coarse mesh resolution at  $t = 0.02 \text{ s}$ .



---

# CHAPTER 6

---

## **Single bubble nucleate pool boiling benchmark**

---

In this chapter, a benchmark for the simulation of single bubble nucleate pool boiling is proposed. Previously, the phase change model has been tested on simple one-dimensional and two-dimensional test cases with analytical solution. For a more thorough validation of the developed model, comparisons with experimental data on real situations are required. In order to achieve this goal, part of the activities of the present thesis were performed at MIT in the Buongiorno's group. They consisted in supporting the experimental team for the definition of the experimental boundary conditions and the post-processing of the results. Recently, Buongiorno's group published a series of experimental data obtained at the MIT pool boiling facility (Duan et al., 2013). Some of the data presented in this paper are used to define the following benchmark. Additional post-processing, consisting in digitizing bubble shape and averaging the results between ebullition cycles, is performed in order to allow a direct comparison of the numerical results with the experimental data. The validation of phase change model can be achieved by comparing the predictions of the bubble shape, growth and detachment from the heated wall as well as the temperature field above the heated wall. Unfortunately, due to the computational time required, numerical results are not yet available thus only the definition of the boundary conditions and computational domain are presented together with the experimental results.

---

### **6.1 The MIT pool boiling facility**

---

The facility uses a combination of high-speed infrared (IR) thermometry, digital video (HSV) and Particle Image Velocimetry (PIV) to measure the temperature, phase and velocity distributions in the proximity of a boiling surface. The data chosen for the benchmark are not from the experiments using PIV because a higher quality of the

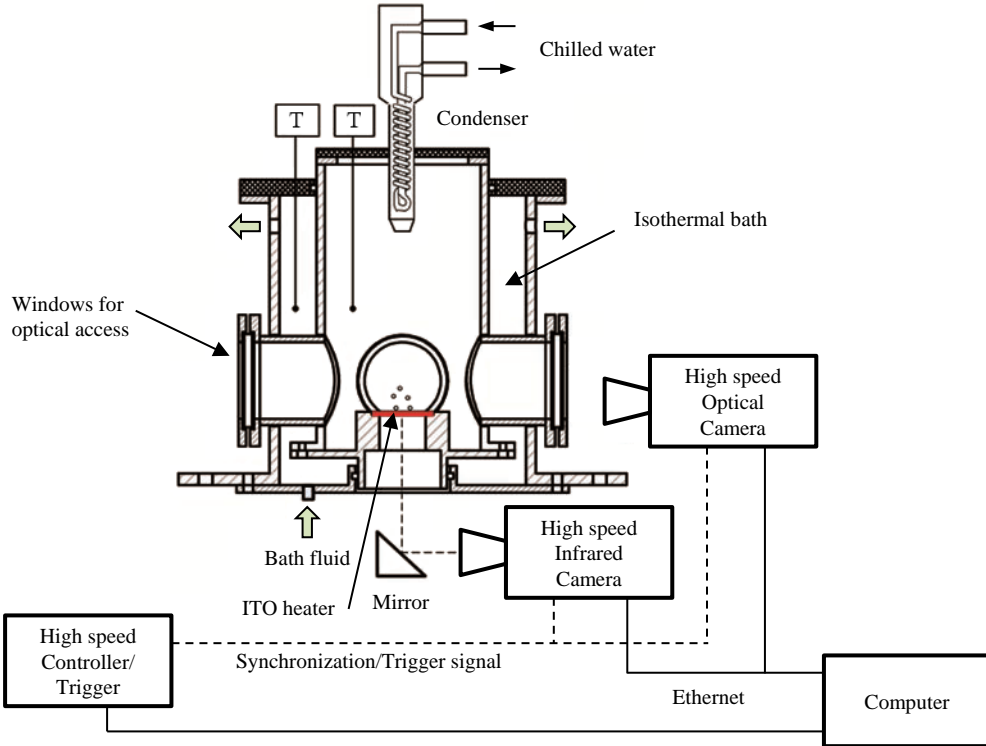


**Figure 6.1:** Schematic of the MIT pool boiling facility. Lateral windows are provided for the HSV (the spherical shape around the ITO heater represents the front and back access windows). The bottom access port is for the IR thermometry.

bubble shape is obtained without the presence of particle within the fluid. A schematic of the facility in this configuration is given in Figure 6.1. It is made of two concentric cylinder structures, forming an inner and an outer cell. Boiling occurs in the inner cell over a flat horizontal electric heater (the ITO heater), that will be described below. The outer cell serves as an isothermal bath to control the temperature of the whole facility, prior and during the experiments. On the top of the inner cell, a reflux condenser is inserted to prevent loss of water through evaporation and to maintain the test cell at atmospheric pressure. Four glass windows are located along the inner cell surface. They are equally spaced of  $90^\circ$  to allow PIV imaging. The bulk temperatures of the fluids is monitoring using thermocouples into the inner cell and the isothermal bath. Stainless-steel, grade 316, is used for all metal parts to minimize corrosion.

The specially designed heater over which boiling of saturated de-ionized water occurs is a thin film heating element made of Indium-Tin-Oxide (ITO). The ITO layer of  $0.7 \mu\text{m}$  thickness is vacuum deposited onto a sapphire substrate of  $250 \mu\text{m}$  thickness to provide mechanical stability. Silver electrode pads of  $20 \mu\text{m}$  thickness are used to pass a DC current to the heater. The size of the sapphire substrate is  $50 \times 50 \text{ mm}^2$ , while the exposed heating area of the ITO is  $20 \times 10 \text{ mm}^2$ .

The ITO heating element is heated by Joule effect and boiling occurs on the upward facing side of the ITO film. The heating element is sealed using silicon gel and the

## 6.1. The MIT pool boiling facility

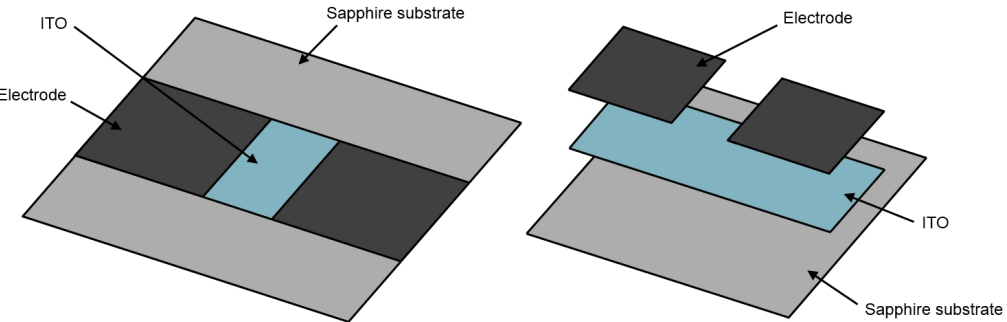


**Figure 6.2:** Schematic of the ITO heater.

bottom surface of the sapphire substrate is exposed to air, effectively turning the sealed heater into a window on the bottom surface of the inner cell. The ITO is transparent in the visible range (380–750 nm) but opaque in the mid-IR range (3–5  $\mu\text{m}$ ), while the sapphire substrate is transparent in both the visible and mid-IR ranges. This combination allows temperature measurement on the bottom of the ITO layer with the high-speed IR camera. Because the ITO heater is so thin, the temperature drop across the ITO is negligible, so the IR camera effectively measures the temperature of the boiling surface. A detailed analysis of such assumption is given in Gerardi (2009). The static contact angle of water on the ITO is of the order of 80–90° as measured (at room temperature) on the actual heaters in the facility.

A Phantom 12.1 high speed video camera (Vision Research, Wayne, New Jersey, USA) is used for imaging the bubbles. The camera's complementary metal-oxide-semiconductor (CMOS) sensor is  $25.6 \times 16.0 \text{ mm}^2$  with a  $20 \mu\text{m}$  pixel size. An AF Micro-Nikkor 200 mm f/4D lens (Nikon, Tokyo, Japan) is used for “close-up” imaging of the bubbles. The long working distance (260 mm) of this lens allows the camera to reach its 1:1 reproduction rate with a safe distance from the hot boiling cell. When this magnification is kept during the imaging process, the images will always have a  $20 \mu\text{m}/\text{pixel}$  scale. This leads to a  $20 \mu\text{m}$  spatial resolution in analyzing the HSV images and a maximum field of view (FOV) of  $25.6 \times 16.0 \text{ mm}^2$  in the flow field. When extension rings are used for the camera lens, spatial resolution of better than  $15 \mu\text{m}$  can be achieved.

To acquire the temperature distribution on the heater surface, an infrared (IR) high-speed camera is used to measure IR intensity. The IR camera is an SC6000 from FLIR systems, Boston, Massachusetts, USA. The camera has an Indium Antimonide (InSb) detector that operates in the 3–5  $\mu\text{m}$  wavelength range (mid-IR) and has a maximum resolution of  $640 \times 512$  pixels. A 100 mm germanium lens (f/2.3) with a 3/4-inch extension ring is used to achieve the desired spatial resolution at the optimal camera distance from the reference plane. In the experiment, only a small window (e.g.,  $224 \times 116$  pixels) is needed for imaging the whole ITO heater surface, allowing for a high frame rate of 1,000 fps. For measurement of a single bubble, an even higher frame rate can be achieved; frame rates up to 3,000 fps were used in the experiment.

## Chapter 6. Single bubble nucleate pool boiling benchmark

---

**Table 6.1:** Thermo-physical properties of water, ITO and sapphire at 100 °C.

Property	Water (liquid)	Water (vapor)	ITO	Sapphire
Density (kg m <sup>-3</sup> )	958	0.6	7160	3980
Thermal conductivity (W m <sup>-1</sup> K <sup>-1</sup> )	0.68	0.025	8.7	30
Specific heat capacity (J kg <sup>-1</sup> K <sup>-1</sup> )	4216	2080	340	760
Dynamic viscosity (Pa s)	$2.82 \times 10^{-4}$	$1.23 \times 10^{-5}$	n/a	n/a
Heat of vaporization (J kg <sup>-1</sup> )		$2.256 \times 10^6$	n/a	n/a
Surface tension (N m <sup>-1</sup> )		0.058	n/a	n/a

## 6.2 Simplifying assumptions

---

The benchmark is aimed at the simulation of bubble growth and detachment in a pool of saturated de-ionized water at atmospheric pressure ( $T_{\text{sat}} = 100$  °C,  $p = 1$  atm). The following simplifying assumptions are recommended for the simulations:

- at the selected experimental conditions (i.e., low heat flux), the bubbles can be considered isolated from each other, i.e., interaction with bubbles at neighboring nucleation sites can be ignored;
- given the small temperature changes (from 100 to 110 °C), constant thermo-physical properties may be used for water, ITO and sapphire. Table 6.1 summarizes the recommended values of the relevant properties.
- in principle, several bubble growth and detachment cycles should be performed in the simulation until the temperature and velocity fields for bubble are similar to those of the previous one, i.e., until periodic conditions are achieved. This may be computationally prohibitive, thus the initial conditions should be as close as possible to the periodic conditions (which are unknown a priori). The PIV measurements have shown that at low heat fluxes, i.e., the conditions of interest, the fluid is almost at rest after a bubble departure. Thus an initial null velocity field can be adopted in the simulations. Infrared images have also shown that the temperature distribution on the ITO surface in the proximity of a nucleation site rapidly becomes uniform after a bubble departs, thus suggesting that an initial temperature distribution consistent with transient conduction throughout the domain could be specified.
- the sapphire substrate has a quite high thermal diffusivity thus the effects of conjugate heat transfer on the solution may not be negligible. However, for some codes, the conjugate heat transfer feature may not be available. In such case, a simplification could be to assign a constant heat flux at the bottom boundary of the fluid domain. In effect, the thinness of the ITO heater permits to consider the heat generation rate as planar and distributed uniformly along the heater surface.

### 6.3. Computational domain, boundary conditions and initialization

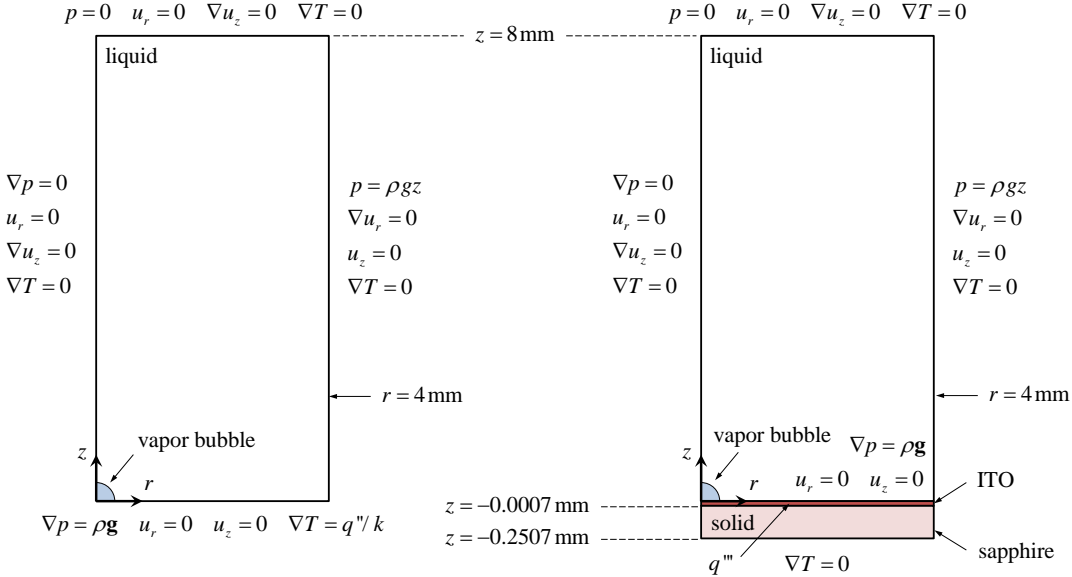


**Figure 6.3:** Schematic of the two possible computational domains (drawing not in scale).

## 6.3 Computational domain, boundary conditions and initialization

In this section, the settings for the computational domain, the boundary conditions and the initialization of the simulations are discussed.

### 6.3.1 Computational domain

Two different computational domains can be adopted depending on the assumptions made: without conjugate heat transfer or with conjugate heat transfer. The corresponding schematic of these domains are displayed in Figure 6.3. A single isolated bubble is analyzed and an axisymmetric domain is used. The hypothesis of axisymmetry is confirmed by the high-speed video visualization. The vertical axis of the bubble is the axis of symmetry. The dimension of the domain in the  $r$ -direction is 4 mm or higher, while the height of the fluid domain can be 8 mm or higher depending on the size of the bubble at detachment. The ITO has a thickness of  $0.7 \mu\text{m}$  while the sapphire substrate has a thickness of 0.25 mm. At the conditions of interest, the vapor bubbles typically have a departure radius of 1 to 2 mm.

### 6.3.2 Boundary conditions

The boundary conditions for the pressure, velocity and temperature are identified in Figure 6.3. The left boundary, i.e., along the  $z$ -axis with  $r = 0$ , should be set to axisymmetry for both the fluid and solid regions. The bottom boundary of the fluid region should be set to a no-slip wall, with the pressure gradient that balance the buoyancy force. The right boundary can be set either to free-slip conditions or to open boundary, i.e., with the pressure corresponding to the hydrostatic pressure of water. If free-slip conditions are used, a larger computational domain may be required to avoid side effects. The top boundary should be set as open, with a null pressure. Note that since

the densities are constant, the flow is incompressible and a pressure relative to the atmospheric pressure is used to reduce round-off errors. If conjugate heat transfer is considered, all boundaries can be set to adiabatic. Otherwise, imposed heat flux boundary condition should be set for the bottom boundary of the fluid region. A contact angle between 80° to 90° should be set on the bottom boundary, as measured (at room temperature) on the actual heaters in the facility. Note however that temperature and dynamic effects may change the value of the contact angle at the heater wall.

The chosen experiments for the present test case present the following conditions:

- heat generation rate:  $q''' = 41 \text{ GW m}^{-3}$ ;
- corresponding heat flux:  $q'' = 28.7 \text{ kW m}^{-2}$ ;
- nucleation temperature:  $T_n = 109.0 \text{ }^\circ\text{C}$ .

### 6.3.3 Initial conditions

Simulation of the actual micro-cavity from which the bubble would nucleate is beyond the scope of this test case. Therefore, to start the bubble growth simulation, a small bubble will have to be “seeded” at a prescribed location on the wall, with a prescribed nucleation temperature of  $T_n$ . As described by Plesset and Zwick (1954), the growth of a bubble in a superheated liquid is characterized by a first inertia-controlled phase, where density variations due to pressure play a major role. In order to capture this preliminary phase, special treatments should be implemented in the CFD model. In most cases, only the thermally-controlled phase is of interest. As a consequence the bubble can be initialized with a radius of about 100  $\mu\text{m}$ . The shape of the bubble can be considered as a spherical cap attached to the wall.

In most numerical method, the pressure solution is implicit at each time step, thus an initial condition for pressure is generally not necessary and a null pressure field can be set. A null velocity field should also be set as described previously in the simplifying assumptions.

Since the thermal diffusivity of sapphire is high, a uniform temperature equal to the temperature of nucleation ( $T_n$ ) may be assumed throughout the sapphire substrate at the beginning of the simulation. The temperature distribution within the liquid near the wall is the result of transient conduction heat transfer following the departure of the previous bubble. The temperature of the liquid far from the wall is equal to the saturation temperature. The following equation is a reasonable assumption for the initial liquid temperature profile within the domain:

$$T(z) = \begin{cases} T_n & z \leq 0, \\ T_n + \frac{T_{\text{sat}} - T_n}{0.213}z & 0 < z < 0.213, \\ T_{\text{sat}} & z \geq 0.213, \end{cases} \quad (6.1)$$

with  $z$  expressed in mm. This temperature profile assure that the temperature gradient at the heater wall corresponds to the imposed heat flux. After the liquid temperature is initialized, the temperature within the vapor bubble can be set. A good approximation may be to assign the saturation temperature within the vapor bubble.

## 6.4 Data post-processing

---

In order to compare the results of the simulations with the experimental data, the investigator should monitor the following quantities as a function of time:

- bubble volume;
- bubble surface area;
- bubble center of mass (after detachment it can be used to estimate the bubble rise velocity);
- bubble maximum vertical position (defines the bubble height during bubble growth);
- bubble maximum radial position (defines the bubble lateral diameter,  $d_{\text{lateral}}$ , during bubble growth);
- bubble minimum radial position for  $z < 100 \mu\text{m}$  (defines the bubble base diameter,  $d_{\text{base}}$ , during bubble growth);
- interface shape at times (0.7, 2.8, 6.9, 13.2, 17.3) ms and eventually at (22.9, 27.1, 31.2) ms;
- temperature field over the heater surface at times (0.42, 2.50, 6.66, 8.75, 19.16, 35.81, 117.44) ms;
- average temperature over the heater surface,  $\langle T_{\text{wall}} \rangle$ .

The definition of  $d_{\text{lateral}}$ ,  $d_{\text{base}}$  and bubble height is shown in Figure 6.4. The bubble volume and surface area can be used to determine the history of the mass transfer rate. Comparing it with the integral of the local mass transfer rate from the phase change model can also be done to check the global mass conservation.

The interface shape and temperature field are to be compared with experimental data obtained at specific times (see next section).

Finally the average temperature is used to compute the history of the heat transfer coefficient defined as

$$h = \frac{q''}{\langle T_{\text{wall}} \rangle - T_{\text{sat}}}, \quad (6.2)$$

where  $q''$  is the imposed surface heat flux. The average heat transfer coefficient can also be determined from the time average wall temperature

$$\bar{h} = \frac{q''}{\overline{\langle T_{\text{wall}} \rangle} - T_{\text{sat}}}, \quad (6.3)$$

with

$$\overline{\langle T_{\text{wall}} \rangle} = \frac{1}{t_{\text{cycle}}} \int_0^{t_{\text{cycle}}} \frac{1}{A} \int_A T(r, t) dA dt. \quad (6.4)$$

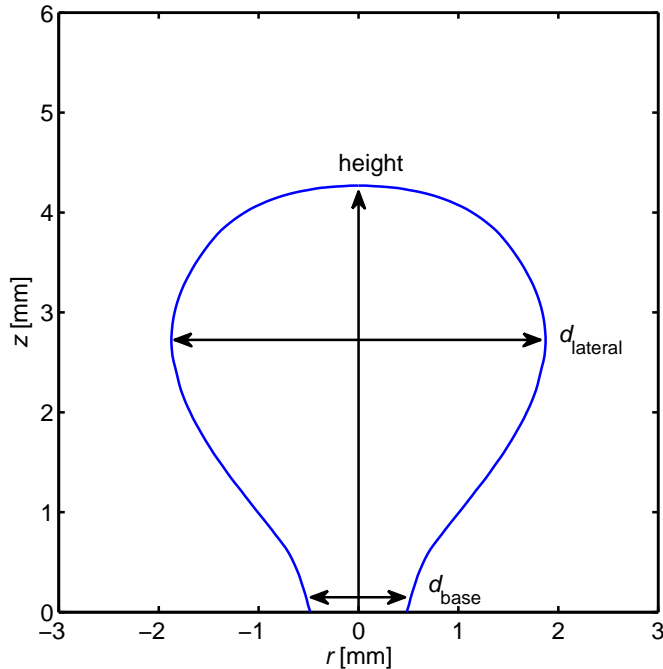


**Figure 6.4:** Schematic of the characteristic dimensions of the bubble during bubble growth.

## 6.5 Experimental results

The experimental data used to determine this benchmark are from experiments without PIV measurements. In effect, the particles present in the fluid in order to perform PIV imaging do not allow an accurate visualization of the bubble shape. Moreover, under the conditions of interest, i.e., low heat fluxes and laminar flow, the correct prediction of the bubble shape is more challenging than the correct prediction of the velocity field. PIV measurements may be appropriate at high heat fluxes for the estimation of the enhanced convection heat transfer due to the motions induced by the bubbles.

Data from synchronized high-speed video (HSV) and infrared (IR) thermometry are therefore available and the experimental conditions are as follows:

- pressure: 1 atm;
- water bulk temperature:  $99.5 \pm 1.1$  °C;
- HSV frame rate: 7,204 fps;
- IR frame rate: 2,401.3 fps (synchronized within 3  $\mu$ s);
- nucleation temperature:  $109.0 \pm 2$  °C; this would correspond to a nucleation site (microcavity) of critical diameter  $\approx 6$   $\mu$ m according to the Young–Laplace and Clausius–Clapeyron equations Rohsenow et al. (1998).

A good repeatability of the results is observed and three consecutive bubbles at a single nucleation site are chosen from the dataset.

## 6.5. Experimental results

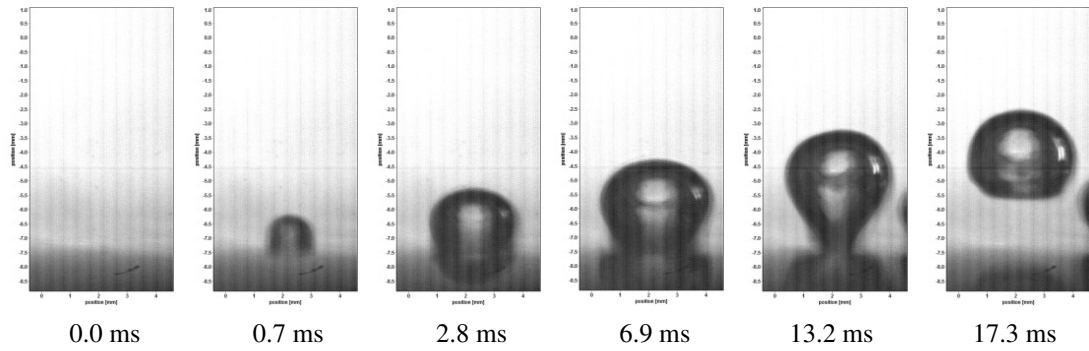


**Figure 6.5:** Sequence of HSV images for the first bubble.

### 6.5.1 High-speed video imaging

In order to obtain information about the bubble shape, dimensions and departure frequency, HSV images were taken from a side window of the boiling cell (see Figure 6.1). A typical sequence of images taken for the first bubble are shown in Figure 6.5. The repeatability of this sequence between the three consecutive bubbles is excellent (Duan et al., 2013). The average shape of the bubbles is thus computed from the dataset and is given in Figure 6.6. The results from the simulations can be compared directly with these digitized experimental shapes.

In addition to the bubble shape, three of its characteristic dimensions have been monitored in the experiments. These dimensions are respectively the lateral diameter,  $d_{\text{lateral}}$ , the base diameter,  $d_{\text{base}}$ , and the bubble height (see Figure 6.4 for more details). The results for the three bubbles are displayed in Figure 6.7 together with an average time evolution of the bubble characteristic dimensions.

### 6.5.2 High-speed IR measurements

The temperature of the heating surface is obtained from high-speed IR measurements from the bottom access port of the boiling cell (see Figure 6.1). Both IR and HSV are synchronized within  $3 \mu\text{s}$  and the frequency of IR acquisition is one-third the frequency of the HSV acquisition. A detailed analysis of the temperature field underneath the bubble together with the bubble shape and dimensions is therefore possible.

Again, the results obtained for the three consecutive bubbles have a good repeatability. The radial distributions of the azimuthally average temperature,  $T(r, t)$ , show a precision  $< 0.5^\circ\text{C}$ . In Figure 6.8, the average distribution of  $T(r, t)$  between the three bubbles is displayed. It can be observed the cold ring due to the microlayer evaporation (note that the three phase contact line position is about  $r = 1 \text{ mm}$  for  $t > 2 \text{ ms}$ ). The dry spot at the nucleation site is also clearly visible, and expands as the bubble grows.

The time history of the temperature at the nucleation for the three ebullition cycle is given in Figure 6.9. From this result it is possible to estimate the bubble frequency, bubble growth time and wait time between each cycle.

Finally a series of average heat transfer coefficients calculated for various radial size of the integration domain is displayed in Figure 6.10.

From both the HSV images and IR measurements, it can be observed the following parameters in this experiment:

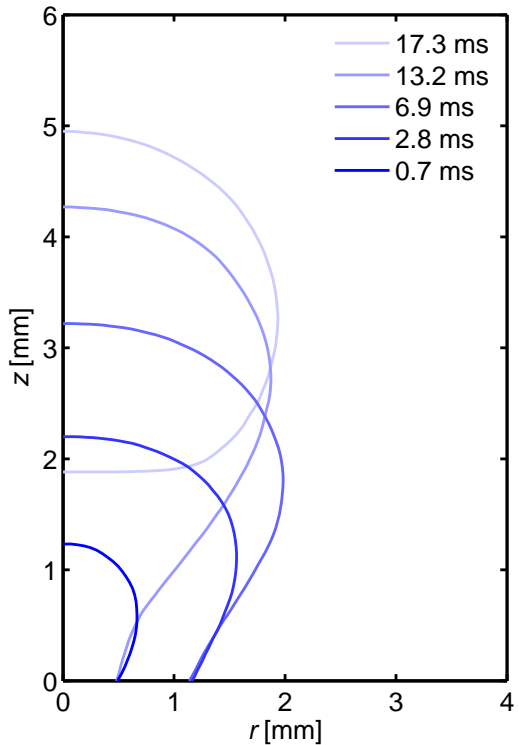


**Figure 6.6:** Schematic of the characteristic dimensions of the bubble during bubble growth.

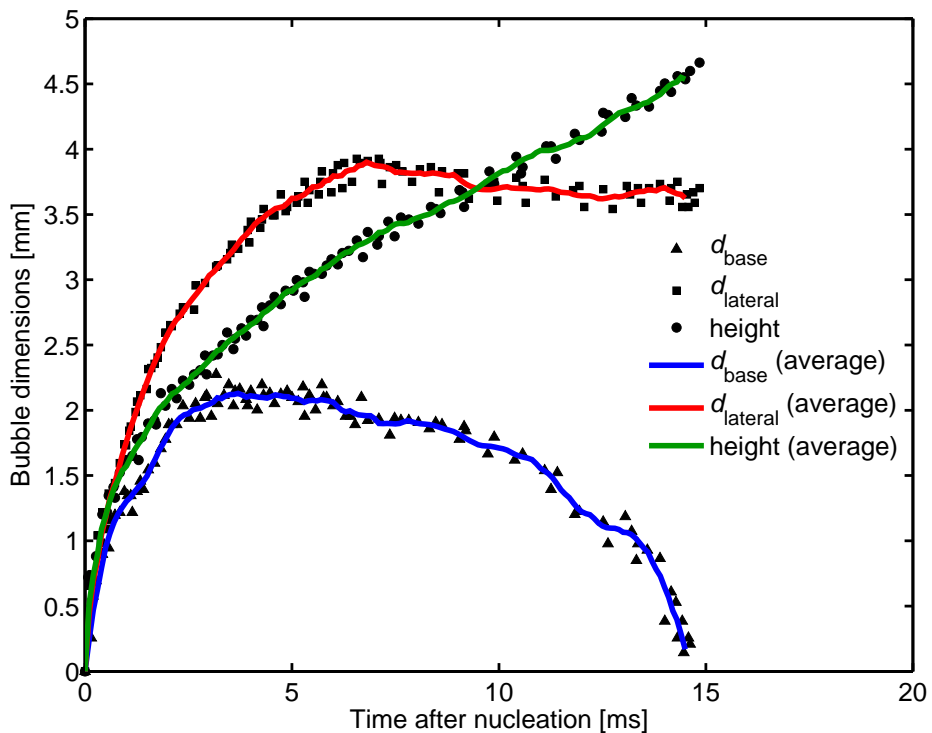


**Figure 6.7:** Time evolution of the characteristic dimensions of the three bubbles. The measurements have an accuracy of  $\pm 0.04$  mm.

## 6.5. Experimental results

- bubble frequency:  $\approx 4.7$  Hz;
- bubble growth time:  $14.7 \pm 0.2$  ms;
- wait time:  $\approx 200$  ms;
- bubble departure diameter:  $3.8 \pm 0.07$  mm;
- average heat transfer coefficient:  $\approx 3.18 \text{ kW m}^{-2} \text{ K}^{-1}$ .

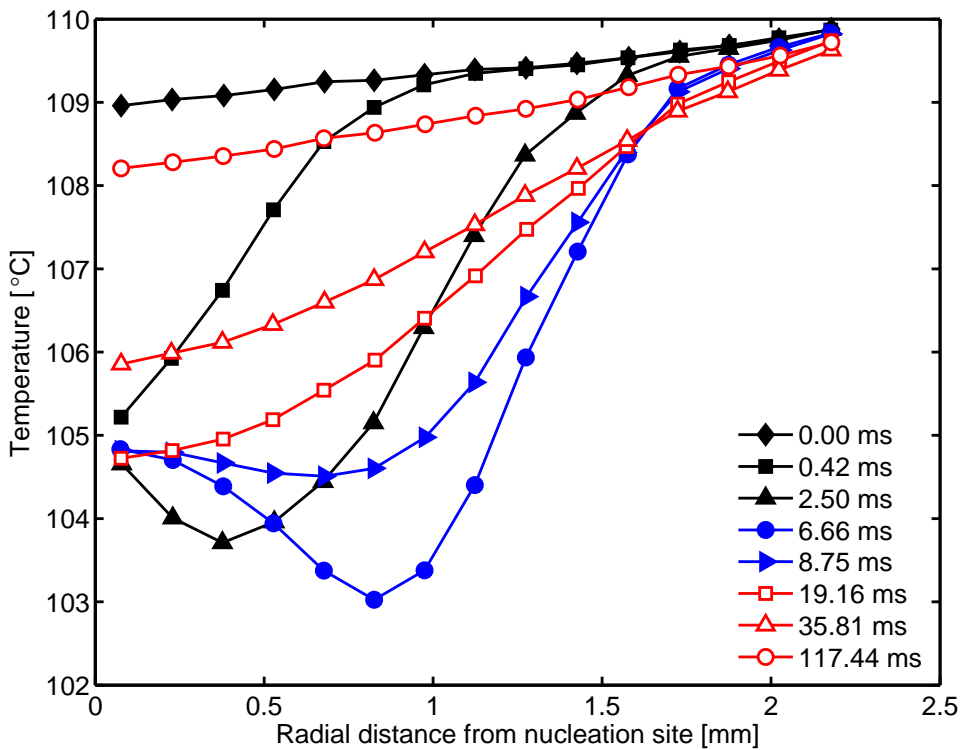


**Figure 6.8:** Radial distribution of the azimuthally average temperature (averaged between the three bubbles). Curves with empty symbols are after bubble departure. Accuracy of the measured temperature is  $\pm 2$  °C, and precision is  $< 0.5$  °C.

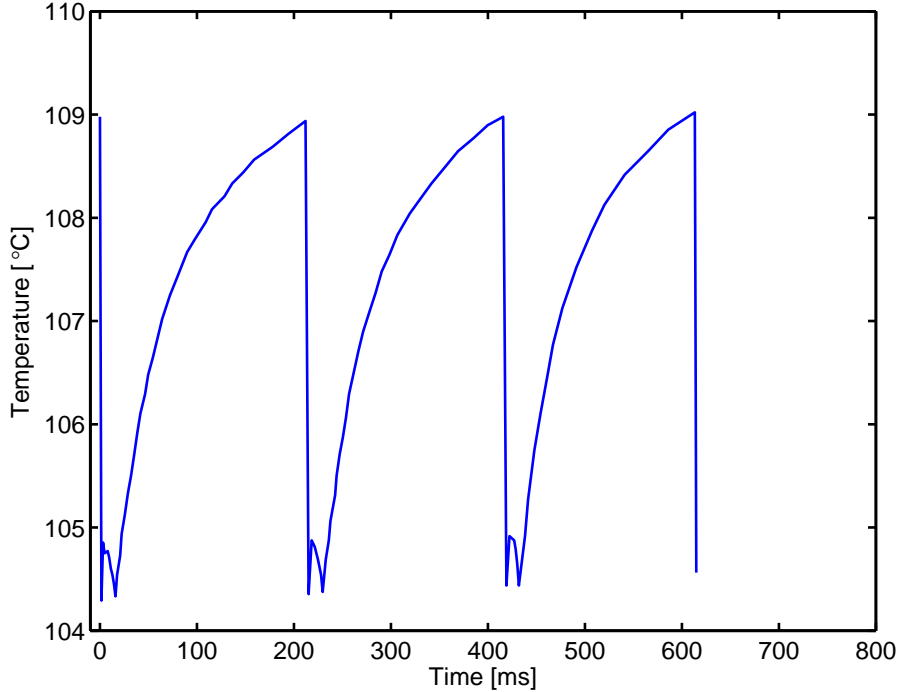


**Figure 6.9:** Time history of the temperature at the nucleation site. Accuracy of the measured temperature is  $\pm 2^{\circ}\text{C}$ .

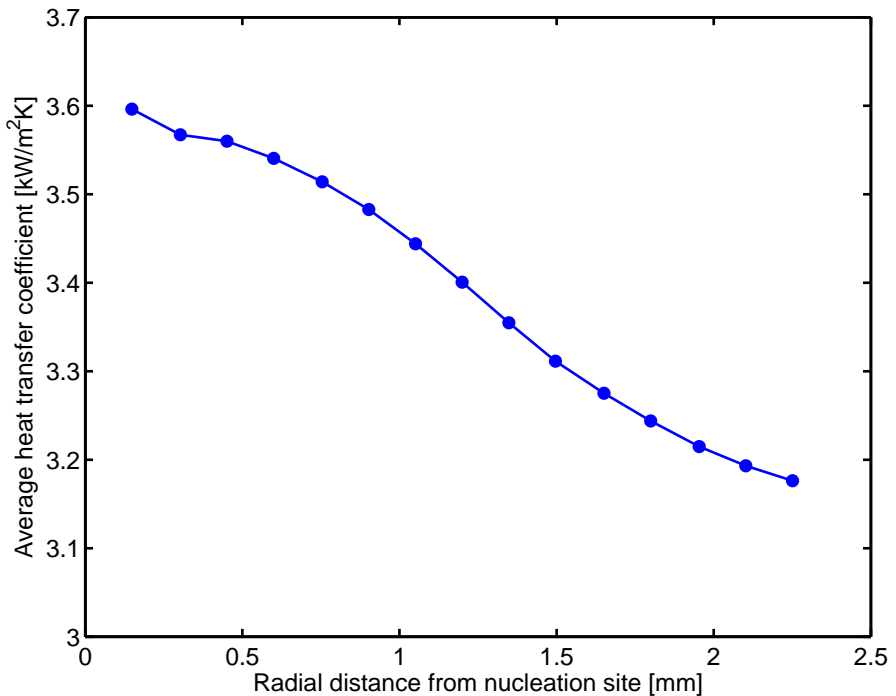


**Figure 6.10:** Average heat transfer coefficient as a function of the radial size of the integration domain. Average between the three ebullition cycles. Accuracy of the calculated heat transfer coefficient is  $\pm 0.8 \text{ kW m}^{-2} \text{ K}^{-1}$ , and precision  $< 0.2 \text{ kW m}^{-2} \text{ K}^{-1}$ .

---

# 7

## CHAPTER

---

# Conclusions and outlook

---

## 7.1 Summary

---

In this thesis, a flexible and reliable numerical method for the simulation of two-phase heat and mass transfer has been implemented. The method has been applied to the simulation of boiling heat transfer, which is a relevant mode of heat transfer within the energy production and conversion sector. A detailed description of the governing equations and of the implemented numerical method has been provided, followed by a proper verification and validation process. Then the model has been applied to the simulation of isothermal rising air bubbles in water with dimensions typical to heat and mass transfer applications. Finally, a benchmark for the simulation of single bubble nucleate pool boiling has been developed.

The derivation of the governing equations for a two-phase heat and mass transfer problem has demonstrated that the form of the energy equation using a one-fluid formulation is not trivial. When a smooth Heaviside function is adopted instead of a sharp Heaviside function, several additional terms related to the mixture quantities also arise and need to be closed. For these reasons, it is preferred to solve the energy equation for each phase separately by implementing a Ghost Fluid Method, where the boundary conditions at the interface are taken into account at the cell centers by modifying the discretization of the various terms in the energy equation. This constitutes an improvement with respect to the phase change methods that have already been implemented in OpenFOAM.

Two interfacial curvature calculation method, denoted as *node-based gradient* and *recursive weighted interpolations*, have been proposed in addition to the original method implemented in OpenFOAM and to the *height function* method implemented in the Gerris Flow Solver code, used as a reference in terms of accuracy. The proposed methods are compatible with non-orthogonal and unstructured meshes. On the contrary, the

## Chapter 7. Conclusions and outlook

---

*height function* method is limited to orthogonal meshes. The static bubble and capillary wave test cases have been performed using these four interfacial curvature calculation methods. The *node-based gradient* method showed higher spurious velocities near the interface with respect to the *recursive weighted interpolations* method. However a higher accuracy of the *node-based gradient* method has been observed on the capillary wave test case, suggesting a higher temporal resolution of the method. The simulations of spherical rising air bubbles in water also demonstrated a more physical behavior of the bubble rise velocity for the *node-based gradient* with respect to the *recursive weighted interpolations* method. However, the latter predicted a more regular velocity field within the bubble, which is close to the velocity field observed with the *height function* method. In general, the two methods proposed in this thesis performed better than the original *Gauss* method implemented in OpenFOAM.

The verification and validation of the phase change model has been performed through the simulation of the Stefan, sucking interface and spherical bubble growth problems. The one-dimensional Stefan problem proved that the diffusion term is implemented correctly and that the model well predicts the mass transfer rate and interface position in this case. The one-dimensional sucking interface problem permitted to evidence a possible improvement in the discretization of the convection term. In this case, the accuracy of the solution had a high dependence on the mesh element size. However for fine enough meshes, the accuracy was good. Finally, the spherical bubble growth problem, simulated using a three-dimensional computational domain, showed that some improvements can be obtained by improving the discretization of the convection term and by improving the method used to calculate the mass transfer rate. A high dependence of the results on the mesh element size was again observed for this test case. Relatively good accuracy has been obtained for the finest mesh however.

The newly developed phase change model presented in this thesis therefore relies on an improved solution of the energy equation, a sharp treatment of the mass transfer sources and on a more accurate interfacial curvature calculation method. These constitute some enhancements of the already existing phase change models implemented in OpenFOAM. In particular, less computationally expensive meshes may be employed due to a more concentrated distribution of the mass transfer around the interface and a more consistent solution of the energy equation.

A benchmark for the simulation of single bubble nucleate pool boiling has been finally developed in order to test the developed model. The high resolution experimental data obtained at the MIT pool boiling facility permitted to define detailed boundary conditions at the heater surface. Three consecutive ebullition cycles presenting a good repeatability have been analyzed. The time history of the bubble shape has been digitized and averaged over the three bubbles, allowing a direct comparison with simulation results. Averaged temperature profiles and bubble dimensions have also been extracted from the dataset. Finally, some global parameters of the experiment such as nucleation time, wait time, bubble frequency and averaged heat transfer coefficient have been determined. This collection of data will permit to thoroughly validate the developed numerical model and to determine which part of the model may be improved.

---

## 7.2 Future work

---

The developed and implemented numerical method is considered as preliminary and several improvements can be made regarding its accuracy. Concerning the interface tracking technique, these include:

- treatment of contact angles other than 90°;
- more robust treatment of the relative interface motion in case of mass transfer;
- implementation of a reconstructed Level-Set compatible with non-orthogonal meshes and able to accurately predict the interfacial curvature;
- use of a geometric VOF, preventing the diffusion of the volume fraction field.

On the other hand, the phase change model may be improved by considering the following modifications:

- discretization of the convection term in the energy equation to account for the interface temperature;
- more accurate estimation of the mass transfer rate;
- implementation of a sub-grid model to account for the microlayer evaporation.

With these improvements, the model should be able to simulate boiling phenomena more accurately. We also noticed a limitation on the parallel use of the adaptive mesh refinement feature implemented in the OpenFOAM library. In effect, it is not yet possible to perform dynamic load balancing of the adapted mesh. An improvement of the efficiency of the model could therefore be obtained by enabling parallel load balancing.



---

## Bibliography

---

- Agarwal, D.K., Welch, S.W.J., Biswas, G., Durst, F., 2004. Planar simulation of bubble growth in film boiling in near-critical water using a variant of the vof method. ASME J. Heat Transfer 126, 329–338.
- Alves, S.S., Orvalho, S.P., Vasconcelos, J.M.T., 2005. Effect of bubble contamination on rise velocity and mass transfer. Chem. Eng. Sci. 60, 1–9.
- ANSYS, 2010. ANSYS® FLUENT®, Release 13.0, User's guide and theory guide. ANSYS, Inc., Canonsburg, PA, USA.
- Aris, R., 1962. Vectors, Tensors and the Basic Equations of Fluid Mechanics. Prentice-Hall.
- Benjamin, R.J., Balakrishnan, A.R., 1997. Nucleation site density in pool boiling of saturated pure liquids: Effect of surface microroughness and surface and liquid physical properties. Exp. Therm. Fluid Sci. 15, 32–42.
- Bhaga, D., Weber, M.E., 1981. Bubbles in viscous liquid: shapes, wakes and velocities. J. Fluid Mech. 105, 61–85.
- Brackbill, J.U., Kothe, D.B., Zemach, C.A., 1992. A continuum method for modeling surface tension. J. Comput. Phys. 100, 335–354.
- Carslaw, H.S., Jaeger, J.C., 1959. Conduction of Heat in Solids. Oxford University Press, London.
- Celata, G.P., Cumo, M., D'Annibale, F., Di Marco, P., Tomiyama, A., Zovini, C., 2006. Effect of gas injection mode and purity of liquid on bubble rising in two-component systems. Exp. Therm. Fluid Sci. 31, 37–53.
- Clift, R., Grace, J.R., Weber, M.E., 1978. Bubbles, Drops and Particles. Academic Press, New York.
- Cole, R., 1967. Bubble frequencies and departure volumes at subatmospheric pressures. AIChE J. 13, 779–783.

## Bibliography

---

- Collier, J.G., Thome, J.R., 1994. Convective Boiling and Condensation, 3rd Edition. Clarendon Press, Oxford, UK.
- Colombo, E., Inzoli, F., Mereu, R., 2012. A methodology for qualifying industrial CFD: The Q<sup>3</sup> approach and the role of a protocol. *Comput. Fluids* 54, 56–66.
- Cooper, M.G., 1984. Saturation nucleate pool boiling – A simple correlation, in: Proc. 1<sup>st</sup> UK National heat transfer conference, IChemE symposium series 86, 785–793.
- Cooper, M.G., Lloyd, A.J.P., 1969. The microlayer in nucleate pool boiling. *Int. J. Heat Mass Transfer* 12, 895–913.
- Courant, R., Friedrichs, K.O., Lewy, H., 1928. Über die partiellen differenzgleichungen der matematischen physik. *Matematishe Annalen* 100, 32–74.
- Dai, Z., Dukhin, S., Fornasiero, D., Ralston, J., 1998. The inertial hydrodynamic interaction of particles and rising bubbles with mobile surfaces. *J. Colloid Interface Sci.* 197, 275–292.
- Delgoshaei, P., Kim, J., 2010. Microscale heat transfer measurements during subcooled pool boiling of pentane: Effect of bubble dynamics, in: Proc. of the 14<sup>th</sup> International Heat Transfer Conference IHTC14.
- Delhaye, J.M., 1974. Jump conditions and entropy sources in two-phase systems. local instant formulation. *Int. J. Multiphase Flow* 1, 395–509.
- Demiray, F., Kim, J., 2004. Microscale heat transfer measurements during pool boiling of FC-72: effect of subcooling. *Int. J. Heat Mass Transfer* 47, 3257–3268.
- Dhir, V.K., 2006. Mechanistic prediction of nucleate boiling heat transfer—Achievable or a hopeless task? *ASME J. Heat Transfer* 128, 1–12.
- Dijkhuizen, W., van den Hengel, E.I.V., Deen, N.G., van Sint Annaland, M., Kuipers, J.A.M., 2005. Numerical investigation of closures for interface forces acting on single air-bubbles in water using volume of fluid and front tracking models. *Chem. Eng. Sci.* 60, 6169–6175.
- Dijkhuizen, W., Roghair, I., van Sint Annaland, M., Kuipers, J.A.M., 2010a. DNS of gas bubbles behaviour using an improved 3D front tracking model—Drag force on isolated bubbles and comparison with experiments. *Chem. Eng. Sci.* 65, 1415–1426.
- Dijkhuizen, W., Roghair, I., van Sint Annaland, M., Kuipers, J.A.M., 2010b. DNS of gas bubbles behaviour using an improved 3D front tracking model—Model development. *Chem. Eng. Sci.* 65, 1427–1437.
- Dijkhuizen, W., van Sint Annaland, M., Kuipers, J.A.M., 2010c. Numerical and experimental investigation of the lift force on single bubbles. *Chem. Eng. Sci.* 65, 1274–1287.
- Duan, X., Phillips, B., McKrell, T., Buongiorno, J., 2013. Synchronized high-speed video, infrared thermometry, and particle image velocimetry data for validation of interface-tracking simulations of nucleate boiling phenomena. *Exp. Heat Transfer* 26, 169–197.

## Bibliography

---

- Duineveld, P.C., 1995. The rise velocity and shape of bubbles in pure water at high Reynolds number. *J. Fluid Mech.* 292, 325–332.
- Esmaeeli, A., Tryggvason, G., 2004a. Computations of film boiling. Part I: numerical method. *Int. J. Heat Mass Transfer* 47, 5451–5461.
- Esmaeeli, A., Tryggvason, G., 2004b. Computations of film boiling. Part II: multi-mode film boiling. *Int. J. Heat Mass Transfer* 47, 5463–5476.
- Esmaeeli, A., Tryggvason, G., 2004c. A front tracking method for computations of boiling in complex geometries. *Int. J. Multiphase Flow* 30, 1037–1050.
- Fan, L.S., Tsuehiya, K., 1990. *Wake Dynamics in Liquids and Liquids-Solid Suspensions*. Butterworth-Heinemann, Boston.
- Fedkiw, R.P., Aslam, T., Merriman, B., Osher, S., 1999. A non-oscillatory Eulerian approach to interfaces in multimaterial flows (the Ghost Fluid Method). *J. Comput. Phys.* 152, 457–492.
- Forster, H.K., Zuber, N., 1955. Dynamics of vapor bubbles and boiling heat transfer. *AIChE J.* 1, 531–535.
- Francois, M., Cummins, S., Dendy, E., Kothe, D., Sicilian, J., Williams, M., 2006. A balanced-force algorithm for continuous and sharp interfacial surface tension models within a volume tracking framework. *J. Comput. Phys.* 213, 141–173.
- Fritz, W., 1935. Berechnung des Maximalvolumens von Dampfblasen. *Physikalische Zeitschrift* 36, 379–384.
- Gerardi, C., Buongiorno, J., Hu, L.W., McKrell, T., 2010. Study of bubble growth in water pool boiling through synchronized, infrared thermometry and high-speed video. *Int. J. Heat Mass Transfer* 53, 4185–4192.
- Gerardi, C.D., 2009. Investigation of the Pool Boiling Heat Transfer Enhancement of Nano-Engineered Fluids by means of High-Speed Infrared Thermography. Ph.D. thesis. Department of Nuclear Science and Engineering, Massachusetts Institute of Technology.
- Gerlach, D., Tomar, G., Biswas, G., Durst, F., 2006. Comparison of volume-of-fluid methods for surface tension-dominant two-phase flows. *Int. J. Heat Mass Transfer* 49, 740–754.
- Gibou, F., Chen, L., Nguyen, D., Banerjee, S., 2007. A level set based sharp interface method for the multiphase incompressible Navier-Stokes equations with phase change. *J. Comput. Phys.* 222, 536–555.
- Gibou, F., Fedkiw, R.P., Cheng, L.T., Kang, M., 2002. A second-order-accurate symmetric discretization of the Poisson equation on irregular domains. *J. Comput. Phys.* 176, 205–227.
- Gorenflo, D., Sokol, P., Caplanis, S., 1990. Pool boiling heat transfer from single plain tubes to various hydrocarbons. *Int. J. Refrig.* 13, 286–292.

## Bibliography

---

- Haberman, W.L., Morton, R.K., 1954. An experimental study of bubbles moving in liquids, in: Proc. Am. Soc. Civ. Eng.
- Hadamard, J.S., 1911. Mouvement permanent lent d'une sphère liquide visqueuse dans un liquide visqueux. C. R. Acad. Sci. 152, 1735–1752.
- Han, C.Y., Griffith, P., 1965a. The mechanism of heat transfer in nucleate pool boiling - Part I: Bubble initiation, growth and departure. Int. J. Heat Mass Transfer 8, 887–904.
- Han, C.Y., Griffith, P., 1965b. The mechanism of heat transfer in nucleate pool boiling - Part II: The heat flux-temperature difference relation. Int. J. Heat Mass Transfer 8, 905–914.
- Hardt, S., Wondra, F., 2008. Evaporation model for interfacial flows based on a continuum-field representation of the source terms. J. Comput. Phys. 227, 5871–5895.
- Harmathy, T.A., 1960. Velocity of large drops and bubbles in media of infinite and restricted extent. A.I.Ch.E. J. 6, 281–288.
- Hirt, C.W., Nichols, B.D., 1981. Volume of fluid (VOF) method for the dynamics of free boundaries. J. Comput. Phys. 39, 201–225.
- Hua, J., Lou, J., 2007. Numerical simulation of bubble rising in viscous liquid. J. Comput. Phys. 222, 769–795.
- Hua, J., Stene, J.F., Lin, P., 2008. Numerical simulation of 3D bubbles rising in viscous liquids using a front tracking method. J. Comput. Phys. 227, 3358–3382.
- Ishii, M., Hibiki, T., 2006. Thermo-Fluid Dynamics of Two-Phase Flow. Springer, New York.
- Issa, R.I., 1986. Solution of the implicitly discretised fluid flow equations by operator-splitting. J. Comput. Phys. 62, 40–65.
- Jakob, M., Fritz, W., 1931. Versuche über den Verdampfungsvorgang. Forschung auf dem Gebiet der Ingenieurwissenschaften 2, 435–447.
- Jasak, H., 1996. Error Analysis and Estimation for the Finite Volume Method with Applications to Fluid Flows. Ph.D. thesis. Imperial College, University of London.
- Juric, D., Tryggvason, G., 1998. Computation of boiling flows. Int. J. Multiphase Flow 24, 387–410.
- Kang, M., Fedkiw, R.P., Liu, X.D., 2000. A boundary condition capturing method for multiphase incompressible flow. J. Sci. Comput. 15, 323–360.
- Kenning, D.B.R., Kono, T., Wienecke, M., 2001. Investigation of boiling heat transfer by liquid crystal thermography. Exp. Therm. Fluid Sci. 25, 219–229.
- Kenning, D.B.R., Yan, Y., 1996. Pool boiling heat transfer on a thin plate: features revealed by liquid crystal thermography. Int. J. Heat Mass Transfer 39, 3117–3137.

## Bibliography

---

- Kim, H., Buongiorno, J., 2011. Detection of liquid-vapor-solid triple contact line in two-phase heat transfer phenomena using high-speed infrared thermometry. *Int. J. Multiphase Flow* 37, 166–172.
- Kim, J., 2009. Review of nucleate pool boiling bubble heat transfer mechanisms. *Int. J. Multiphase Flow* 35, 1067–1076.
- Kulkarni, A.A., Joshi, J.B., 2005. Bubble formation and bubble rise velocity in gas–liquid systems: a review. *Ind. Eng. Chem. Res.* 44, 5873–5931.
- Kunkelmann, C., 2011. Numerical Modeling and Investigation of Boiling Phenomena. Ph.D. thesis. Institut für Technische Thermodynamik, Technische Universität Darmstadt.
- Kunkelmann, C., Ibrahem, K., Schweizer, N., Herbert, S., Stephan, P., Gambaryan-Roisman, T., 2012. The effect of three-phase contact line speed on local evaporative heat transfer- experimental and numerical investigations. *Int. J. Heat Mass Transfer* 55, 1896–1904.
- Kunkelmann, C., Stephan, P., 2009. CFD simulation of boiling flows using the volume-of-fluid method within OpenFOAM. *Numer. Heat Transfer A* 56, 631–646.
- Kunkelmann, C., Stephan, P., 2010a. Modification and extension of a standard volume-of-fluid solver for simulating boiling heat transfer, in: Proceedings of ECCOMAS CFD 2010. June 14–17, Lisbon, Portugal.
- Kunkelmann, C., Stephan, P., 2010b. Numerical simulation of the transient heat transfer during nucleate boiling of refrigerant hfe-7100. *Int. J. Refrig.* 33, 1221–1228.
- Lebaigue, O., Duquennoy, C., Vincent, S., 2003. Test-case number 1: rise of a spherical cap bubble in a stagnant liquid (PN). <http://test.interface.free.fr/Case01.pdf>. [Last accessed on September 07, 2012].
- van Leer, B., 1974. Towards the ultimate conservative difference scheme. ii. monotonicity and conservation combined in a second-order scheme. *J. Comput. Phys.* 14, 361–370.
- Liu, X.D., Fedkiw, R.P., Kang, M., 2000. A boundary condition capturing method for Poisson's equation on irregular domains. *J. Comput. Phys.* 160, 151–178.
- Magnini, M., Pulvirenti, B., 2011. Height function interface reconstruction algorithm for the simulation of boiling flows. *Comput. Methods in Multiphase Flow VI* 70, 69–80.
- Magnini, M., Pulvirenti, B., Thome, J.R., 2013a. Numerical investigation of hydrodynamics and heat transfer of elongated bubbles during flow boiling in a microchannel. *Int. J. Heat Mass Transfer* 59, 451–471.
- Magnini, M., Pulvirenti, B., Thome, J.R., 2013b. Numerical investigation of the influence of leading and sequential bubbles on slug flow boiling within a microchannel. *Int. J. Therm. Sci.* 71, 36–52.

## Bibliography

---

- Malenkov, I.G., 1972. The frequency of vapor-bubble separation as a function of bubble size. *Fluid Mechanics – Soviet Research* 1, 36–42.
- Mikic, B.B., Rohsenow, W.M., 1969. A new correlation of pool-boiling data including the effect of heating surface characteristics. *ASME J. Heat Transfer* 91, 245–250.
- Moghaddam, S., Kiger, K., 2009a. Physical mechanisms of heat transfer during single bubble nucleate boiling of FC-72 under saturation conditions-I. Experimental investigation. *Int. J. Heat Mass Transfer* 52, 1284–1294.
- Moghaddam, S., Kiger, K., 2009b. Physical mechanisms of heat transfer during single bubble nucleate boiling of FC-72 under saturation conditions-II: Theoretical analysis. *Int. J. Heat Mass Transfer* 52, 1295–1303.
- Moore, D.W., 1963. The boundary layer on a spherical gas bubble. *J. Fluid Mech.* 16, 161–176.
- Moore, D.W., 1965. The velocity of rise of distorted gas bubbles in a liquid of small viscosity. *J. Fluid Mech.* 23, 749–766.
- Mostinski, I.L., 1963. Calculation of heat transfer and critical heat fluxes in liquids based on the law of corresponding states. *Teploenergetika* 10, 66–71.
- Mukherjee, A., Dhir, V.K., 2004. Study of lateral merger of vapor bubbles during nucleate pool boiling. *ASME J. Heat Transfer* 126, 1023–1039.
- Mukherjee, A., Kandlikar, S.G., 2007. Numerical study of single bubbles with dynamic contact angle during nucleate pool boiling. *Int. J. Heat Mass Transfer* 50, 127–138.
- Myers, J.G., Yerramilli, V.K., Hussey, S.W., Yee, G.F., Kim, J., 2005. Time and space resolved wall temperature and heat flux measurements during nucleate boiling with constant heat flux boundary conditions. *Int. J. Heat Mass Transfer* 48, 2429–2442.
- Nakamura, T., Tanaka, R., Yabe, T., Takizawa, K., 2001. Exactly conservative semi-Lagrangian scheme for multi-dimensional hyperbolic equations with directional splitting technique. *J. Comput. Phys.* 174, 171–207.
- Nelson, R.A., 2001. Do we doubt too little? Examples from the thermal sciences. *Exp. Therm. Fluid Sci.* 25, 255–267.
- Nichita, B.A., Zun, I., Thome, J.R., 2010. A level set method coupled with a volume of fluid method for modeling of gas-liquid interface in bubbly flow. *J. Fluids Eng.* 132, 1–15.
- Noh, W.F., Woodward, P.R., 1976. SLIC (Simple Line Interface Calculation). *Lectures Notes in Physics* 59, 330–360.
- Nukiyama, S., 1934. The maximum and minimum values of the heat Q transmitted from metal to boiling water under atmospheric pressure. *J. Jpn. Soc. Mech. Eng.* 37, 367–374.
- OpenFOAM Foundation, 2013. OpenFOAM® version 2.2.0 user and programmer's guide.

## Bibliography

---

- Parkinson, L., Sedev, R., Fornasiero, D., Ralston, J., 2008. The terminal rise velocity of 10–100  $\mu\text{m}$  diameter bubbles in water. *J. Colloid Interface Sci.* 322, 168–172.
- Peebles, F., Garber, H., 1953. Studies of the motion of gas bubbles in liquids. *Chem. Eng. Prog.* 49, 88–97.
- Plesset, M.S., Zwick, S.A., 1954. The growth of vapor bubbles in superheated liquids. *J. Appl. Phys.* 25, 493–500.
- Popinet, S., 2003. Gerris: a tree-based adaptive solver for the incompressible Euler equations in complex geometries. *J. Comput. Phys.* 190, 572–600.
- Popinet, S., 2009. An accurate adaptive solver for surface-tension-driven interfacial flows. *J. Comput. Phys.* 228, 5838–5866.
- Popinet, S., Zaleski, S., 1999. A front-tracking algorithm for accurate representation of surface tension. *Int. J. Numer. Meth. Fluids* 30, 775–793.
- Prosperetti, A., 1981. Motion of two superposed viscous fluids. *Phys. Fluids* 24, 1217–1223.
- Raeini, A.Q., Blunt, M.J., Bijeljic, B., 2012. Modelling two-phase flow in porous media at the pore scale using the volume-of-fluid method. *J. Comput. Phys.* 231, 5653–5668.
- Renardy, Y., Renardy, M., 2002. PROST: a parabolic reconstruction of surface tension for the volume-of-fluid method. *J. Comput. Phys.* 183, 400–421.
- Rhie, C.M., Chow, W.L., 1983. Numerical study of the turbulent flow past an airfoil with trailing edge separation. *AIAA J.* 21, 1525–1532.
- Roghair, I., Lau, Y.M., Deen, N.G., Slagter, H.M., W., B.M., van Sint Annaland, M., Kuipers, J.A.M., 2011. On the drag force of bubbles in bubble swarms at intermediate and high Reynolds numbers. *Chem. Eng. Sci.* 66, 3204–3211.
- Rohsenow, W.M., 1952. A method of correlating heat transfer data for surface boiling of liquids. *Trans. ASME* 74, 969–975.
- Rohsenow, W.M., Hatnett, J.P., Cho, Y.I., 1998. *Handbook of Heat Transfer*. McGraw-Hill, New York.
- Rybczynski, W., 1911. On the translatory motion of a fluid sphere in a viscous medium. *Bull. Acad. Sci. Cracow Ser. A*, 40–46.
- Sanada, T., Sugihara, K., Shirota, M., Watanabe, M., 2008. Motion and drag of a single bubble in super-purified water. *Fluid Dyn. Res.* 40, 534–545.
- Sato, Y., Ničeno, B., 2012. A conservative local interface sharpening scheme for the constrained interpolation profile method. *Int. J. Numer. Meth. Fluids* 70, 441–467.
- Sato, Y., Ničeno, B., 2013. A sharp-interface phase change model for a mass-conservative interface tracking method. *J. Comput. Phys.* 249, 127–161.
- Scardovelli, R., Zaleski, S., 1999. Direct numerical simulation of free-surface and interfacial flow. *Annu. Rev. Fluid Mech.* 31, 567–603.

## Bibliography

---

- Schrage, R.W., 1953. A Theoretical Study of Interphase Mass Transfer. Columbia University Press, New York.
- Schweizer, N., Stephan, P., 2009. Experimental study of bubble behavior and local heat flux in pool boiling under variable gravitational conditions. *Multiphase Sci. Tech.* 21, 329–350.
- Scriven, L.E., 1959. On the dynamics of phase growth. *Chem. Eng. Sci.* 10, 1–13.
- van Sint Annaland, M., Dijkhuizen, W., Deen, N.G., Kuipers, J.A.M., 2006. Numerical simulation of behavior of gas bubbles using a 3D front-tracking method. *A.I.Ch.E. J.* 52, 99–110.
- Son, G., 2001. A numerical method for bubble motion with phase change. *Numer. Heat Transfer B* 39, 509–523.
- Son, G., 2005. A level set method for incompressible two-fluid flows with immersed solid boundaries. *Numer. Heat Transfer B* 47, 473–489.
- Son, G., Dhir, V.K., 1998. Numerical simulation of film boiling near critical pressures with a level set method. *ASME J. Heat Transfer* 120, 183–192.
- Son, G., Dhir, V.K., 2007. A level set method for analysis of film boiling on an immersed solid surface. *Numer. Heat Transfer B* 52, 153–177.
- Son, G., Dhir, V.K., 2008a. Numerical simulation of nucleate boiling on a horizontal surface at high heat fluxes. *Int. J. Heat Mass Transfer* 51, 2566–2582.
- Son, G., Dhir, V.K., 2008b. Three-dimensional simulation of saturated film boiling on a horizontal cylinder. *Int. J. Heat Mass Transfer* 51, 1156–1167.
- Son, G., Dhir, V.K., Ramanujapu, N., 1999. Dynamic and heat transfer associated with a single bubble during nucleate boiling on a horizontal surface. *ASME J. Heat Transfer* 121, 623–631.
- Son, G., Ramanujapu, N., Dhir, V.K., 2002. Numerical simulation of bubble merger process on a single nucleation site during pool nucleate boiling. *ASME J. Heat Transfer* 124, 51–62.
- Stephan, K., 1992. Heat Transfer in Condensation and Boiling. Springer-Verlag, Berlin.
- Stephan, K., Abdelsalam, M., 1980. Heat-transfer correlations for natural convection boiling. *Int. J. Heat Mass Transfer* 23, 73–87.
- Stephan, P., Kern, J., 2004. Evaluation of heat and mass transfer phenomena in nucleate boiling. *Int. J. Multiphase Flow* 25, 140–148.
- Sussman, M., Puckett, E.G., 2000. A coupled level set and volume-of-fluid method for computing growth and collapse of vapor bubbles. *J. Comput. Phys.* 162, 301–337.
- Sussman, M., Smereka, P., Osher, S., 1994. A level set approach for computing solutions to incompressible two-phase flow. *J. Comput. Phys.* 114, 146–159.
- Sweby, P.K., 1984. High resolution schemes using flux limiters for hyperbolic conservation laws. *SIAM J. Numer. Anal.* 21, 995–1011.

---

## Bibliography

- Tanguy, S., Ménard, T., Berlemont, A., 2007. A level set method for vaporizing two-phase flows. *J. Comput. Phys.* 221, 837–853.
- The MathWorks, 2011. MATLAB® Release 2011a. The MathWorks, Inc., Natick, MA, USA.
- Theofanous, T.G., Dinh, T.N., Tu, J.P., Dinh, A.T., 2002a. The boiling crisis phenomenon: Part II: dryout dynamics and burnout. *Exp. Therm. Fluid Sci.* 26, 793–810.
- Theofanous, T.G., Tu, J.P., Dinh, A.T., Dinh, T.N., 2002b. The boiling crisis phenomenon: Part I: nucleation and nucleate boiling heat transfer. *Exp. Therm. Fluid Sci.* 26, 775–792.
- Tomar, G., Biswas, G., 2005. Numerical simulation of bubble growth in film boiling using a coupled level-set and volume-of-fluid method. *Phys. Fluids* 17, 1–13.
- Tomiyama, A., 2004. Drag, lift and virtual mass forces acting on a single bubble, in: Proceedings of the Third International Symposium on Two-Phase Flow Modelling and Experimentation. September 22–24, Pisa, Italy.
- Tomiyama, A., Celata, G.P., Hosokawa, S., Yoshida, S., 2002. Terminal velocity of single bubbles in surface tension force dominant regime. *Int. J. Multiphase Flow* 28, 1497–1519.
- Torrey, M., Cloutman, L., Mjolsness, R., Hirt, C., 1985. NASA-VOF2D: a computer program for incompressible flows with free surfaces. Technical Report. Los Alamos National Laboratory.
- Tryggvason, G., Bunner, B., Esmaeeli, A., Juric, D., Al-Rawahi, N., Tauber, W., Han, J., Nas, S., Jan, Y.J., 2001. A front-tracking method for the computations of multi-phase flow. *J. Comput. Phys.* 169, 708–759.
- Tubović, Ž., Jasak, H., 2012. A moving mesh finite volume interface tracking method for surface tension dominated interfacial fluid flow. *Comput. Fluids* 55, 70–84.
- Ubbink, O., Issa, R.I., 1999. Method for capturing sharp fluid interfaces on arbitrary meshes. *J. Comput. Phys.* 153, 26–50.
- Unverdi, S.O., Tryggvason, G., 1992. A front tracking method for viscous, incompressible, multi-fluid flows. *J. Comput. Phys.* 100, 25–37.
- Vachon, R.I., E., T.G., Davis, D.L., Nix, G.H., 1967a. Pool boiling on polished and chemically etched stainless steel surfaces, in: Paper 67-HT-34 presented at US National Heat Transfer Conference, Seattle.
- Vachon, R.I., Nix, G.H., E., T.G., 1967b. Evaluation of cconstant for the rohsenow pool boiling correlation, in: Paper 67-HT-33 presented at US National Heat Transfer Conference, Seattle.
- Welch, S.W.J., 1995. Local simulation of two-phase flows including interface tracking with mass transfer. *J. Comput. Phys.* 121, 142–154.

## Bibliography

---

- Welch, S.W.J., 1998. Direct simulation of vapor bubble growth. *Int. J. Heat Mass Transfer* 41, 1655–1666.
- Welch, S.W.J., Rachidi, T., 2002. Numerical computation of film boiling including conjugate heat transfer. *Numer. Heat Transfer B* 42, 35–53.
- Welch, S.W.J., Wilson, J., 2000. A volume of fluid based method for fluid flows with phase change. *J. Comput. Phys.* 160, 662–682.
- Whitaker, S., 1999. *The Method of Volume Averaging*. Springer.
- Wu, J., Dhir, V.K., 2011. Numerical simulation of dynamics and heat transfer associated with a single bubble in subcooled boiling and in the presence of noncondensables. *ASME J. Heat Transfer* 133, 1–14.
- Wu, M., Gharib, M., 1998. Path instabilities of air bubbles rising in clean water, in: eprint arXiv:patt-sol/9804002.
- Yang, B., Prosperetti, A., Takagi, S., 2003. The transient rise of a bubble subject to shape or volume changes. *Phys. Fluids* 15, 2640–2648.
- Youngs, D.L., 1982. *Time-Dependent Multi-Material Flow With Large Fluid Distortion*. Academic Press, New York.
- Yu, B., Tao, W.Q., Wei, J.J., Kawaguchi, Y., Tagawa, T., Ozoe, H., 2002. Discussion on momentum interpolation method for collocated grids of incompressible flow. *Numer. Heat Transfer B* 42, 141–166.
- Yuan, M.H., Yang, Y.H., Li, T.S., Hu, Z.H., 2008. Numerical simulation of film boiling on a sphere with a volume of fluid interface tracking method. *Int. J. Heat Mass Transfer* 51, 1646–1657.
- Zuber, N., 1963. Nucleate boiling. The region of isolated bubbles and the similarity with natural convection. *Int. J. Heat Mass Transfer* 6, 53–78.
- Zun, I., Groselj, J., 1996. The structure of bubble non-equilibrium movement in free-rise and agitated-rise conditions. *Nucl. Eng. Des.* 163, 99–115.